

UCLA

UCLA Electronic Theses and Dissertations

Title

Development of a Regional Wind Risk Assessment Framework for Wood-frame Single-family Residential Building Stock

Permalink

<https://escholarship.org/uc/item/8pn8h3bq>

Author

Meng, Shuochuan

Publication Date

2023

Peer reviewed|Thesis/dissertation

UNIVERSITY OF CALIFORNIA

Los Angeles

DEVELOPMENT OF A REGIONAL WIND RISK ASSESSMENT FRAMEWORK FOR
WOOD-FRAME SINGLE-FAMILY RESIDENTIAL BUILDING STOCK

A dissertation submitted in partial satisfaction
of the requirements for the degree
Doctor of Philosophy in Civil Engineering

by

Shuochuan Meng

2023

© Copyright by
Shuochuan Meng
2023

ABSTRACT OF THE DISSERTATION

DEVELOPMENT OF A REGIONAL WIND RISK ASSESSMENT FRAMEWORK FOR WOOD-FRAME SINGLE-FAMILY RESIDENTIAL BUILDING STOCK

by

Shuochuan Meng

Doctor of Philosophy in Civil Engineering

University of California, Los Angeles, 2023

Professor Ertugrul Taciroglu, Chair

Over the past few decades, residential buildings along the coastal areas of the United States have suffered enormous structural damage and economic losses due to hurricane strikes. The significant variations in the building characteristics of residential buildings lead to distinctive building-level vulnerabilities under extreme winds. Therefore, an accurate representation of the building inventory is critical for quantifying regional hurricane risk.

In this dissertation, a regional wind risk assessment framework is developed to evaluate hurricane-induced structural damage and economic losses for residential communities. Unlike existing loss models that represent the building stock by archetype models with limited variations in building characteristics, the proposed framework applies site-specific risk assessments on every house in the region of interest based on parcel-based building inventories. A sensitivity analysis is conducted to investigate the effects of different building features on building vulnerability to identify the most critical features and explore the means of simplifying the building modeling process. To apply site-specific damage assessments at regional level, an automatic building modeling workflow is integrated into the framework, which is

supported by property-specific characteristics extracted through machine learning-aided data collection approaches.

The framework is applied to residential communities in New Hanover County, North Carolina. Through site-specific risk assessments on 1,746 realistic building models, the overall variance in building-level damage and loss results among single-family houses is evaluated. The damage results reveal significant differences in wind vulnerability due to variations in architectural features. Furthermore, a comparative study shows that the aggregated regional loss calculated based on refined building models is substantially higher than that derived from building archetypes used in existing regional loss models. The building inventory generation and building modeling modules integrated into the framework largely reduce the inherent uncertainties of hurricane risk prediction. The high-resolution damage and loss results produced by the framework offer insights into local risk conditions, which facilitate the improvement of hazard risk mitigation and post-disaster management strategies.

The dissertation of Shuochuan Meng is approved.

Henry J. Burton

Jingyi Li

Rachel A. Davidson

Scott Joseph Brandenburg

Ertugrul Taciroglu, Committee Chair

University of California, Los Angeles

2023

*To my wife Zhiyin,
for her endless love, support, and encouragement*

TABLE OF CONTENTS

1	INTRODUCTION	1
1.1	Introduction	1
1.2	Objective and Scope	2
1.2.1	Construction of parcel-based building inventories	3
1.2.2	Archetype-based modeling methodology for individual buildings	3
1.2.3	Automation of site-specific wind risk assessment	4
1.3	Case Study Area	4
1.4	Contributions	6
1.5	Organization	7
2	LITERATURE REVIEW	8
2.1	Major Building Characteristics for Single-family Houses	8
2.2	Wind Vulnerability Modeling of Single-family Houses	12
2.3	Building Data Collection Techniques	15
3	SENSITIVITY ANALYSIS FOR EXTREME WIND FRAGILITY OF ROOF SHEATHING	17
3.1	Introduction	17
3.2	Building Models	18
3.3	Fragility Modeling Methodology	24
3.3.1	Damage states	24
3.3.2	Fragility analysis	25

3.3.3	Uplift capacity	26
3.3.4	Dead load and wind load	27
3.4	Fragility Curves	30
3.4.1	Effect of roof shape	30
3.4.2	Effect of roof pitch	36
3.4.3	Comparison with other characteristics	39
3.5	Roof Modeling Methodology	41
3.6	Limitations	44
3.7	Summary	45
4	BUILDING INVENTORY GENERATION MODEL	47
4.1	Overview	47
4.2	Baseline Building Inventory	50
4.3	Building Data Collection Methods	56
4.3.1	Roof plan dimension measurement	56
4.3.2	Roof type classification	66
4.3.3	Number of stories classification	79
4.3.4	Roof pitch prediction	88
4.4	Case Study	96
4.4.1	Roof type classification	96
4.4.2	Building inventory generation	105
4.5	Summary	113
5	DAMAGE AND LOSS ASSESSMENT MODEL	114

5.1	Model Description	115
5.1.1	Overview	115
5.1.2	Probabilistic hurricane scenario	116
5.1.3	Building inventory	117
5.1.4	Building modeling	120
5.1.5	Damage analysis	126
5.1.6	Loss analysis	131
5.2	Building Modeling Results	133
5.3	Damage Results	134
5.3.1	Component-level damage results	135
5.3.2	Building-level damage results	139
5.4	Loss Results	141
5.5	Model Limitations	146
5.6	Summary	148
6	CONCLUSIONS AND FUTURE WORK	150
6.1	Conclusions	150
6.2	Future Work	151
A	EXTERNAL WIND PRESSURE COEFFICIENTS	153
B	FRAGILITY PARAMETERS FOR ROOF SHEATHING	155
C	BASIC PARAMETERS FOR DAMAGE ANALYSIS	161
D	INTERIOR DAMAGE CALCULATION	163

LIST OF FIGURES

1.1	General steps of the regional wind risk assessment framework	2
1.2	Locations and satellite images of study areas	5
2.1	Critical building characteristics for wind vulnerability modeling of single-family houses	9
2.2	Typical garage types for single-family houses in the United States	12
2.3	Building components considered for wind damage calculation for wood-frame single-family houses	13
3.1	Dimensions and panel layouts for gable-roof building models (all dimensions are given in meters)	20
3.2	Dimensions and panel layouts for hip-roof building models (all dimensions are given in meters)	21
3.3	Dimensions and roof sheathing layout, Structure Type 6 (all dimensions are given in meters)	22
3.4	Characteristics of building models (Set 2) (a) Roof configurations and dimensions for baseline building models. The panel layouts are shown for 4:12 pitched roofs. (b) Selected roof pitch (all dimensions are given in meters)	23
3.5	Simulation procedure for roof sheathing fragility assessment	26
3.6	Wind pressure zones for GC_p for C&C on roofs: (a) Gable roofs; (b) Hip roofs	29
3.7	Fragility curves for gable-roofed buildings (Type 1-23)	31
3.8	Median wind speed of fragility curves for gable-roofed buildings (Type 1-23)	32
3.9	Fragility curves for hip-roofed buildings (Type 24-47)	33
3.10	Median wind speed of fragility curves for hip-roofed buildings (Type 24-47)	34

3.11	Fragility curves for all buildings in building model set 1: (a) DS1; (b) DS4 . . .	35
3.12	Fragility curves for gable-roof buildings with different roof pitches: (a) Structure type A; (b) Structure type B	37
3.13	Median wind speed of fragility curves for gable-roof buildings: (a) Structure type A; (b) Structure type B	37
3.14	Fragility curves for hip-roof buildings with different roof pitches (DS1): (a) Structure type C; (b) Structure type D	38
3.15	Median wind speed of fragility curves for hip-roof buildings: (a) Structure type C; (b) Structure type D	39
3.16	Fragility curves for Type 7 with different building features: (a) DS1; (b) DS4 . .	40
3.17	Fragility curves for Type 29 with different building features: (a) DS1; (b) DS4 .	41
3.18	Archetype roof plans for different roof types	43
4.1	Structure of the building inventory generation model	49
4.2	Measurement of roof dimensions using a building-level satellite image	52
4.3	Validation of the roof dimension measurement process	53
4.4	Distribution of roof area for houses in the baseline inventory	53
4.5	Distribution of roof types for houses in the baseline inventory	54
4.6	Measurement of roof pitch: (a) Direct measurement for buildings with gable end wall visible in street view images; (b) Indirect measurement based on roof height and plan dimensions	55
4.7	Distribution of roof pitch for houses in the baseline inventory	56
4.8	Workflow for roof plan dimension measurement process	58
4.9	Illustration of the U-Net architecture	59
4.10	Roof mask area for the testing dataset	60

4.11	Representative roof segmentation and outline extraction results on the testing dataset	61
4.12	Comparison of building footprints: (a) The model developed in this study; (b) Microsoft OpenStreetMap; (c) FEMA USA Structures	62
4.13	Incorrect roof outlines due to tree occlusion: (a) Slightly blocked rectangular roof with incorrect roof outline and correct bounding box; (b) Slightly blocked non-rectangular roof with incorrect roof outline and correct bounding box; (c) Heavily blocked roof with incorrect roof outline and bounding box	63
4.14	Flowchart of the roof dimension refinement process	65
4.15	Example building models with different types of roofs	67
4.16	Example low-quality satellite images: (a) Rooftop is heavily blocked by trees; (b) Geolocation of the building is incorrect; (c) The building was demolished	67
4.17	Flowchart for roof type classification	68
4.18	Examples satellite images in the training dataset for roof type classification	70
4.19	VGG-19 architecture adopted from Simonyan and Zisserman (2014)	72
4.20	Confusion matrix of VGG-19 for roof type classification evaluated on validation dataset	72
4.21	Confusion matrix of VGG-19 evaluated on test datasets A (buildings with pure gable, pure hip, and unknown-type roofs)	74
4.22	Example satellite images in testing dataset B (buildings with complex and mixed roof shapes)	76
4.23	Confusion matrix of VGG-19 evaluated on testing dataset B (buildings with mixed roof shapes)	76
4.24	Process of mapping roof features predicted by imputation algorithms to roof types	78
4.25	Neighborhoods with similar roof styles	79

4.26	General steps of missing roof-type data imputation	79
4.27	Typical elevated single-family houses with different enclosure condition of the base floor: (a) Enclosed; (b) Partially enclosed; (c) Partially open	81
4.28	Single-story houses with attics considered to be two-story in ZTRAX	81
4.29	Number of stories for single-family houses	82
4.30	Flowchart for the number of stories classification process	83
4.31	Example low-quality street view images: (a) The building is heavily blocked by trees; (b) The building is blurred; (c) The image is unavailable	84
4.32	Top 3 prediction results on example street view images using Places365-ResNet: (a) The building can be clearly viewed; (b) The building is heavily obscured; (c) The building is not visible	84
4.33	Example street view images in the training dataset for number of stories classifi- cation	85
4.34	Confusion matrix of the number of stories classification model evaluated on the validation dataset	86
4.35	Example street view images in the testing dataset for single-family houses in New Hanover County	87
4.36	Confusion matrix of the number of stories classification model evaluated on the testing dataset	88
4.37	Representative single-family houses with attics and steep roofs. Roof pitch: (a) 8/12 (34°); (b) 10/12 (40°); (c) 16/12 (53°)	90
4.38	Distribution of roof pitch with different attic conditions for the baseline inventory	91
4.39	Correlation between building characteristics: (a) Dendrogram of the hierarchical clustering on the Spearman rank-order correlations; (b) Heatmap of the Spearman rank-order correlations	92

4.40	Comparison of the model performance on predicting roof pitch with different thresholds	93
4.41	Permutation feature importance evaluated on validation dataset for roof pitch prediction using Random Forest	94
4.42	Prediction of roof pitch on testing dataset with Random Forest Regression: (a) Roof pitch in degree; (b) Standardized roof pitch	96
4.43	Case study area in Miami-Dade County and associated census tract boundaries	97
4.44	Predicted roof type map for study areas	98
4.45	Roof type distribution for study areas	99
4.46	Fraction of single-family houses with gable roofs per census tract in study areas. (census tracts with less than ten houses were removed from the map)	100
4.47	Fraction of single-family houses with complex roofs, including simple cross-gable, complex cross-gable and cross-hip roofs, per census tract in study areas (census tracts with less than ten houses were removed from the map)	100
4.48	Candidate search radius used to calculate neighborhood-level roof type distribution for predicting missing roof-type data	101
4.49	Permutation feature importance evaluated on validation dataset for Miami-Dade County with Random Forest : (a) Predicting roof to be gable or hip; (b) Predicting roof to be simple or complex	103
4.50	Location and ground truth roof type of buildings in the testing dataset	104
4.51	Bird eye’s view images of study areas (images are from Google Earth)	106
4.52	Distribution of year built for study areas	107
4.53	Distribution of building value for study areas	107
4.54	Distribution of roof area for study areas	108

4.55	Comparison between original images from Google Maps and refined images produced by the roof segmentation model	109
4.56	Distribution of roof type for study areas	110
4.57	Distribution of number of stories for study areas	111
4.58	Distribution of roof pitch for study areas	112
5.1	General steps for the site-specific wind loss model	115
5.2	Annual exceedance probability of wind speed and associated hurricane categories for hurricane scenarios	117
5.3	Key components of the building inventory	118
5.4	General steps for the building modeling process	122
5.5	Roof modeling process	123
5.6	Roof plan and panel layout for cross-hip roofs with different plan dimensions . .	124
5.7	Opening layouts for buildings with different roof types: (a) Simple gable and hip; (b) Simple cross-gable; (c) Complex cross-gable; (d) Cross-hip	125
5.8	Opening layouts for elevated houses	125
5.9	Wind pressure zones for GC_p for C&C on walls	129
5.10	Flowchart of wind damage analysis	131
5.11	Comparison between building models and actual structures (building images are from Google Earth)	134
5.12	Damage vulnerability for roof components: (a) Roof sheathing; (b) Roof covering	136
5.13	Fragility curves for roof sheathing damage: (a) DS1 (no roof sheathing failure); (b) DS3 (25% of roof sheathing failure)	137
5.14	Fragility curves for roof covering damage: (a) DS1 (15% of roof covering failure); (b) DS2 (50% of roof covering failure)	137

5.15 Window damage vulnerability	138
5.16 Building-level fragility curves: (a) DS1; (b) DS2; (c) DS3; (d) DS4	140
5.17 Distribution of expected annual loss at building level	141
5.18 Annual probabilities of loss exceedance for individual buildings: (a) Study area 1; (b) Study area 2	142
5.19 Building models and opening layouts for archetype-based loss assessment	144
5.20 Building-level expected annual losses calculated using different types of assess- ments: (a) Study area 1; (b) Study area 2	145
5.21 Comparison of regional losses between assessments using building archetypes and site-specific building models	146

LIST OF TABLES

3.1	Dimensions and characteristics of building models (Set 1)	22
3.2	Dimensions and characteristics of building models (Set 2)	24
3.3	Resistance (R), dead load (D), and wind load (W) statistics	27
3.4	Proposed roof types for single-family houses	42
4.1	Categorical building attributes in the baseline building inventory	50
4.2	Numerical building attributes in the baseline building inventory	51
4.3	Mean roof geometry parameters calculated for the baseline building inventory	65
4.4	Distribution of training and validation images for the roof classification model	69
4.5	Performance of VGG-19 on testing dataset A (buildings with pure gable, pure hip, and unknown-type roofs)	74
4.6	Performance of VGG-19 on testing dataset B (buildings with mixed roof shapes)	77
4.7	Distribution of number of stories for single family houses in New Hanover County (Zillow, 2018)	80
4.8	Performance of the number of stories classification model on the testing dataset	88
4.9	Performance of machine learning models on roof pitch prediction	95
4.10	Prediction accuracy of roof type (gable or hip) using dominant roof type surrounding each building, and the proportion of buildings missing neighbors within the search radius	102
4.11	Features used for roof type and roof complexity prediction with data imputation algorithms	103
4.12	Validation and testing accuracy of predicting roof type (gable or hip) with different models	105

4.13	Validation and testing accuracy of predicting roof complexity (simple or complex) with different models	105
5.1	Building components for wind damage modeling of wood-frame residential buildings	119
5.3	Estimated distribution of component configurations by year built (modified from Peng (2013))	120
5.2	Resistance statistics of Components and Claddings (modified from Peng (2013))	121
5.4	Dimension of openings for building modeling	124
5.5	Damage states for wood-frame residential buildings	127
5.6	Component replacement ratio	132
5.7	Comparison between building archetypes and site-specific building models . . .	143
A.1	Nominal value of negative GC_p for C&C on gable roofs	153
A.2	Nominal value of negative GC_p for C&C on hip roofs	154
B.1	Lognormal parameters for roof sheathing fragilities (building model set 1)	155
B.2	Lognormal parameters for roof sheathing fragilities (Structure Type A)	157
B.3	Lognormal parameters for roof sheathing fragilities (Structure Type B)	157
B.4	Lognormal parameters for roof sheathing fragilities (Structure Type C)	158
B.5	Lognormal parameters for roof sheathing fragilities (Structure Type D)	158
B.6	ANOVA test on the median of fragility curves between gable-roof building model groups	159
B.7	ANOVA test on the median of fragility curves of complex hip-roof building model groups (Groups 7-11)	160
C.1	Wind speed	161

C.2 Component damage ratio	162
D.1 Interior damage equations	164

ACKNOWLEDGMENTS

This dissertation incorporates interdisciplinary knowledge from various fields, many of which were unfamiliar to me before embarking on my Ph.D. research. Therefore, I am deeply thankful for all the assistance I received throughout my Ph.D. studies, which aided me in surmounting numerous challenges until the completion of this dissertation.

First and foremost, I would like to extend my heartfelt appreciation to my advisor, Prof. Ertugrul Taciroglu, for his invaluable guidance, unwavering support, and continuous encouragement throughout my academic journey. His insights into urban resilience shaped this dissertation, while sufficient freedom and trust were provided to me to put my own ideas into practice. Furthermore, the extensive collaboration opportunities he created allowed me to connect to experts from different fields and acquire their valuable feedback on my research. This greatly enriched the quality of my work and broadened my perspective. His generous personal and professional guidance has been invaluable in supporting me to pursue my academic and career goals.

Second, I would like to express my sincere appreciation to my Ph.D. committee members, Prof. Henry Burton, Prof. Jingyi Li, Prof. Rachel Davidson, and Prof. Scott Brandenburg, for their insightful comments and constructive criticism on my research. I would also like to convey my special thanks to Prof. Rachel Davidson. Her expert advice and feedback have been instrumental in directing the course of my research. The previous studies conducted by her and her students served as the foundation for the regional loss model developed in this dissertation. Her dedication and passion for research have made her a great role model for me to follow.

Third, I am grateful for the financial support from the National Science Foundation under award 2209190 and the building metadata provided by Zillow through the Zillow Transaction and Assessment Dataset (ZTRAX). The results and opinions presented in this dissertation do not reflect the position of NSF or the Zillow Group.

I also want to express my appreciation to my colleagues and collaborators, Dr. Pengyu Chen, Dr. Hesam Soleimani, and Caroline Williams. Their consistent feedback and encouragement throughout different phases of my Ph.D. studies have been a continual source of motivation and inspiration. I am truly grateful for their friendship, mentorship, and the impact they have had on my personal and professional growth.

In closing, I would like to express my deepest gratitude to my family members. My parents, Xiancheng Meng and Xiaohong Xu, provided me with the opportunity to study abroad and their unconditional love and support. Above all, I want to thank my wife, Zhiyin Lin, for being my constant companion throughout my Ph.D. journey. She supported me through the most challenging times during the pandemic and took care of me while busy with her studies and work. She has also made significant contributions to the development of the building modeling workflow. Without her invaluable assistance, this dissertation would not have been possible.

VITA

- 2017 B.E. (Civil Engineering), Tianjin University, Tianjin, China.
- 2019 M.S. (Civil Engineering), UCLA, Los Angeles, CA.
- 2019–2023 Teaching Fellow, Department of Civil and Environmental Engineering,
UCLA, Los Angeles, CA.
- 2019 Structural Engineering Intern, JCE Structural Engineering Group, Los Angeles, CA.
- 2022 Risk and Resilience Engineering Intern, Arup, San Francisco, CA.

CHAPTER 1

INTRODUCTION

1.1 Introduction

Wood-frame residential buildings, the most prevalent building type in the United States, are particularly fragile under extreme winds, such as hurricanes and tornadoes (van de Lindt and Dao, 2009). According to insurance claim files from past hurricanes (Sparks et al., 1994), the majority of wind losses are caused by breaches in the building envelope and resulting rain penetration. Various building characteristics, such as roof type, roof pitch, and building shape, have significant impacts on the wind pressures acting on the building envelope (Meecham et al., 1991; Wiik and Hansen, 1997; Xu and Reardon, 1998; Shao et al., 2018; Sarma et al., 2023). An alteration in any of these attributes can result in distinctive wind performance of the structure (Li, 2005; Brown-Giammanco et al., 2018; Masoomi et al., 2018).

Based on functional and aesthetic needs, the appearance of single-family residential buildings in the United States varies substantially. However, the variations of very few building features are considered in the archetype building models adopted by existing regional wind loss frameworks, including the Federal Emergency Management Agency (FEMA) HAZUS-MH model (Vickery, 2006) and the Florida Public Hurricane Loss Model (FPHLM) (Pinelli et al., 2011; Hamid, 2021). The simplified and idealized building models can potentially compromise the validity of wind damage and loss estimation. The adoption of more detailed building models is mainly hindered by two obstacles. First, the determination of wind loads

for buildings with complex geometries is challenging due to limited experimental results. Second, the building attributes of interest are usually missing in available datasets, which obstructs the mapping from building prototypes to the building stock.

This dissertation presents an end-to-end framework for quantifying the wind risk of large-scale single-family residential building stock. The proposed framework aims to improve the regional wind loss projection by incorporating detailed and realistic building models into wind damage simulations. The framework starts with the generation of a parcel-based building inventory, followed by building-level risk assessments that incorporate a variety of site-specific building properties. The enriched building data and associated building modeling methodology considerably reduce the uncertainties in the building inventory and enhance the accuracy of damage and loss estimation.

1.2 Objective and Scope

The research objective of this dissertation is to develop a regional wind risk assessment framework (Fig. 1.1) by integrating machine learning-based building inventory generation and automatic building modeling. The framework aims to improve the understanding of wind risk for single-family residential building stock by adopting detailed building models built upon enriched building inventories. The main tasks that support this objective are introduced in the following sections.

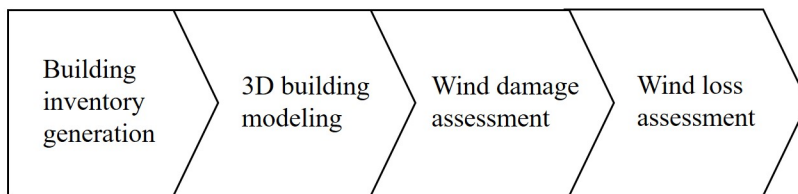


Figure 1.1: General steps of the regional wind risk assessment framework

1.2.1 Construction of parcel-based building inventories

The building inventory is an essential input for the wind risk assessment, and parcel-based building inventory allows for damage and loss estimation at the individual building level. However, many building characteristics important in determining wind vulnerability, such as roof type and roof pitch, are often missing or of low-quality in existing building databases. Recent advancements in computer vision have provided powerful tools to extract building attribute data from remote sensing data. Large-scale building inventories can be produced by combining advanced image processing methods with publicly available remote sensing database such as Google Maps. In addition, statistical models can be adopted to infer missing building features based on the correlations among different building characteristics. Consequently, an integrated model that incorporates various data collection techniques is necessary for the construction of high-resolution building inventories for use in wind risk assessment.

1.2.2 Archetype-based modeling methodology for individual buildings

The implementation of site-specific risk assessments requires the construction of 3D building models that provide the layout and location of building components. Due to the complex nature of single-family residential construction, simplifications are necessary when converting real structures to building models. Integrating building archetypes into individual building modeling can effectively reduce the computational complexity of the modeling process. The development of efficient modeling methodologies must also take into account the availability of building attribute data and the capability of the wind vulnerability model. To accurately reflect the wind performance of the original structure, the building model should be capable of capturing critical building characteristics, which requires an understanding of the relative importance of building features to building vulnerability. On the other hand, the building modeling methodology guides the development and optimization of the building data

collection process.

1.2.3 Automation of site-specific wind risk assessment

To conduct site-specific risk assessment at the regional scale, it is necessary to automate the assessment process. The framework must be able to automatically create building models, generate building components, and determine wind pressures on each component unit. This enables the forecast of wind damage for individual buildings and the estimation of aggregated regional losses. The proposed assessment methodology incorporates the correlations among building attributes and the spatial variance of the building inventory, which facilitates the improvement of post-disaster recovery strategies. The building-level results also reveal the variance of wind vulnerability for single-family houses, providing insight into the relative importance of each building variable.

1.3 Case Study Area

New Hanover County, located on the southeastern coast of North Carolina, is selected as the study area for this dissertation. It is comprised of various municipalities, including the city of Wilmington and coastal towns of Wrightsville Beach, Kure Beach, and Carolina Beach. As part of the hurricane-prone Eastern Seaboard, New Hanover County is particularly vulnerable to direct tropical cyclone strikes. Recent major hurricanes that affected New Hanover County include Irene (2011), Matthew (2016), and Florence (2018). Hurricane Florence, which made landfall in Wrightsville Beach as a Category 1 hurricane, resulted in 24 billion dollars in damages. Over the past decade, extensive efforts have been made to quantify the regional hazards, predict the wind losses, and improve the post-disaster management strategies in this area (Apivatanagul et al., 2011; Peng, 2013; Peng et al., 2014; Wang et al., 2020). Nonetheless, due to the lack of field studies, a comprehensive building inventory dataset for New Hanover County is not yet available. Therefore, substantial assumptions and approx-

imations were made when describing the building stock at risk, introducing considerable uncertainty to the regional loss estimation. In this dissertation, the distribution of critical building characteristics for the single-family residential building stock in New Hanover County is investigated. Furthermore, the regional wind risk assessment framework is implemented to 1,746 single-family houses in two residential communities (Fig. 1.2) in New Hanover County, denoted as study areas 1 and 2. The selected study areas are considered to be representative of residential neighborhoods in coastal and non-coastal regions of the United States. The differences in building density and vegetation coverage between these areas aid in evaluating the generalizability of the building inventory generation methodology proposed in this dissertation.

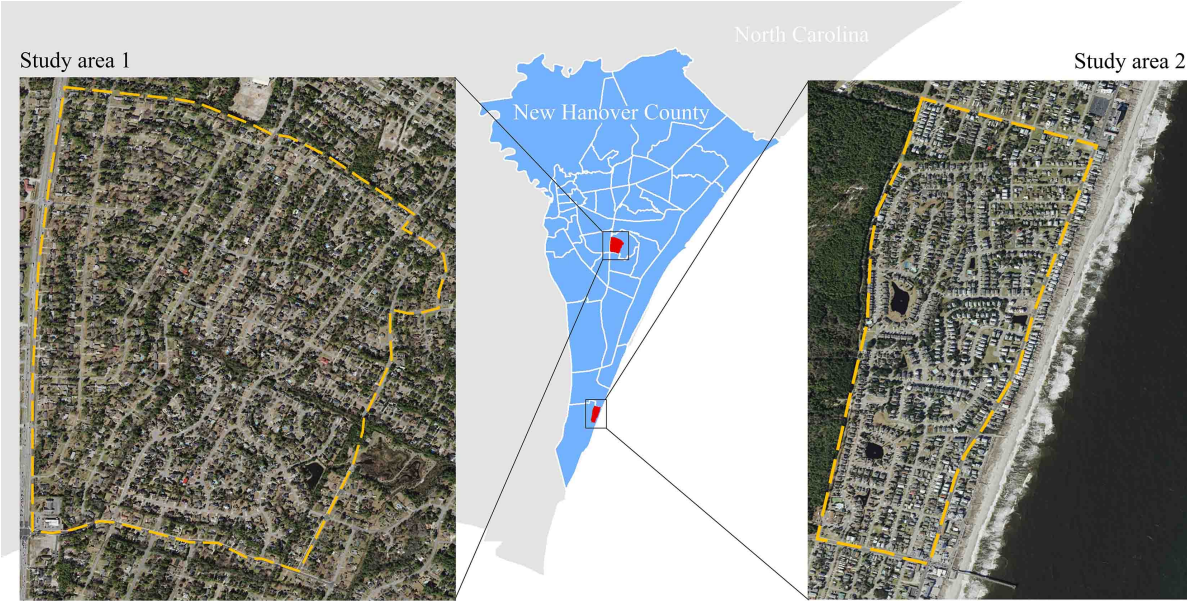


Figure 1.2: Locations and satellite images of study areas

1.4 Contributions

The main contributions of this study are summarized below:

1. The sensitivity analysis described in Chapter 3 provides a quantitative evaluation of the relative importance of building characteristics in wind vulnerability modeling of roof sheathing. Specifically, it assesses the effects of building shape and roof pitch, the variations of which have not been incorporated into the building archetypes used by existing wind vulnerability models.
2. An archetype-based modeling methodology for complex-shaped roofs is developed. The proposed method largely simplifies the modeling of complex roofs and reduces the amount of required input data. This methodology allows for the inclusion of complex roof geometries in wind damage analysis, which improves the accuracy of wind damage and loss estimation.
3. Data collection methods are developed to produce reliable and low-cost building inventories through machine learning, which can be extended to other hazards. The advanced techniques enable the generation of large-scale and high-resolution building inventories. Strategies are created to filter out low-quality remote sensing data and impute any missing data, which improve the reliability and completeness of the building inventory. The generalizability of the proposed methods is also examined through the case study.
4. Large-scale building datasets, including building features that are not available in publicly available databases, are created using manual investigation and machine learning. The building datasets reveal the distribution of critical building characteristics and guide the development of more detailed and realistic building archetypes.
5. Site-specific risk assessments are conducted on a large-scale building inventory, which reveal the overall variance in wind vulnerability of single-family houses, taking into

account a variety of building characteristics. The building-level wind damage results provide insights into the main sources of uncertainty that affect the building performance under extreme winds.

1.5 Organization

This dissertation consists of six chapters. Following the introduction in Chapter 1, Chapter 2 reviews the existing wind vulnerability modeling methodology and the state-of-the-art techniques for building inventory generation.

In Chapter 3, a parametric sensitivity analysis is conducted to evaluate the effects of critical building characteristics on wind fragility for roof sheathing, with the focus on buildings with non-rectangular footprints. Roof archetypes are developed to simplify the modeling of individual buildings, and suggestions for building modeling and data collection are provided.

Chapter 4 describes a building inventory generation model designed to extract building information from remote sensing data. The construction of the training data, as well as the training and evaluation of the model, are explained in detail. Case studies are presented for the application of the inventory generation pipeline at neighborhood and city scales.

In Chapter 5, the wind damage and loss assessment model is elaborated through a case study. The model is applied to the single-family residential building stock in residential communities. The results are discussed in terms of fragility curves and expected annual losses for individual buildings. The aggregated regional wind loss is also compared with the wind loss calculated using building archetypes with average building features.

Chapter 6 summarizes the main contributions and conclusions of this study, as well as the directions of future work based on the limitations of the proposed framework.

CHAPTER 2

LITERATURE REVIEW

This chapter provides an overview of the existing literature related to classification and modeling methods of the single-family residential building stock. Section 2.1 summarizes the critical building characteristics that are identified to have a significant impact on the building performance under extreme winds. Section 2.2 describes the building models employed by existing wind loss frameworks, and discusses the limitations of those models in terms of building configurations. Furthermore, Section 2.3 reviews the state-of-the-art techniques for collecting building metadata, which can be adopted to create high-resolution building inventories.

2.1 Major Building Characteristics for Single-family Houses

This section introduces the externally visible building characteristics (depicted in Fig. 2.1) that were identified to have critical effects on building performance under high winds. The effect of each building feature is discussed based on available wind tunnel tests, post-disaster damage data, and probabilistic vulnerability assessments. Additionally, typical configurations for each building feature for single-family dwellings in the United States are introduced. Efforts to evaluate the impact of individual building characteristics on wind loads and building performance facilitate the development of a building data collection and modeling methodology.

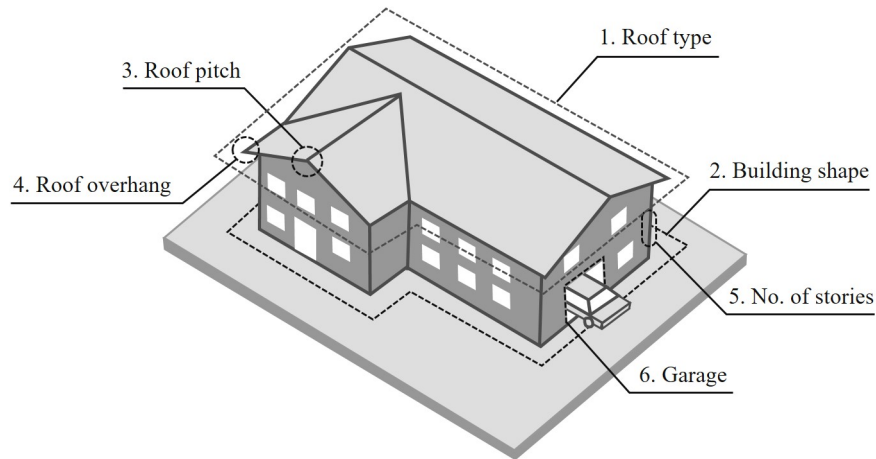


Figure 2.1: Critical building characteristics for wind vulnerability modeling of single-family houses

Roof type

In the hurricane-prone region of the United States, gable and hip roofs are the dominant roof types for single-family residential buildings (Vickery, 2006; Crandell et al., 1993). Post-disaster studies (Crandell et al., 1993; Brown-Giammanco et al., 2018) show that hip roofs suffer significantly less damage than gable roofs, due to differences in wind pressure distribution and roof framing structure (Meecham et al., 1991). The peak negative pressures on gable roofs are substantially higher than those on hip roofs, as concluded in previous wind tunnel tests (Gavanski et al., 2013; Xu and Reardon, 1998; Shao et al., 2018).

Building shape

Most single-family houses in the United States have non-rectangular footprints (Meloy et al., 2007). The building shape affects the layouts of both roof and wall structures. Recent studies conducted wind tunnel tests on low-rise buildings with complex-shaped roofs (e.g., L- and T-shaped roofs) (Shao et al., 2018; Parackal et al., 2016; Uematsu et al., 2022; Sarma et al., 2023). The experimental results show distinctive magnitude and distribution of wind pressures between non-rectangular and rectangular roofs with the same roof type (gable/hip).

Additionally, Sarma et al. (2023) assessed the wind vulnerability of roof sheathing on gable roofs with different building shapes. It is concluded that complex gable roofs have substantially different wind vulnerability compared rectangular-shaped gable roofs. However, due to limited number of models assessed, the effect of building shape on roof vulnerability remains unclear. On the other hand, researchers have not paid attention to the wind load and vulnerability of non-rectangular wall structures for low-rise buildings.

Roof pitch

The roof pitch for single-family houses in the coastal area has a wide range. Based on a survey of the national distribution of typical roof pitch values conducted by the NAHB Research Center (Gurley et al., 2005), fractions of site-built houses with roof pitches lower than 5/12, between 5/12 and 6/12, and over 6/12 are 17%, 40%, and 43%, respectively. It was observed in the post-disaster survey of Hurricane Harvey (Brown-Giammanco et al., 2018) that roof slope had a notable impact on roof sheathing and roof underlayment damage. Based on the investigation of 213 single-family dwellings, the failure frequency for roof sheathing is 16% lower for steep roofs (greater than 7/12) than for moderate-slope roofs (2/12 - 7/12). The effect of roof pitch on roof pressures was also evaluated by wind tunnel tests (Xing et al., 2018; Xu and Reardon, 1998). Xing et al. (2018) conducted experiments on gable-roof building models of 11°, 22°, and 31° roof pitch and concluded that gable roofs with a lower roof pitch experience higher suction pressures. Xu and Reardon (1998) evaluated effect of roof pitch on wind pressure on hip roofs using building models of 15°, 20°, and 30° roof pitch. The results showed that the increase in roof pitch resulted in higher peak suction on hip roofs. Based on the post-disaster data and wind tunnels results, roof pitch has a significant effect on roof damage for both gable and hip roofs, even with frequently used roof pitch angles.

Roof overhang

Roof overhangs are frequently used for single-family houses for rainfall protection and shading purposes. The typical size of an overhang ranges from 12 inches and 24 inches. Wind tunnel tests conducted by Wiik and Hansen (1997) and Mostafa et al. (2022) show that the overhang experiences higher uplift wind forces compared to other areas of the roof, and larger overhangs suffer higher suction. Li (2005) evaluated the effect of overhangs on extreme wind fragility for roof sheathing. The fragility analysis demonstrates that houses with roof overhangs have a significantly higher probability of roof sheathing damage than those without overhangs.

Number of stories

Single-family houses are typically one- or two-story buildings. The number of building stories is associated with multiple building characteristics. First, buildings with more stories have greater building height, inducing higher wind pressure on the roof. Li (2005) calculated the roof sheathing fragility for both one- and two-story building models and concluded that roof height had minor effect on roof sheathing fragility. In addition, a post-disaster study by Crandell et al. (1993) showed that two-story buildings did not suffer significantly more severe roof damage than one-story buildings.

Second, buildings with more stories have substantially more windows, which increases the probability of window damage due to wind pressure and wind-borne debris. The breakage of the windows can result in water ingress (Pita et al., 2012) and the change in internal pressures (Liu and Saathoff, 1981), which can trigger interior damage and progressive damage of other envelope components. These effects were supported by the post-disaster site investigation by Crandell et al. (1993), which showed that two-story buildings experienced significantly higher damage ratio than single-story buildings for building envelope damage and interior damage due to water intrusion.

Garage

As shown in Fig. 2.2, there are three common types of garage for single-family houses in the United States: attached garages, detached garages, and carports. Among these types, only attached garage is considered for the wind vulnerability modeling methodology developed by previous studies (Vickery, 2006; Pinelli et al., 2011; Peng, 2013; Chung Yau et al., 2011). As the largest opening on the single-family houses, garage door is a weak link in the building system. Failure of the garage door changes the internal wind pressure dramatically, and triggers the damage of other building components (Crandell et al., 1993).

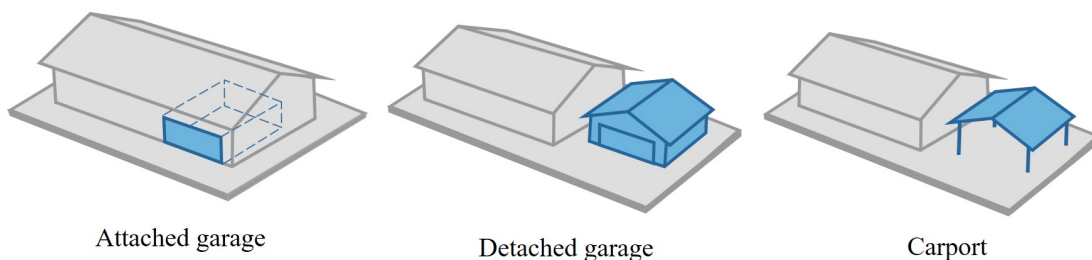


Figure 2.2: Typical garage types for single-family houses in the United States

2.2 Wind Vulnerability Modeling of Single-family Houses

This section reviews the wind vulnerability modeling of single-family houses using probabilistic methods, with a focus on the building attributes considered in existing models. The capabilities and limitations of existing models are discussed, as well as potential improvements that can be implemented to increase the accuracy of damage prediction.

The wind vulnerability modeling of single-family houses generally requires two types of building-related variables: building configuration and structural configuration. Building configuration refers to the general building characteristics, such as the building area, roof type, and number of stories. Structural configuration represents the types and capacities of building components and structural connections. Typical building components considered for

the physical damage modeling of wood-frame single-family houses are illustrated in Fig. 2.3.

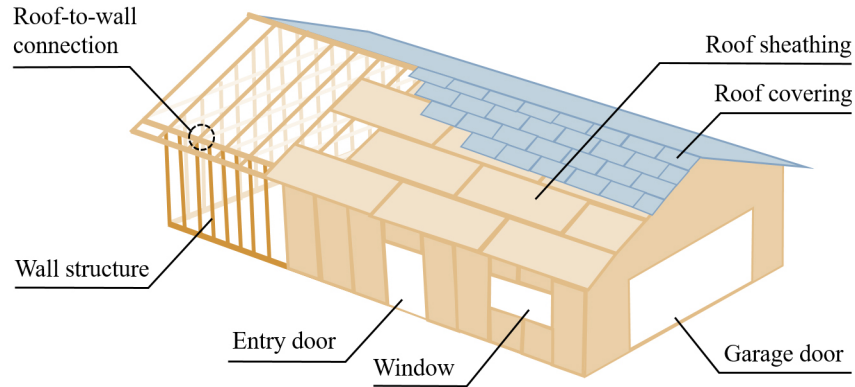


Figure 2.3: Building components considered for wind damage calculation for wood-frame single-family houses

Existing regional wind loss models, including the Federal Emergency Management Agency (FEMA) HAZUS-MH model (Vickery, 2006) and the Florida Public Hurricane Loss Model (FPHLM) (Pinelli et al., 2011; Hamid et al., 2011), implement wind damage simulations on building archetypes designed based on typical building configurations. Variations of critical building characteristics, including roof type (gable/hip), number of stories (one/two), and garage condition (Y/N), are considered in the building archetypes for single-family houses. When determining the aggregated regional loss, the model houses are mapped to the building stock based on the statistical distribution of the aforementioned features at the regional level (e.g., census-tract level). Due to limited building inventory data and a lack of understanding regarding the impact of architectural features, variations of many critical building attributes (e.g., building shape and roof pitch) are neglected. As a result, rectangular-shaped building models with simple roof shapes and a single roof pitch value are adopted for the building archetypes. In terms of the structural configuration, component resistances are usually estimated based on the building location and construction year (Hamid, 2021; Peng, 2013), which are correlated with building design codes and local retrofit policies.

Extensive efforts were devoted to improving the wind vulnerability modeling methodol-

ogy for rectangular-shaped low-rise residential buildings. Lin and Vanmarcke (2010) developed the debris risk analysis methodology for quantifying the failure probability of openings due to wind-borne debris. Ji et al. (2020) introduced a simplified approach to simulate the progressive damage process of the building envelope due to changes in internal wind pressures. Chung Yau et al. (2011) integrated assessments of wind pressure damage and wind-borne debris effect to estimate the wind loss for residential neighborhoods. Unnikrishnan and Barbato (2016) developed a performance-based hurricane engineering framework with multilayer Monte Carlo Simulation to compare building performance with different retrofit strategies.

On the other hand, only a limited number of studies have examined the wind performance of non-rectangular residential buildings, with the majority of assessments focusing on roof components. Amini and van de Lindt (2014) developed tornado fragilities for the roof system of four complex gable-roofed buildings and one simple hip-roofed building using wind loads calculated based on ASCE 7-10 (ASCE, 2010). Masoomi et al. (2018) conducted fragility analysis on the same set of building models considering both straight-line winds and tornadoes, using ASCE 7-10 (ASCE, 2010) and ASCE 7-16 (ASCE, 2016). Stewart et al. (2018) developed fragility curves for metal roof sheeting on a complex hip-roof building using wind pressure data obtained from wind tunnel tests. Similarly, Sarma et al. (2023) assessed roof sheathing vulnerabilities for seven gable-roof building models with different building shapes using wind pressure coefficients derived from wind tunnel tests.

In summary, existing wind vulnerability models are developed based on simplified and idealized building models, which can lead to errors and biases in the damage and loss predictions. However, recent advancements in risk assessment methodologies for irregular buildings have made it possible to integrate non-rectangular building models into the wind risk assessment framework. This will provide a more realistic description of the building stock and improve the accuracy of damage and loss estimation.

2.3 Building Data Collection Techniques

As introduced in Section 2.2, wind vulnerability modeling of single-family houses requires detailed descriptions of exterior building features. Existing regional wind loss models mainly rely on publicly available datasets (e.g., tax appraisers' databases) to derive the statistical distribution of building attributes based on selected geographic area units (e.g., census tracts). However, many critical building characteristics (e.g., roof type) are missing in such datasets (Pita et al., 2008). Post-disaster studies, which mainly focus on damaged buildings, provide a means of collecting building inventory data. In a case study conducted by Vickery (2006), roof type and number of stories of 1,633 homes were manually labeled using aerial images to classify the residential building stock in Florida. Building inventories generated through manual data collection process are usually limited to hundreds to thousands of buildings, which are not sufficient to produce statistically significant results and can cause bias when extrapolated to large-scale building stocks.

Recent advancements in machine learning have provided powerful tools to extract detailed building information using predictive modeling and image processing. Machine learning-based building data collection methods can be classified into two major types. One type of approach is predicting unknown building characteristics using other correlated building variables. This type of approach is widely used for missing data imputation. Pita et al. (2011) applied Bayesian Belief Networks and Classification and Regression Trees to impute missing roof-type data using building characteristics such as construction year and building value. Taghinezhad et al. (2020) examined several regression models for imputing missing first floor elevation data. The statistical models are easy to train and can be used to predict both categorical and numerical variables. However, the implementation of such methods heavily rely on the availability of other building information. Moreover, building features, like building value, are correlated with building location, which reduce the prediction accuracy when applied to different areas (Pita et al., 2011).

Another approach is extracting building information using remote sensing data with Convolutional Neural Networks (CNNs) through Representation Learning (Bengio et al., 2013). Representation learning extracts the features automatically through its learning process, without the need for hand-crafted features, thus offering higher generalizability than statistical and hand-crafted features which might not generalize to unseen data well (El-Hariri et al., 2019). Deep learning-based data collection methods for various building attributes have been developed by previous studies through image classification, object detection, and semantic segmentation. CNNs were trained to predict roof type using satellites imagery (Buyukdemircioglu et al., 2021; Wang et al., 2021; Alidoost and Arefi, 2018). Kang et al. (2018) developed an automatic workflow for building instance classification using street view images. In addition, extensive studies have been focused on roof segmentation using satellite and aerial imagery (Wu et al., 2018; Merabet et al., 2015), and building facade segmentation using street view images (Dai et al., 2021). Previous experiments have demonstrated that CNNs could be used to generate building inventories efficiently with high accuracy. Nevertheless, low-quality remote-sensing data are frequently encountered due to various reasons (e.g., tree occlusion), which reduces the robustness of classification or segmentation (Jayaseeli and Malathi, 2020; Zambanini et al., 2020). Considering the complex nature of residential environments, the generalizability and effectiveness of deep learning-based methods for producing building metadata remain unclear. Additional pre- and post-processing steps are necessary to identify low-quality remote-sensing data and impute the resulting missing data in order to create reliable and comprehensive building inventories.

Facilitated by publicly available remote sensing databases (e.g., Google Maps), deep learning models can be adopted to predict building features critical for wind risk assessments. A machine learning-aided model can be developed to construct large-scale and high-resolution building inventories. These enriched building inventories can enhance the understanding of the residential building stock and support more detailed building modeling than existing models.

CHAPTER 3

SENSITIVITY ANALYSIS FOR EXTREME WIND FRAGILITY OF ROOF SHEATHING

This chapter presents a parametric sensitivity analysis for evaluating the effects of critical roof features on wind fragility for roof sheathing. The analysis results are used to identify the relative importance of building characteristics for wind vulnerability modeling, which facilitates the development of building archetypes and building data collection methods. Section 3.1 introduces the background and motivation of the sensitivity analysis. Section 3.2 describes the building models used for the fragility analysis, followed by the explanation of the fragility modeling methodology in Section 3.3. In Section 3.4, fragility curves for building models with different roof shapes and roof pitches are presented, and the results are discussed in terms of failure probabilities and fragility parameters. In the end, roof modeling approaches for assessing the building's wind vulnerability are provided in Section 3.5, and the limitations of the analysis are discussed in Section 3.6.

3.1 Introduction

Damage to the roofs of single-family residential buildings is frequently observed in extreme wind hazard events. Uplift pressure acting on roofs can remove roof sheathing panels from roof framing. Loss of a single piece of the roof sheathing can cause rainwater penetration, resulting in severe interior damage and corresponding content losses (Sparks et al., 1994). Moreover, the loss of roof sheathing can induce sudden internal pressurization and affect the

wind pressure applied on other building components (Liu and Saathoff, 1981). Hence, accurately predicting the performance of roof sheathing is critical for damage and loss estimation of the whole building structure.

Based on functional and aesthetic needs, most single-family residential buildings in the United States have non-rectangular footprints with resulting complex roof configurations. The roof pitch for residential buildings can vary from 3:12 (14°) to 12:12 (45°) (Brown-Giammanco et al., 2018). Previous research on the reliability of roof sheathing subjected to high wind has mostly focused on simple roof shapes with rectangular building plans (Ellingwood et al., 2004; Lee and Rosowsky, 2005; Li, 2005; van de Lindt and Dao, 2009). Only a limited number of studies considered building models with complex roof shapes and non-rectangular building plans (Amini and van de Lindt, 2014; Masoomi et al., 2018; Stewart et al., 2018; Sarma et al., 2023). Nevertheless, due to the limited number of building models, the effects of roof shape and roof pitch on roof sheathing fragilities remain unclear. Consequently, this study conducts a quantitative evaluation of the effects of roof shape and roof pitch on roof sheathing fragility by assessing a large number of realistic building models with various roof shapes and roof pitches. The goal of this analysis is to provide guidance for improving the vulnerability modeling for single-family houses and to explore potential simplifications for site-specific building modeling.

3.2 Building Models

Two sets of building models were used to evaluate roof type and roof pitch effects on roof sheathing fragility, respectively. The first set includes 47 building models (5 rectangular gable-roofed, 18 complex gable-roofed, 1 rectangular hip-roofed, and 23 complex hip-roofed cases), designated Types 1-47 (Figs. 3.1 and 3.2). The 47 building models were classified into Groups 1-12 based on roof complexity, with the number of ridgelines for gable roofs (one to five) and the number of roof corners for hip roofs (four to nine) used as the primary features

representing the roof complexity. Groups 1-2 and 3-6 represent buildings with rectangular gable roofs and complex gable roofs, respectively. Groups 7 and 8-12 represent buildings with rectangular hip roofs and complex hip roofs, respectively. Building models were designed to have similar plan areas and dimensions. Roof configurations and building properties of building models were developed based on common practice in residential construction. Roof sheathing panels are placed following a staggered pattern with 50% offset. They are intended to be representative of most single-family houses in hurricane-prone areas of the United States. Table 3.1 presents the properties of building model set 1. The building dimensions and roof configuration for Structure Type 6 are shown in Fig. 3.3 as an example. Roof dimensions and panel layouts for gable- and hip-roofed building models are shown in Fig. 3.1 and Fig. 3.2, respectively.

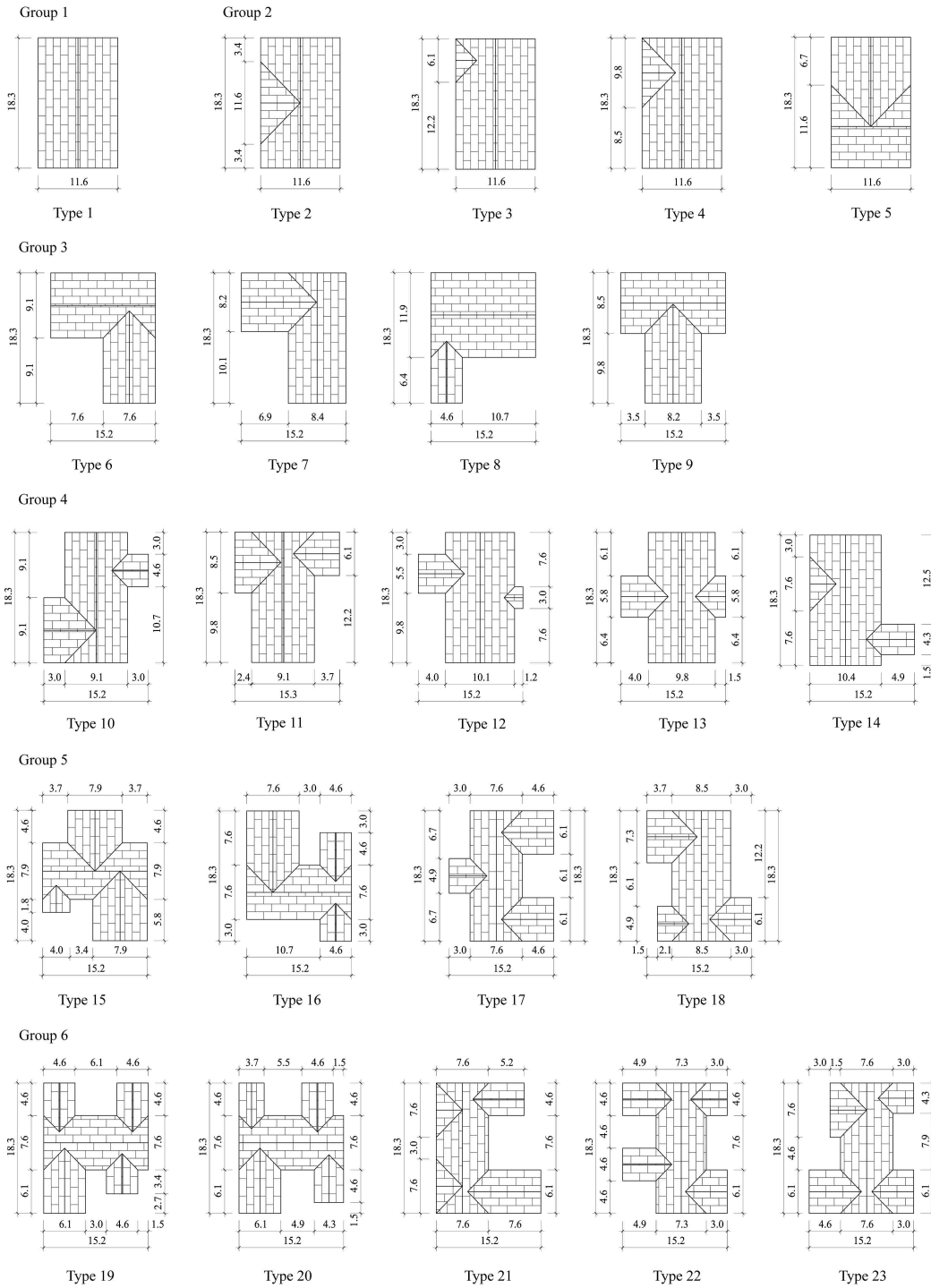


Figure 3.1: Dimensions and panel layouts for gable-roof building models (all dimensions are given in meters)

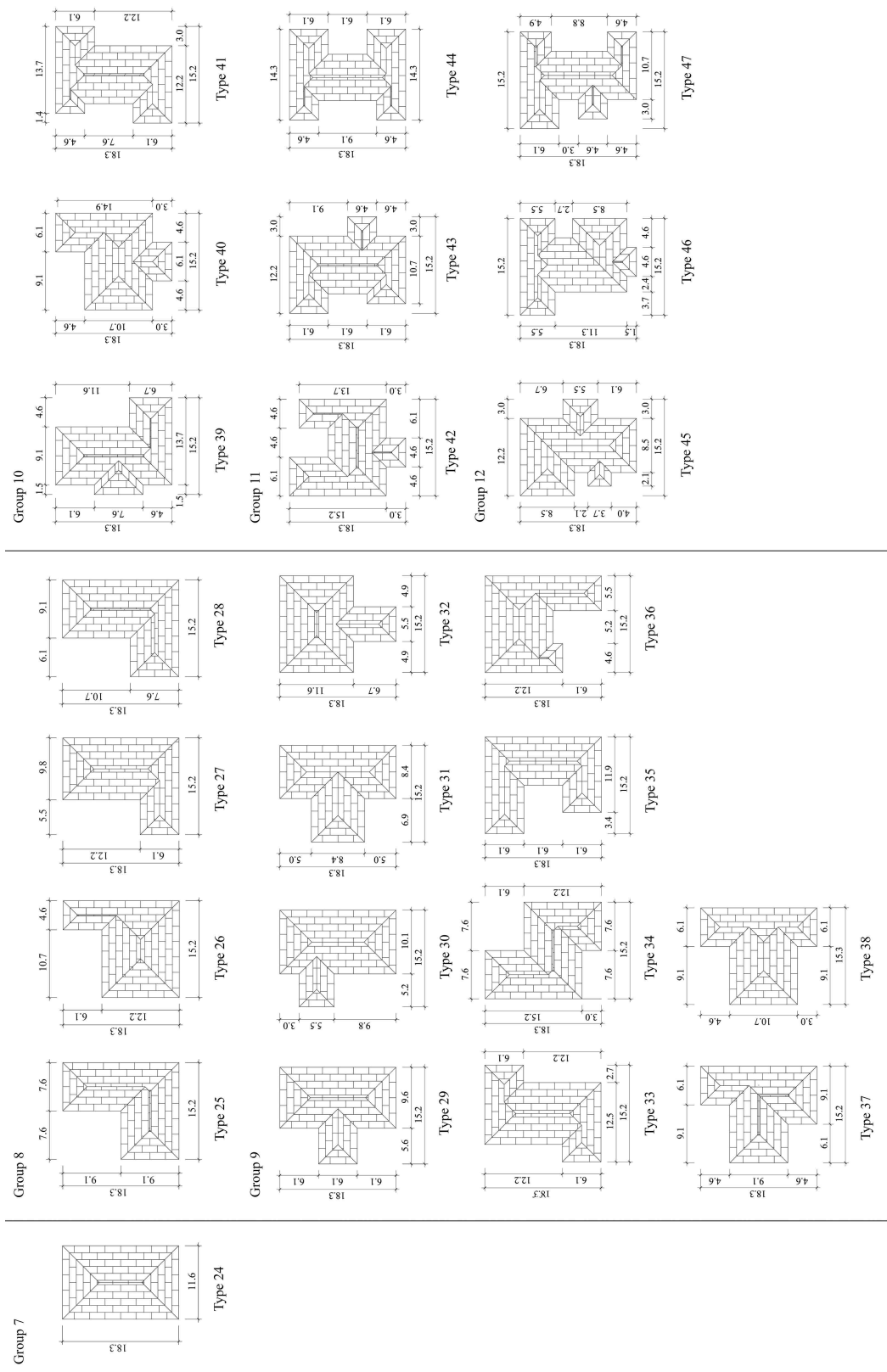


Figure 3.2: Dimensions and panel layouts for hip-roof building models (all dimensions are given in meters)

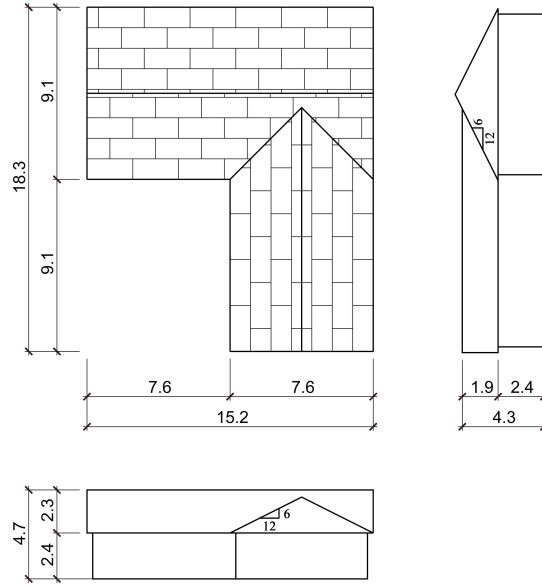


Figure 3.3: Dimensions and roof sheathing layout, Structure Type 6 (all dimensions are given in meters)

Table 3.1: Dimensions and characteristics of building models (Set 1)

Properties	Type 1-5	Type 6-23	Type 24	Type 25-47
Plan dimension (m)	11.0 × 17.7	14.6 × 17.7	11.0 × 17.7	14.6 × 17.7
Roof area (m ²)	211.8	209.0 – 210.9	211.8	209.0 – 213.7
Roof type	Gable	Gable	Hip	Hip
No. of stories	1	1	1	1
Wall height (m)	2.4	2.4	2.4	2.4
Roof slope	6/12 ($\sim 26.6^\circ$)			
Roof framing spacing (m)	0.61	0.61	0.61	0.61
Overhang (m)	0.30	0.30	0.30	0.30

The second set of 40 building models includes four baseline structures, designated Type A-D, with ten different roof pitches (Fig. 3.4). The baseline structures are considered representative of gable- and hip-roofed buildings with rectangular and non-rectangular footprints. The roof pitches vary from 3/12 (14°) to 12/12 (45°), covering commonly used pitch angles in residential buildings. Building properties for the four baseline models are summarized in Table 3.2.

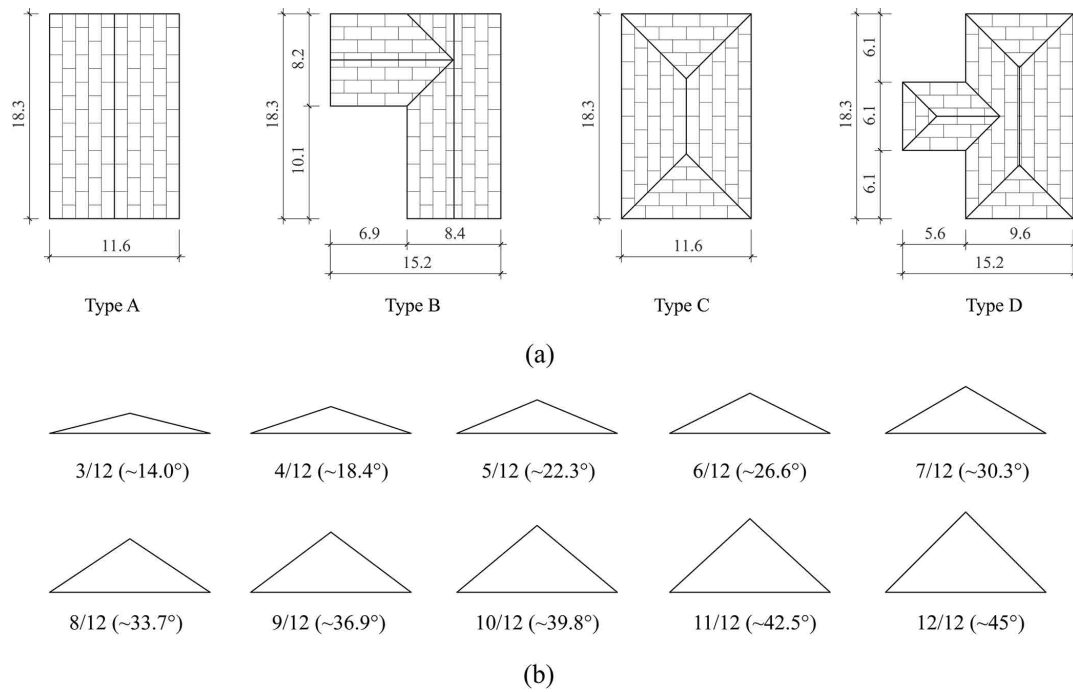


Figure 3.4: Characteristics of building models (Set 2) (a) Roof configurations and dimensions for baseline building models. The panel layouts are shown for 4:12 pitched roofs. (b) Selected roof pitch (all dimensions are given in meters)

Table 3.2: Dimensions and characteristics of building models (Set 2)

Properties	Type A	Type B	Type C	Type D
Plan dimension (m)	11.0 × 17.7	14.6 × 17.7	11.0 × 17.7	14.6 × 17.7
Roof type	Gable	Gable	Hip	Hip
No. of stories	1	1	1	1
Wall height (m)	2.4	2.4	2.4	2.4
Roof framing spacing (m)	0.61	0.61	0.61	0.61
Overhang (m)	0.30	0.30	0.30	0.30

3.3 Fragility Modeling Methodology

3.3.1 Damage states

The failure of roof sheathing due to wind load is usually caused by negative wind pressure (suction) acting on the panel, which causes multiple nail withdrawals and leads to the removal of roof sheathing from roof framing. The limit state for the uplift of an individual roof sheathing panel can be expressed by

$$g(R, W, D) = R - (W - D) \quad (3.1)$$

where R = uplift capacity of roof sheathing, W = uplift wind load acting on the roof sheathing, D = dead load. The failure of individual roof sheathing is defined as $g(\cdot) < 0$. For the fragility of a roof sheathing system, which consists of multiple roof panels, five damage states were considered, which are consistent with previous studies (Lee and Rosowsky, 2005; Amini and van de Lindt, 2014): ($DS1$) no roof sheathing failure, ($DS2$) one roof sheathing panel fails, ($DS3$) more than one, and less than or equal to 10% of roof sheathing panels fail, ($DS4$) more than 10%, and less than or equal to 25% of roof sheathing panels fail,

(*DS5*) more than 25% of roof sheathing panels fail. Roof sheathing with smaller panel size has higher wind uplift capacity (Lee and Rosowsky, 2005). As shown in Figs. 3.1 and 3.2, roof panels with small dimensions are frequently observed at the edge of roof segments for complex roofs. Due to lack of experimental data for the uplift capacity of non-standard roof panels, roof sheathing panels smaller than 6 sq ft are neglected in the fragility analysis.

3.3.2 Fragility analysis

Fragility analysis was applied to evaluate the performance of roof sheathing under high wind incorporating the uncertainties in loads and resistance. Following the method described by Masoomi et al. (2018), wind fragilities for the roof sheathing system can be defined as the conditional probability of exceeding a specific damage state under a given wind speed v

$$Fr(V) = P[DS > ds_i | V = v] \quad (3.2)$$

The fragility curves were developed using Monte Carlo simulations with 10,000 samples. Figure 3.5 summarizes the main steps of the Monte-Carlo simulation for the roof sheathing fragility assessment.

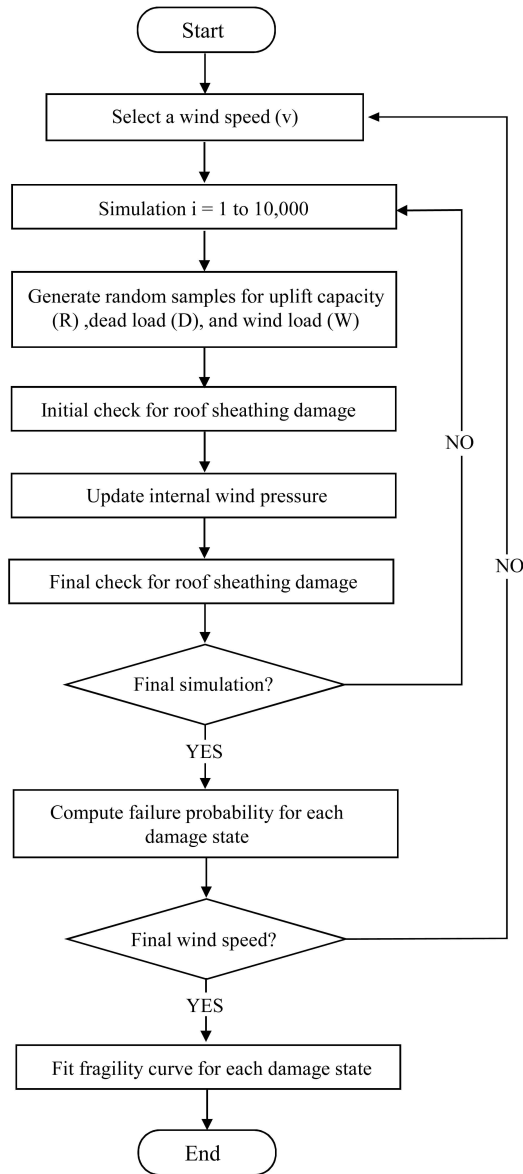


Figure 3.5: Simulation procedure for roof sheathing fragility assessment

3.3.3 Uplift capacity

For this study, the statistics of the wind-uplift capacity (R) of roof sheathing were obtained for $13 \text{ mm} \times 1.2 \text{ m} \times 2.4 \text{ m}$ ($1/2 \text{ in} \times 4 \text{ ft} \times 8 \text{ ft}$) oriented strand board (OSB) fastened to nominal $51 \text{ by } 102 \text{ mm}$ ($2 \text{ by } 4 \text{ in.}$) Southern Yellow Pine (SYP) lumber spaced 24 in.

on-center, using 8d common nails (3.33 mm (0.131 in.) diameter, 63.5 mm (2.5 in.) long). The nail spacing is 6 in. along the edge of the panel and 12 in. at interior locations. The statistics of uplift capacity were obtained from experimental results by Datin et al. (2011) (Table 3.3). The uplift capacities of roof panels in the same building are assumed to be partially correlated due to similar environment, material, and construction conditions (He and Hong, 2012). For each building sample, the resistance for roof panels is generated from a multivariate lognormal distribution with correlation coefficients equal to 0.4, as suggested by Peng (2013).

Table 3.3: Resistance (R), dead load (D), and wind load (W) statistics

Parameters	Category	Mean	COV	Distribution	Reference ^a
R	8DC6/12	129.4 (psf)	0.12	Lognormal	1
	ccSPF	154.9 (psf)	0.17	Lognormal	1
D		3.5 (psf)	0.1	Normal	2
K_z	One-story	0.82	0.14	Normal	2
	Two-story	0.84	0.14	Normal	2
K_d	C&C	0.89	0.16	Normal	2
GC_{pi}	Enclosed	0.15	0.33	Normal	2
	Partially enclosed	0.46	0.33	Normal	2
K_{zt}		Deterministic (1.0)			2

^a References: 1 = Datin et al. 2011; 2 = Lee and Rosowsky 2005.

3.3.4 Dead load and wind load

The dead load (D) considered in Eq. 3.1 is the self-weight of the roof sheathing panel. The self-weight of the roof cover, which is assumed to be an asphalt shingle in this study, is

negligible compared to the weight of roof sheathing. The dead load is assumed to remain constant in time and is modeled by a normal distribution (Lee and Rosowsky, 2005). The statistics of dead load are summarized in Table 3.3.

In this study, wind loads acting on individual roof panels were calculated based on ASCE 7-16 (ASCE, 2016). Wind provisions in ASCE 7-16 focus solely on rectangular buildings, and buildings with non-rectangular footprints are not included. Shao et al. (2018) conducted wind tunnel experiments on L- and T-shaped structures and concluded that wind provisions in ASCE 7 standard could provide a reasonable estimation of wind pressures acting on complex-shaped roofs. In ASCE 7-16 (ASCE, 2016), roof sheathing is modeled as components and cladding (C&C). The wind pressures on C&C of low-rise buildings were determined by the following equation:

$$W = q_h(GC_p - GC_{pi}) \quad (3.3)$$

where q_h = velocity pressure evaluated at mean roof height; GC_p = external pressure coefficient; GC_{pi} = internal pressure coefficient. The nominal value of the external pressure coefficient (GC_p) for roof panels was determined using the weighted-average method explained by Lee and Rosowsky (2005). GC_p values for different wind pressure zones are functions of the roof slope given in ASCE 7-16 (ASCE, 2016). The velocity pressure, q_h , was determined from ASCE (2016):

$$q_h = 0.00256K_zK_{zt}K_dV^2(lb/ft^2); V \text{ in } mi/h \quad (3.4)$$

where K_z = velocity pressure exposure coefficient; K_{zt} = topographic factor; K_d = wind directionality factor; V = 3-sec gust speed at 10 m (33 ft) above ground in open terrain. The velocity pressure exposure coefficient (K_z) is determined based on the mean roof height and the exposure category. For this study, the exposure category is assumed to be Exposure C for open terrain with scattered obstructions. Wind pressures for C&C were determined based on the assumption that wind comes from any possible direction. The wind directionality factor (K_d) was applied to account for the reduced probability of maximum winds coming

from any direction and maximum wind pressure occurring for any given wind direction. It is assumed that GC_p follows a normal distribution with the mean-to-nominal value equal to 0.95 and a coefficient of variation equal to 0.12 (Ellingwood and Tekie, 1999). The wind zones for GC_p on complex roofs adopted in this study are illustrated in Fig. 3.6, which are modified from the wind zones defined for rectangular roofs in ASCE 7-16 (ASCE, 2016). Appendix A summarizes the GC_p values for C&C on gable and hip roofs with different roof pitches. The statistics for other wind load parameters used in this study are summarized in Table 3.3.

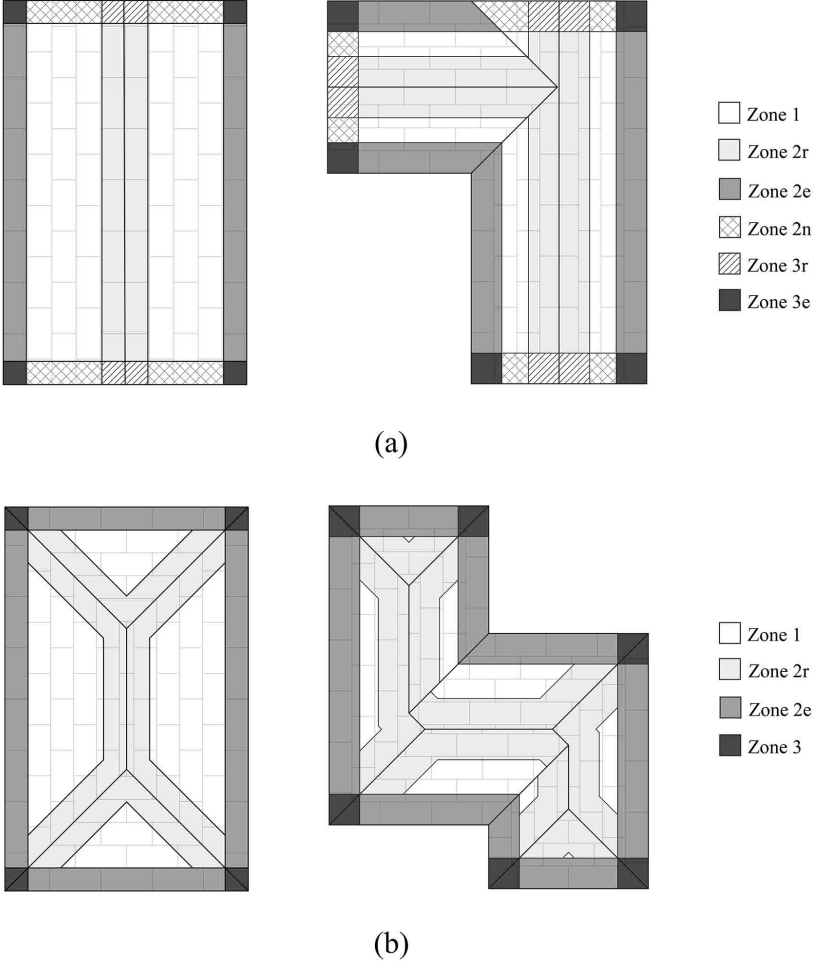


Figure 3.6: Wind pressure zones for GC_p for C&C on roofs: (a) Gable roofs; (b) Hip roofs

Openings in the building envelope created by failed roof sheathings are likely to change the internal pressure (Stewart et al., 2018; Qin and Stewart, 2019; Sarma et al., 2023). The approach proposed by Lee and Rosowsky (2005) is applied in this study to consider this effect. Damage conditions for roof sheathings are first checked with the internal pressure coefficient (GC_{pi}) for an enclosed building. If at least one roof sheathing fails, the internal pressure is recalculated based on a partially enclosed structure. The damage conditions for undamaged roof panels are checked with the updated internal pressure. The positive GC_{pi} values, which result in the worst loading condition for roof sheathing, are used in this study. The statistics for GC_{pi} and other wind load parameters used in this study are summarized in Table 3.3.

3.4 Fragility Curves

3.4.1 Effect of roof shape

3.4.1.1 Gable roofs

Figure 3.7 shows the fragility curves for exceeding DS1 and DS4 of all gable-roofed building models (Type 1-23). The median wind speeds of fragility curves (i.e., the wind speed associated with 50% failure probability) of all gable-roofed buildings are shown in Fig. 3.8 to illustrate the differences in fragilities between different building models. All building models have very similar standard deviations, and the fragility curves with higher median values have lower failure probability given the same wind speed. As shown in Figs. 3.7 and 3.8, the failure probabilities increase with the higher complexity of roof shapes. The rectangular gable roofs (Group 1-2) experience lower failure probabilities than non-rectangular gable roofs (Group 3-6), and the difference increases for more severe damage states. For rectangular gable roofs, the simple gable roof (Group 1) is less vulnerable than cross-gable roofs (Group 2), and the difference decreases drastically for more severe damage states. For non-

rectangular gable roofs, the structures in the same group show similar performance under high winds, as shown in Fig. 3.7. The probability of no roof sheathing failure for Type 1 (rect./ 1 ridgeline) is 13% higher than Type 2 (rect./ 2 ridgelines), and 36% higher than Type 21 (comp./ 5 ridgelines) for a wind speed of 63 m/s (142 mph). The probability of at least 25% roof sheathing failure for Type 1 is 35% lower than Type 20 (comp./ 5 ridgelines) for a wind speed of 73 m/s (163 mph). The aforementioned difference in fragility curves demonstrates that the effect of roof shape on roof sheathing fragility is considerable for gable roofs. The increased roof sheathing failure probabilities with more complex gable roofs can be explained by the distribution of wind pressure on gable roofs. It was observed in wind tunnel tests conducted on rectangular and non-rectangular gable-roof buildings (Marshall, 1975; Gavanski et al., 2013) that peak suction appears along roof ridges, roof edges, and roof corners. A larger portion of the roof panels is located in the high wind pressure zones for more complex gable roofs, which results in overall higher wind loads and a higher likelihood of experiencing roof sheathing damage for gable roofs with higher complexity.

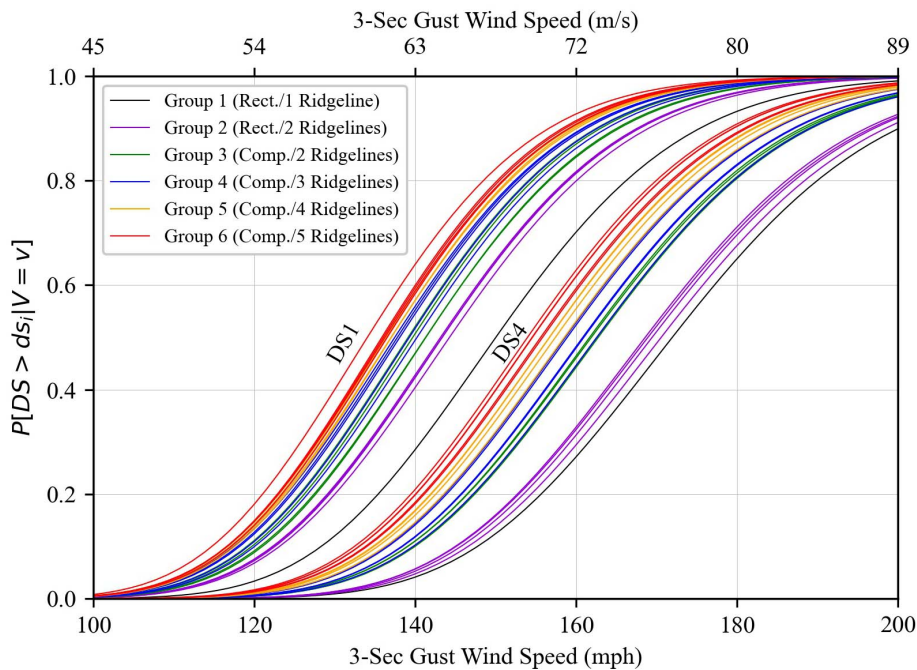


Figure 3.7: Fragility curves for gable-roofed buildings (Type 1-23)

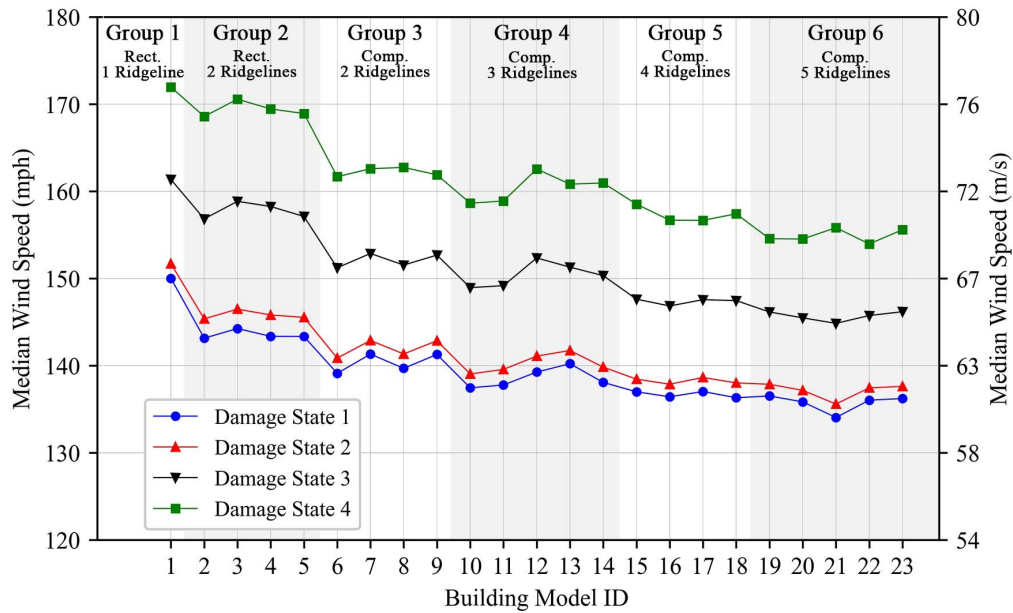


Figure 3.8: Median wind speed of fragility curves for gable-roofed buildings (Type 1-23)

3.4.1.2 Hip roofs

Figure 3.9 shows the fragility curves for hip-roofed buildings (Type 24-47). The median wind speeds for fragility curves for the four damage states are plotted in Fig. 3.10. The median wind speeds for fragility curves are similar for non-rectangular hip-roofed buildings (Groups 8-12). As shown in Fig 3.9, the fragilities show higher variance for more severe damage states (DS3 and DS4). Notable differences in fragilities can be observed between the rectangular hip-roofed building (Type 24) and non-rectangular hip-roofed buildings (Type 25-47) for DS3 and DS4. The probability of at least 25% roof sheathing failure for Type 24 (4 roof corners) is 9% lower than Type 37 (5 roof corners) for a wind speed of 78 m/s (174 mph). In contrast to the gable-roofed buildings, all non-rectangular hip-roofed buildings show similar wind fragilities regardless of the roof complexity. Different effects of roof shape on roof sheathing fragility for gable and hip roofs might be caused by different roof configurations and wind pressure distributions. As shown in Fig. 3.6, the roof panels near the hip lines

and roof edges cover the majority of the roof. The variation of peak negative wind pressures between different wind zones for hip roofs is lower than the gable roofs. When determining the wind loads on roof sheathings for hip roofs, the differentiation between different roof zones is less critical than other building characteristics, like roof height and roof slope, as concluded by Gavanski et al. (2013). In contrast, the differentiation of roof zones was found to be crucial for gable roofs.

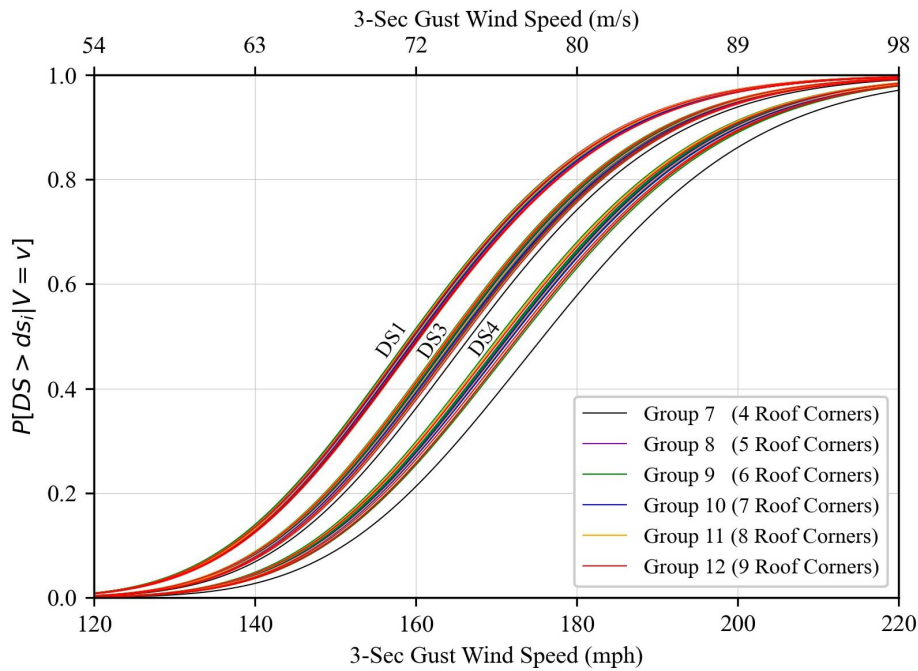


Figure 3.9: Fragility curves for hip-roofed buildings (Type 24-47)

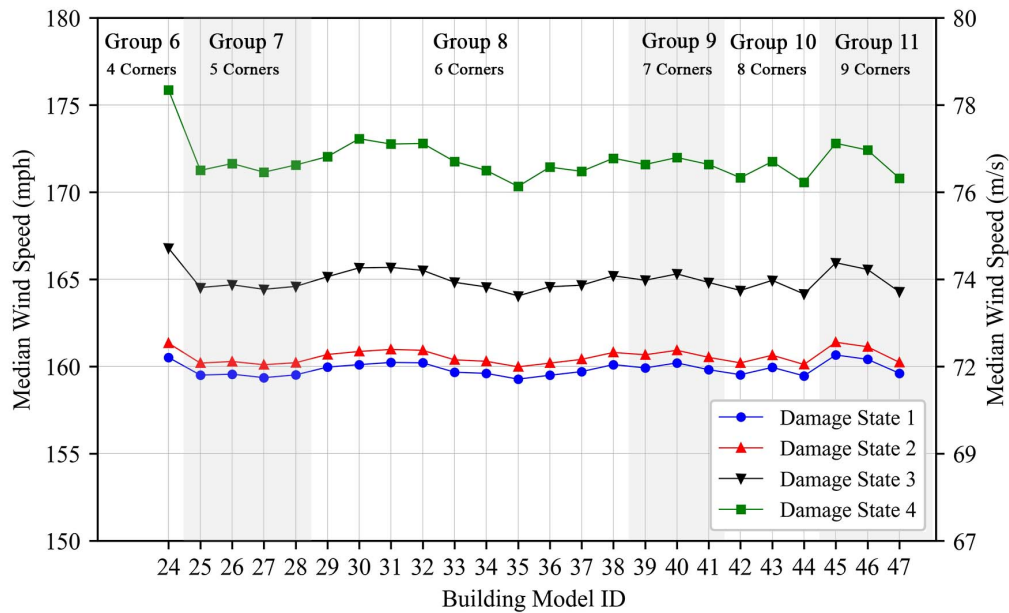


Figure 3.10: Median wind speed of fragility curves for hip-roofed buildings (Type 24-47)

3.4.1.3 Gable versus hip roofs

Figure 3.11 shows the fragility curves for all gable-roof buildings are to the left of those for hip-roof buildings, which indicates that roof sheathing on gable roofs is more likely to be damaged than hip roofs despite variation in roof shapes. It is consistent with the observations from post-disaster surveys that hip roofs had better performance than gable roofs during hurricanes (National Research Council, 1991; FEMA, 1992). As depicted in Fig 3.11, the variance of fragilities for gable roofs with different roof configurations is substantially higher than for hip roofs. As summarized in the post-disaster survey of Hurricane Andrew (Crandell et al., 1993), hip roofs experienced significantly less damage than gable roofs regardless of building shapes, and hip-roof buildings showed less variance in roof damage ratio compared to gable-roof buildings. Brown-Giammanco et al. (2018) assessed the roof sheathing damage for residential buildings after Hurricane Harvey. Roof structure damage was mainly observed in neighborhoods experiencing 54 m/s (120 mph) to 63 m/s (140 mph) gust wind. Gable

roofs showed 18% higher roof sheathing damage frequency for than hip roofs. As shown in Fig. 3.11 (a), for a wind speed of 58 m/s (130 mph), the probability of no roof sheathing failures for a rectangular gable-roof building (Type 1), an L-shaped gable roof (Type 7), and a gable roof with four ridgelines (Type 15) are 8%, 20%, and 29% lower than the T-shaped hip roof (Type 29). Considering the variation in other building characteristics, the roof sheathing damage probabilities predicted by the fragility analysis show good agreement with the observed damage data.

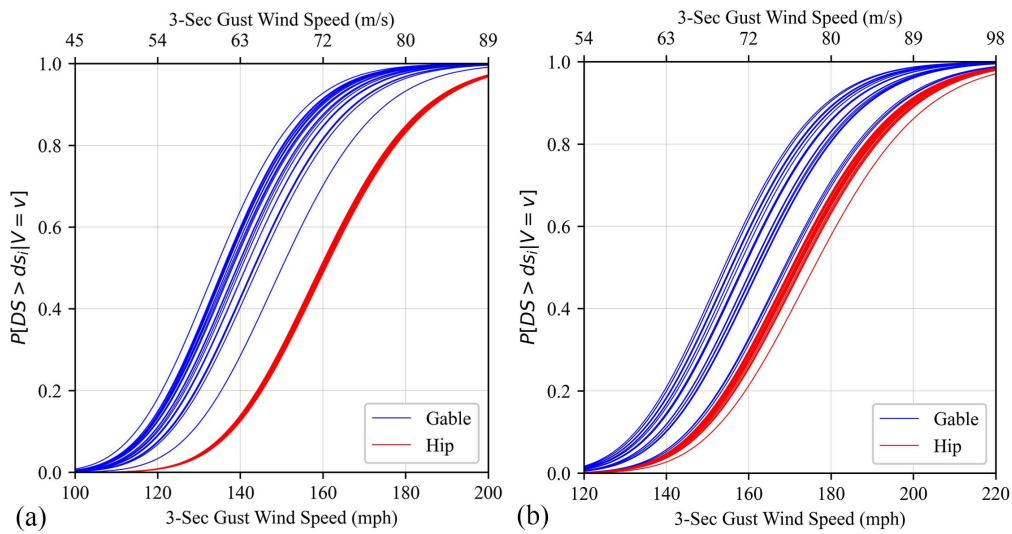


Figure 3.11: Fragility curves for all buildings in building model set 1: (a) DS1; (b) DS4

3.4.1.4 Statistical analysis

To evaluate the statistical significance of the results, analysis of variance (ANOVA) was used to determine if the fragility parameters (median and standard deviation) of different groups are statistically different at the confidence level of 95%. Fragility parameters for building model set 1 and the ANOVA test results are summarized in Appendix B. For gable-roofed building models (Type 1-23), ANOVA analysis shows that rectangular gable-roofed buildings (Group 1-2) have significantly higher median wind speeds for fragility curves than those with non-rectangular roofs (Group 3-6). The median wind speeds for Groups 3 (2

ridgelines) and Group 4 (3 ridgelines) have no significant difference in fragility curves for DS1, DS3 and DS4. The median wind speeds for Group 5 (4 ridgelines) and Group 6 (5 ridgelines) have no significant difference in fragility curves for DS1 and DS2. The median wind speeds differ significantly for fragility curves with other damage states and other groups. As the complexity of roof configuration (i.e., the number of ridgelines) increases, the failure probability of roof sheathing rises significantly.

For hip-roofed building models (Type 24-47), ANOVA test results show that the median wind speeds for the fragility curves for the rectangular hip roof (Type 24) are significantly higher than non-rectangular hip roofs (Type 25-47). For non-rectangular hip roofs (Group 7-11), the fragility parameters do not significantly differ between groups. In summary, rectangular hip roofs have better performance than non-rectangular hip roofs. While for non-rectangular hip roofs, the complexity of roof configurations shows a minor effect on the roof sheathing fragility.

3.4.2 Effect of roof pitch

Figures 3.12 and 3.13 present the fragility curves and corresponding median wind speeds of gable-roofed buildings (Type A and B) with ten different roof pitches. For the rectangular gable-roofed building (Type A), as shown in Fig. 3.12(b), the median wind speeds increase significantly for 5/12 roof pitch compared to those for 3/12 and 4/12 roof pitch. The probability of no roof sheathing failure for Type A of 4/12 roof pitch is 23% lower than 5/12 roof pitch for a wind speed of 63 m/s (142 mph). With the increase of roof pitch beyond 5/12, the median wind speeds change moderately. For the complex gable-roofed building (Type B), two notable increments of median wind speeds can be observed when roof pitch exceeds 4/12 and 6/12. The probability of more than 25% roof sheathing failure for structure Type B of 7/12 roof pitch is 35% and 10% higher than 4/12 and 5/12 roof pitch, respectively, for a wind speed of 72 m/s (161 mph). For roofs steeper than 6/12, similar to Type A, roof pitch shows a moderate effect on roof sheathing fragilities.

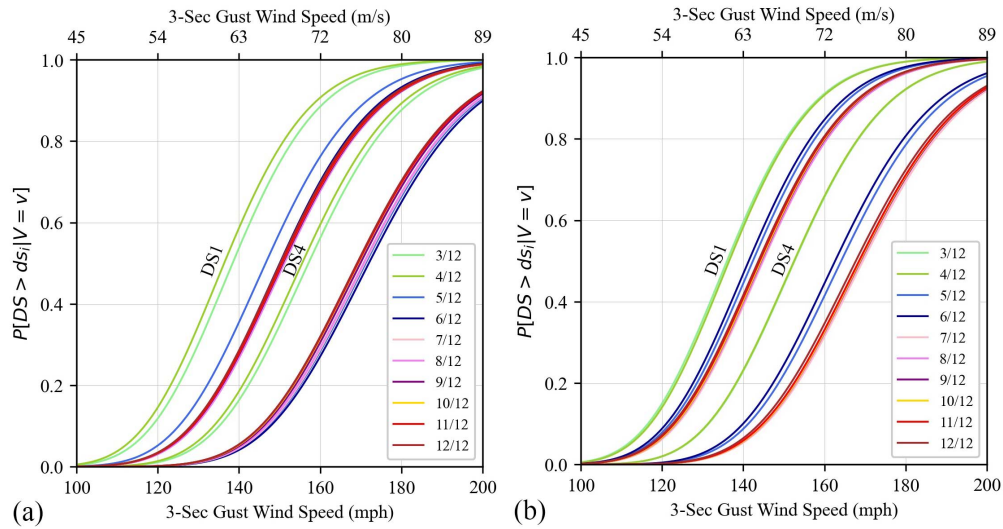


Figure 3.12: Fragility curves for gable-roof buildings with different roof pitches: (a) Structure type A; (b) Structure type B

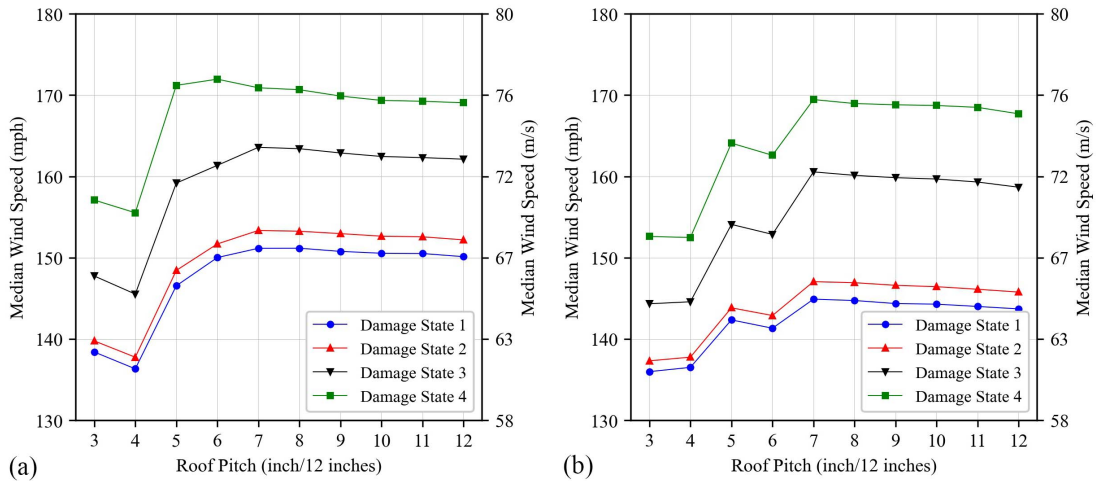


Figure 3.13: Median wind speed of fragility curves for gable-roof buildings: (a) Structure type A; (b) Structure type B

For hip-roofed buildings, similar trends between roof pitch and roof sheathing fragilities for structure types C and D can be found in Figs. 3.14 and 3.15. For frequently used hip roof pitches (3/12 - 6/12), the variation of roof pitch influences roof sheathing fragilities

moderately. The probability of no roof sheathing failure for Type D with 5/12 roof pitch is 8% higher than those for 3/12 roof pitch for a wind speed of 71 m/s (158 mph). As shown in Fig. 3.15, for Types C and D, the median wind speeds reach the maximum value for 7/12 roof pitch and drop rapidly for higher pitch angles. Generally, roof pitch shows more substantial effects on the fragilities of the complex hip-roofed building (Type D) than rectangular hip-roofed building (Type C) for roof pitches smaller 7/12.

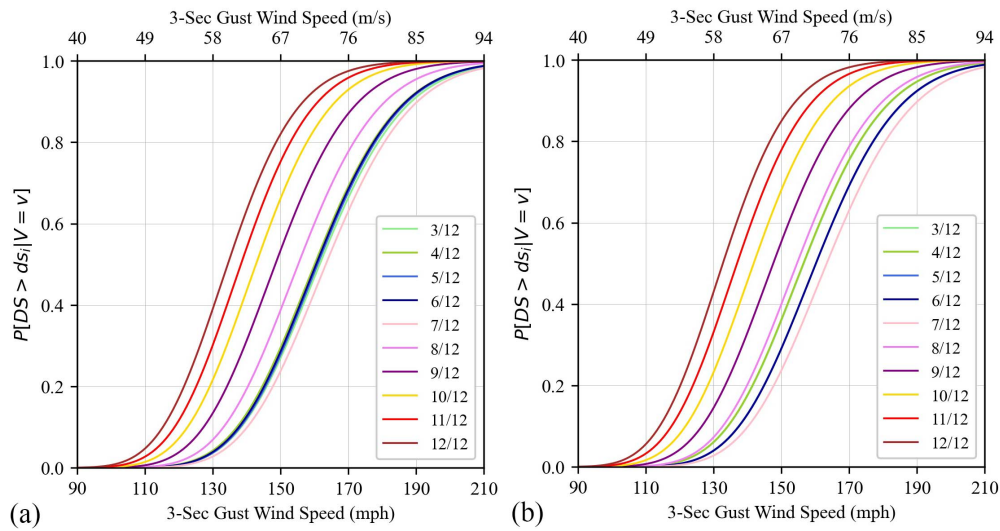


Figure 3.14: Fragility curves for hip-roof buildings with different roof pitches (DS1): (a) Structure type C; (b) Structure type D

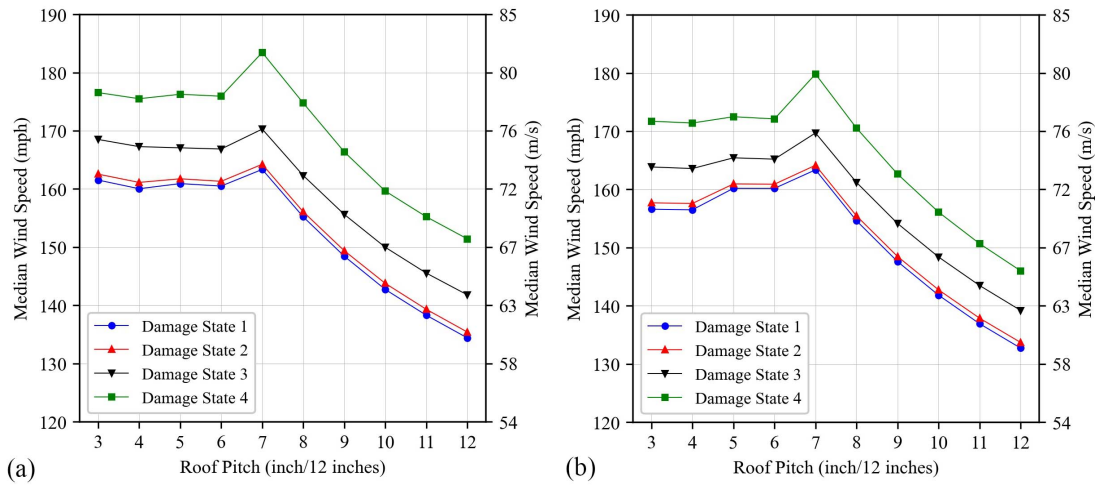


Figure 3.15: Median wind speed of fragility curves for hip-roof buildings: (a) Structure type C; (b) Structure type D

In summary, the effect of roof pitch on roof sheathing fragilities is substantial for gable roofs with a roof pitch smaller than 7/12 and hip roofs with a roof pitch larger than 6/12. For gable roofs with roof pitches smaller than 7/12, roof pitch shows a stronger effect on roof sheathing fragilities for complex roofs than those for simple roofs. For hip roofs, the effect of roof pitch on roof sheathing fragilities is similar for simple and complex roofs. Fragility parameters for building model set 2 are summarized in Appendix B for brevity.

3.4.3 Comparison with other characteristics

Fragility analysis was applied to selected building models with modified building properties to assess the importance of roof type and roof pitch relative to other critical building and structural characteristics. Fragility curves for Type 7 (L-shaped gable roof) and Type 29 (T-shaped hip roof) with different resistance types, number of stories, and overhang conditions are shown in Figs. 3.16 and 3.17. To evaluate the effect of resistance on roof sheathing fragilities, the fragility curves were developed for structures with closed-cell sprayed polyurethane foam (ccSPF) retrofitted panels (Table 3.3). Fragility curves for Type 1 (simple rectangular

gable roof) and Type 24 (rectangular hip roof) are used to demonstrate the effect of roof configurations. Figure 3.16 suggests the effects of roof shape and roof pitch are as critical as the uplift capacity for gable roofs. The impact of roof overhang and the number of stories on roof sheathing fragilities is moderate compared to other characteristics. For hip roofs, the roof shape and roof pitch show minor effects on the fragilities compared to other properties, as shown in Fig. 3.17.

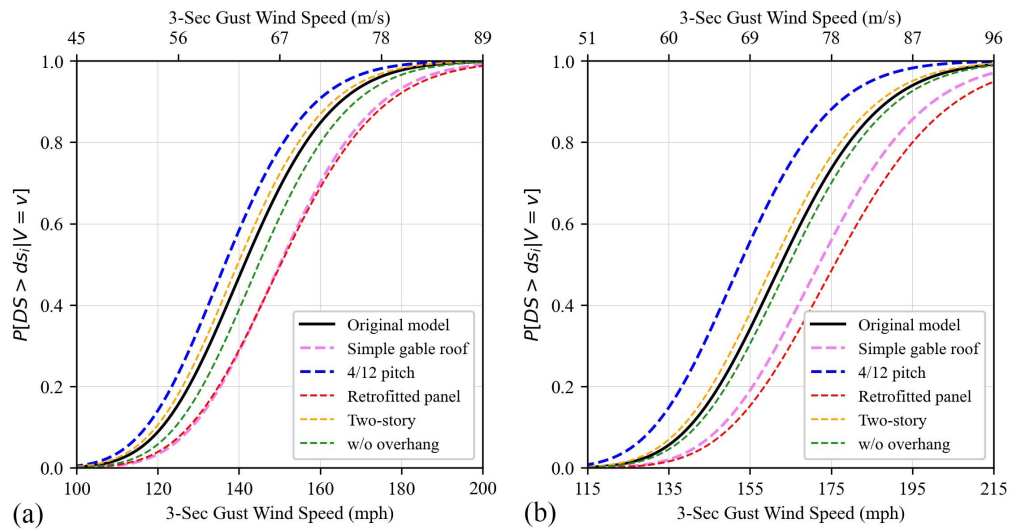


Figure 3.16: Fragility curves for Type 7 with different building features: (a) DS1; (b) DS4

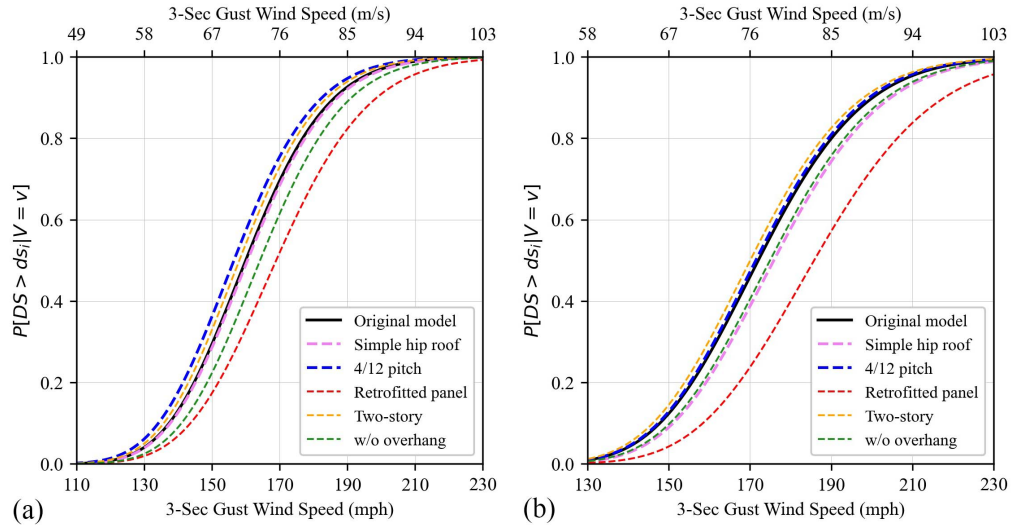


Figure 3.17: Fragility curves for Type 29 with different building features: (a) DS1; (b) DS4

3.5 Roof Modeling Methodology

The fragility analysis presented in Section 3.4 suggests that roof shape has a more significant effect on roof sheathing fragility for gable roofs than for hip roofs. Specifically, gable roofs with more complex configurations experience higher probabilities of roof sheathing failure. Conversely, wind fragilities for non-rectangular hip roofs show minimal differences for different roof shapes. Among all building models, despite variations in roof shapes, gable-roofed buildings show higher fragilities than hip-roofed buildings. The roof covering can be modeled following the same methodology as the roof sheathing (Gurley et al., 2005). Therefore, the conclusions drawn for the effects of roof shape and roof pitch on roof sheathing fragility can be extended to roof covering.

As a result, five baseline roof types, comprising buildings with rectangular and non-rectangular footprints, are defined to develop the archetype roof configurations for wind vulnerability modeling. Table 3.4 provides detailed descriptions of these roof types. Two roof types - simple hip and cross-hip - are defined for hip roofs with rectangular or non-

rectangular building footprints. Based on the ANOVA test results (Section 3.4.1.4), three roof types are created to represent gable roofs, distinguished by the number of ridgelines. Roofs classified as the same type, when other building characteristics are the same, should have similar wind performance and can be modelled using the same roof layout.

Furthermore, five roof archetypes (Fig. 3.18) were developed for modeling the proposed roof types (Table 3.4). The roof plan for each roof archetype is designed considering the ease of modeling and its popularity among single-family dwellings. Compared to building archetypes with only simple gable and hip roofs used by existing wind loss models, the five roof types proposed in this study provide a more realistic description of the single-family building stock, hence leading to more accurate prediction of building damages and losses under wind hazards. Since non-rectangular roofs are proven to be more vulnerable than rectangular roofs, the inclusion of non-rectangular building archetypes in wind vulnerability modeling will result in higher estimation of wind losses.

Table 3.4: Proposed roof types for single-family houses

Roof type	Notation	Description
Simple gable	g	Gable roof with one ridgeline
Simple cross-gable	scg	Gable roof with two or three ridgelines
Complex cross-gable	ccg	Gable roof with more than three ridgelines
Simple hip	h	Rectangular hip roof
Cross-hip	ch	Non-rectangular hip roof

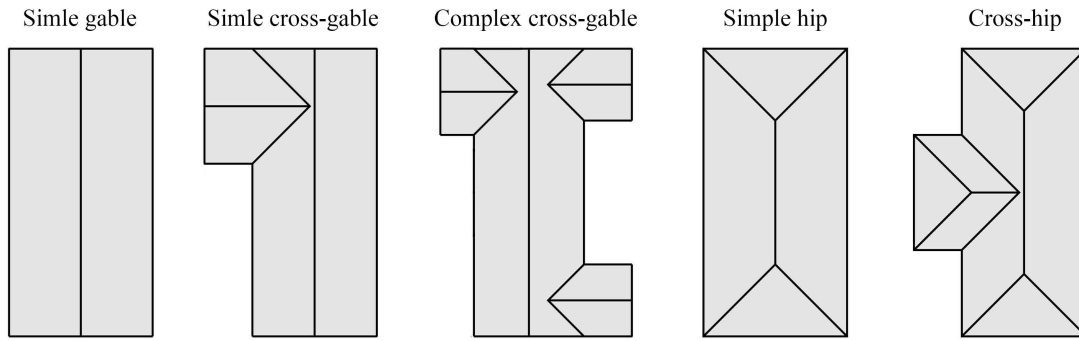


Figure 3.18: Archetype roof plans for different roof types

Results from building models with different roof pitches show that the roof pitch influences roof sheathing fragility considerably, and the effect differs between gable and hip roofs. In the case of gable roofs with roof pitches below $7/12$, the failure probability of roof sheathing decreases rapidly as the roof pitch increases. On the other hand, the effect of roof pitch on roof sheathing fragility for hip roofs with pitches smaller than $7/12$ is moderate. When the roof pitch exceeds $6/12$, the fragility of gable roofs changes moderately with different roof pitches, while the failure probability of roof sheathing in hip roofs increases drastically when the roof pitch rises. Therefore, it is reasonable to neglect the roof pitch variation for intermediate-sloped ($3/12 - 6/12$) hip roofs and steep-sloped (greater than $6/12$) gable roofs for the wind vulnerability assessment of roof sheathing. Moreover, since hip roofs with a roof pitch greater than $6/12$ are rare in practice, the effect of roof pitch on roof sheathing fragility for hip roofs is moderate.

In conclusion, differentiation between intermediate-sloped ($3/12 - 6/12$) and steep-sloped (larger than $6/12$) roofs is critical for the accuracy of wind damage and loss assessment. Using building archetypes with only intermediate-sloped roofs can result in an overestimation of the failure probability of roof components. Additionally, when modeling gable roofs, more detailed roof pitch configurations (e.g., smaller and larger than 20°) should be considered.

3.6 Limitations

This study aims to provide an evaluation of the effects of roof shape and roof pitch on roof sheathing fragility using the analysis methods adopted by current wind vulnerability models, including the FEMA HAZUS-MH model (Vickery, 2006) and the FPHLM model (Hamid et al., 2011), and previous research on fragility analysis for non-rectangular buildings (Amini and van de Lindt, 2014; Masoomi et al., 2018). Due to the lack of data on wind pressures on complex roofs, key assumptions were made when conducting the fragility analysis for roof sheathing.

First, the wind pressures applied on roof sheathing were calculated using the code-based method. Wind pressures were determined based on the maximum wind pressure considering all possible wind directions instead of a specific wind direction since the wind pressure data for directional cases is unavailable for non-rectangular buildings. As shown in Eqs. 3.3 and 3.4, a wind directionality factor (K_d) is applied to account for the reduced probabilities of maximum winds coming from any given direction and the maximum pressure coefficient occurring for any given wind direction (ASCE, 2016). As discussed by Lee and Rosowsky (2005), the wind directionality factor is conservative, and the actual wind pressures should be lower than those used in this study.

Second, the change in internal wind pressure due to the damage of openings (e.g., windows, doors) is not considered in the fragility analysis. If the increase of internal wind pressure due to the damage of openings were considered, the failure probabilities for roof sheathing would be higher than those shown in Section 3.4.

Last, the external wind pressure coefficients (GC_p) provided in ASCE 7-16 (ASCE, 2016) are determined based on the roof pitch. For ease of use, the roof pitches are classified into three groups ($7^\circ - 20^\circ$, $20^\circ - 27^\circ$, and $27^\circ - 45^\circ$), and the GC_p values for roof pitches within the same group are assumed to be the same, except for hip roofs with roof pitches larger than 27° . As a result, the fragility curves Figs. 3.12 and 3.14 may have a larger variance for

roof pitches within the same group and a smaller variance between different groups when using more accurate wind pressure data.

3.7 Summary

The effects of critical building characteristics, including roof shape and roof pitch, on roof sheathing fragility are evaluated in this chapter. The fragility analysis was conducted on building models with rectangular and non-rectangular footprints. The comparison between fragility curves indicates that roof shape has a more significant effect on roof sheathing fragility for gable roofs than for hip roofs. For gable roofs with more complex configurations, roof sheathing experiences higher failure probabilities and shows a larger variance in fragilities. In contrast, wind fragilities for hip roofs show minimal differences for different roof shapes. Among all building models, despite variations in roof shapes, gable-roofed buildings exhibit higher fragilities than hip-roofed buildings. For both gable and hip roofs, a larger variance in roof sheathing fragility is observed for more severe damage states.

Results for building models with different roof pitches show that roof pitch also influences roof sheathing fragility considerably. For roof pitches smaller than 7:12, the failure probabilities of roof sheathing panels in gable roofs decrease rapidly with the increase of roof pitch. For hip roofs, roof pitch has a moderate effect on roof sheathing fragility when the roof pitch is smaller than 7:12. When the roof pitch exceeds 6:12, the failure probability of roof sheathing in hip roofs increases drastically when the roof pitch rises.

Based on the fragility results, the inclusion of complex roof geometries in wind damage calculation is important to avoid underestimation of building damages. Consequently, five roof archetypes were designed to model single-family houses with different shapes. On the other hand, it is suggested that the variation of roof pitch should be considered when modeling gable roofs since roof sheathing fragilities show a substantial difference between frequently used roof pitches. Following the suggestions on roof modeling drawn from the

sensitivity analysis, Chapter 4 presents the development of a building inventory generation model, including the creation of building-level roof type and roof pitch data. Chapter 5 describes the site-specific building modeling method based on the roof archetypes.

CHAPTER 4

BUILDING INVENTORY GENERATION MODEL

This chapter presents a building inventory generation model as part of the regional wind risk assessment framework. The proposed model aims to collect building metadata for single-family houses by integrating remote sensing and real estate data with computer vision techniques and statistical models. The development of this model has three main purposes: (1) evaluate the efficiency and generalizability of machine learning in building inventory generation; (2) produce large-scale building inventories to improve the understanding of single-family residential building stock; (3) generate building inventory inputs for the wind damage and loss model in Chapter 5.

Section 4.1 provides an overview of the model, including data sources and the data generation pipeline. Section 4.2 describes a baseline building inventory that provides a general understanding of the typical configurations and distribution of critical building attributes. Section 4.3 explains in detail the development of each data collection module. Finally, in Section 4.4, case studies for generating city-level roof-type data and neighborhood-level building inventories are presented.

4.1 Overview

The building inventory generation model aims to produce accurate and low-cost building metadata using machine learning-based methods (e.g., semantic segmentation, classification, and regression). Among the building characteristics that are critical for the building's wind

vulnerability, those selected to be predicted using machine learning satisfy at least one of the following criteria:

- The building characteristic is not available in existing databases, but is distinguishable in building images or highly correlated with other available building features.
- The building feature data predicted using machine learning are more accurate than existing data.

The structure of the proposed model is illustrated in Fig. 4.1, which consists of four data collection modules for roof plan dimensions, roof type, number of stories, and roof pitch. This model relies on Google Maps and Zillow’s Transaction and Assessment Database (ZTRAX) (Zillow, 2018) as its primary data sources. Google Maps provides low-cost and regularly updated satellite images and street view images at the building level. ZTRAX is the largest real estate database in the United States. It contains geographic information, property characteristics, and prior valuations for 150 million parcels, covering most single-family dwellings in the United States. However, certain critical building characteristics required for the wind risk assessment, such as roof type and roof pitch, are not available in the ZTRAX database. This limitation motivates the development of the inventory generation model. The construction of the building inventory for the region of interest starts with acquiring basic building information (e.g., building address, construction year, and building value) from the ZTRAX database. Next, satellite and street view images are downloaded based on the building address via Google Maps APIs. A semantic segmentation model is then applied to satellite images to extract roof outlines, which are used to measure roof dimensions and produce refined satellite images. The roof type and number of stories are predicted by CNNs based on the satellite and street view images. Finally, a regression model is used to predict the roof pitch based on other building characteristics. Details of each data collection module are described in Section 4.3.

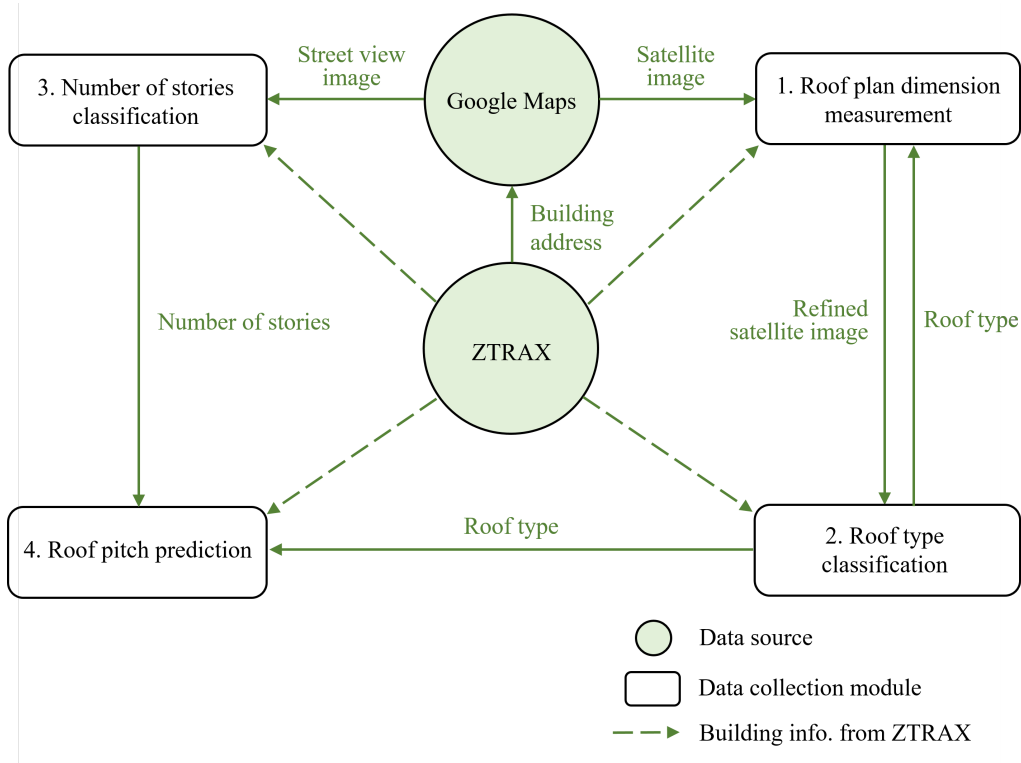


Figure 4.1: Structure of the building inventory generation model

To evaluate the performance of the inventory generation model for the study area, a series of testing datasets were constructed based on houses in New Hanover County for different data extraction tasks. To ensure a robust evaluation, buildings in New Hanover County were excluded from the training datasets for roof segmentation, roof classification, and number of stories classification. A different strategy is applied to the roof pitch prediction, which is implemented with a regression model. Considering that the correlation between roof pitch and other building features (e.g., year built and building value) may be location-sensitive, both the training data and testing data were constructed using buildings in New Hanover county.

4.2 Baseline Building Inventory

A baseline building inventory, which includes 1,314 randomly selected single-family houses in New Hanover County, was created to provide a general description of the single-family residential building stock in the study area. The building attributes for the baseline inventory were gathered from the ZTRAX database and building images (i.e., satellite and street view images). Categorical and numerical building features in the baseline inventory are summarized in Tables 4.1 and 4.2, respectively. The baseline building inventory serves three main purposes in this study. First, it provides the typical configurations of critical building characteristics and guides the selection of corresponding data generation methodology. Second, the statistical distribution of building features derived from the baseline inventory facilitates the validation and correction process of the prediction results. Finally, the baseline inventory is used as the training data for predicting the roof pitch.

Table 4.1: Categorical building attributes in the baseline building inventory

Parameter	Category	Source
Roof type	Simple gable, simple cross-gable, complex cross-gable, simple hip, cross-hip, mix	Satellite images
Exterior wall material	Asbestos shingle, brick, brick veneer, rock, siding, wood, wood shingle	ZTRAX
Topography	Level grade, above street level, rolling	ZTRAX

Table 4.2: Numerical building attributes in the baseline building inventory

Parameter	Unit	Source
Building area	sqft	ZTRAX
First floor area	sqft	ZTRAX
Roof area	sqft	Satellite images
Bounding box area	sqft	Satellite images
Roof length	ft	Satellite images
Roof width	ft	Satellite images
Roof pitch	degree	Satellite and street view images
Garage area	sqft	ZTRAX
Building value	dollar	ZTRAX
Year built		ZTRAX
Number of stories		ZTRAX and street view images

The critical building characteristics that are not available in the ZTRAX database were extracted from building images through manual inspection. These building characteristics include roof plan dimensions, roof type, and roof pitch. As shown in Fig. 4.2, roof plan dimensions were measured from satellite images. The roof area (A_r) represents the area of the roof polygon, while the roof length (L) and width (B) are defined as the length and width of the entire roof structure, determined by fitting the smallest rectangle enclosing the roof outline. Additionally, the area of the fitted rectangle is referred as the bounding box area (A_b).

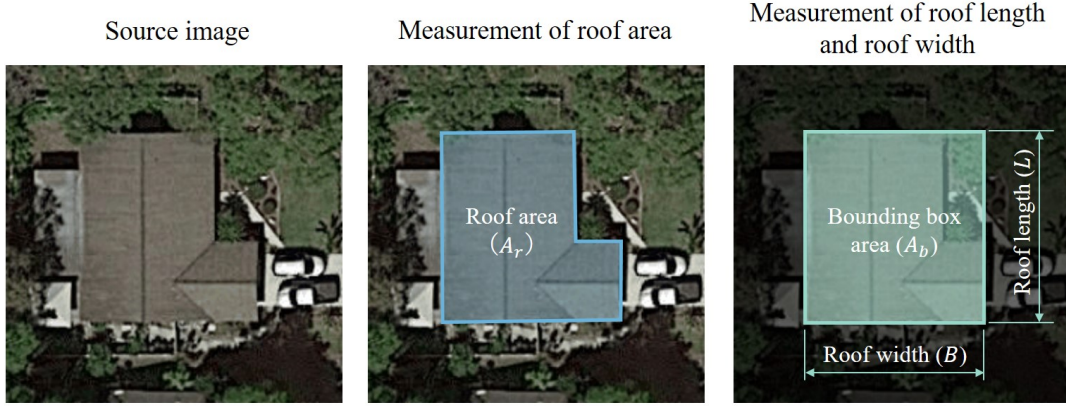


Figure 4.2: Measurement of roof dimensions using a building-level satellite image

The roof dimensions are calculated based on the ground resolution (q_{gr}) of satellite images using the following equations (Microsoft, 2022):

$$q_{gr} = 513592.67 \times \frac{\cos(\text{latitude} \times \frac{\pi}{180})}{2^{\text{zoom level}}} (\text{ft/pixel}) \quad (4.1a)$$

$$A_r = q_{gr}^2 A_{rp} \quad (4.1b)$$

$$L = q_{gr} L_p \quad (4.1c)$$

$$B = q_{gr} B_p \quad (4.1d)$$

where *latitude* is the latitude of the centroid of the building; *zoom level* represents the zoom level used for downloading the satellite images, which is set to be 20 for single-family dwellings; A_{rp} , L_p , and B_p are the roof area, length, and width measured in pixels from the satellite image. The measurement method for roof dimensions was validated using building footprint data provided by Los Angeles Region Imagery Acquisition Consortium (LARIAC) Program ¹. Roof areas for 40 single-family houses calculated using Eqs. 4.1a and 4.1b were compared with the building footprint areas in the LARIAC dataset. As shown in Fig. 4.3, the measured roof area shows good agreement with the building footprint area recorded in

¹<https://lariac-lacounty.hub.arcgis.com/>

the LARIAC dataset. The roof plan dimensions were measured for each building in the baseline inventory. Figure 4.4 shows the distribution of roof area for the baseline inventory, which ranges from 585 to 5,021 sqft. Approximately 90% of houses have a roof area between 1,000 and 3,000 sqft.

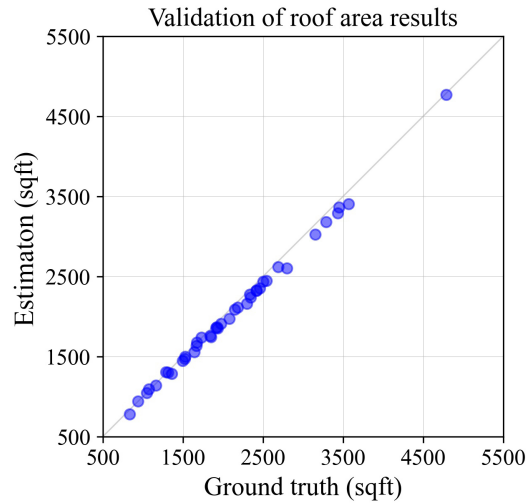


Figure 4.3: Validation of the roof dimension measurement process

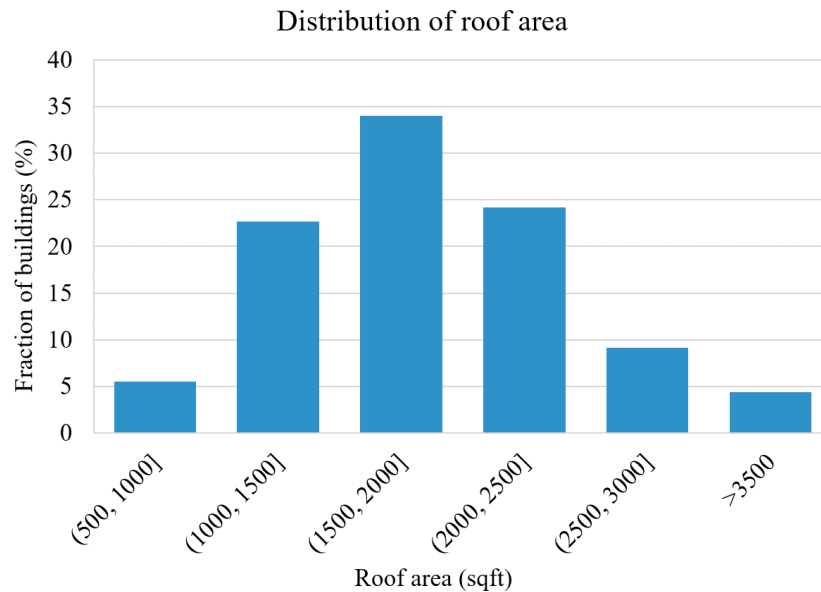


Figure 4.4: Distribution of roof area for houses in the baseline inventory

The roof type of each building is also classified using satellite images according to the roof types defined in Table 3.4. The distribution of roof types is presented in Fig. 4.5. The ratio of gable roofs to hip roofs is approximately 4:1, and houses with mix-shaped roofs, which are roofs with a combination of gable and hip roof sections, account for 8% of the buildings in the baseline dataset. All mix-shaped roofs have complex roof configurations, except for one building that has a simple roof with a rectangular outline. In addition, flat roofs are not observed in the baseline inventory.

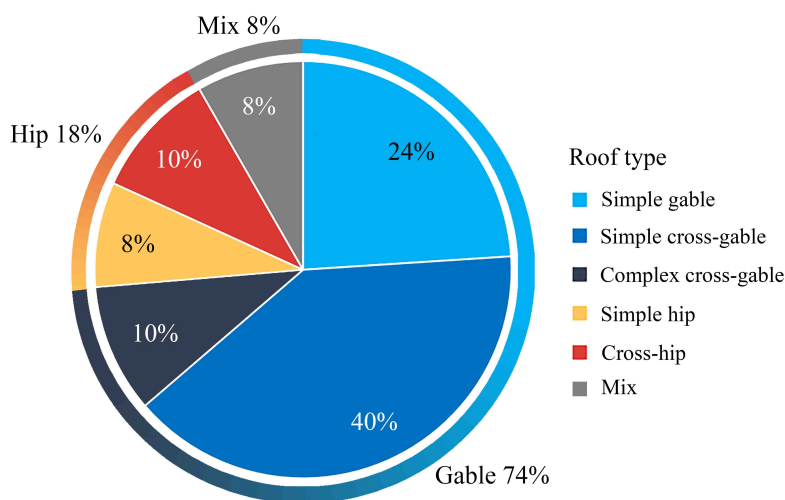


Figure 4.5: Distribution of roof types for houses in the baseline inventory

Another critical roof feature, roof pitch, is measured using two methods depending on the building's orientation in the street view image. If the street view image shows the gable end wall, as depicted in Fig. 4.6 (a), the roof pitch can be directly measured. However, if the house has a hip roof or the gable end wall is not visible, the roof height is measured in the street view image, as presented by Fig. 4.6 (b), and then adjusted based on the perspective effect. Finally, the roof pitch is calculated by the following equation:

$$\theta = \arctan\left(\frac{2h_s}{B_s}\right) \quad (4.2)$$

where h_s = adjusted roof height considering the perspective effect; B_s = width of the

corresponding roof segment. One single roof pitch value is recorded for each building. If the building has roof segments with different roof pitches, the pitch angle for the main roof segment is used. The measured roof pitch in degree or radian is converted to the closest standard roof pitch in the number of inches the roof rises for every 12 inches in depth.

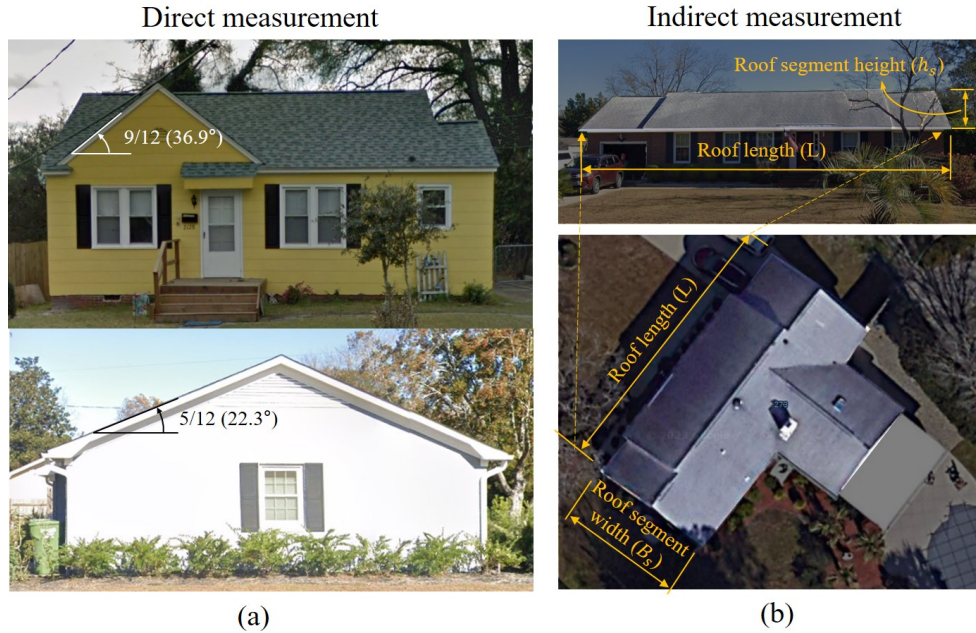


Figure 4.6: Measurement of roof pitch: (a) Direct measurement for buildings with gable end wall visible in street view images; (b) Indirect measurement based on roof height and plan dimensions

Figure 4.7 shows the distribution of roof pitch for the baseline inventory. The roof pitch varies between 2/12 (9°) and 16/12 (53°). The fraction of houses with roof pitch below 20° , between 20° and 27° , and above 27° is 29%, 44%, and 27%, respectively. The most common roof pitch values are 4/12 (18°) and 5/12 (23°), accounting for up to 58% of the houses investigated. Roof pitches of 4/12 and 5/12 are also used for the building archetypes in HAZUS-MH (Vickery, 2006) and FPHLM (Gurley et al., 2005), respectively. However, around 40% of houses have roof pitches steeper than 5/12, which can result in distinctive performance of roofs during hurricanes.

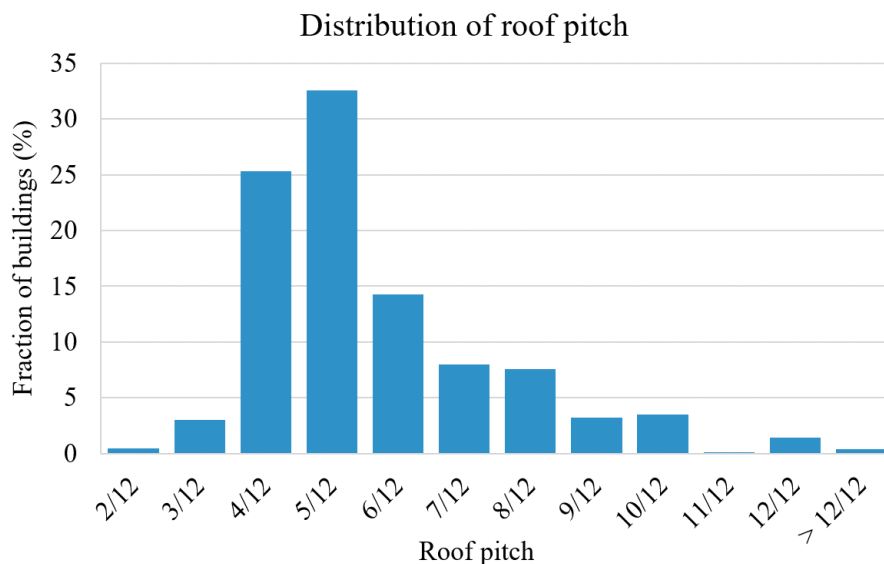


Figure 4.7: Distribution of roof pitch for houses in the baseline inventory

4.3 Building Data Collection Methods

This section describes the development of building data collection modules that constitute the inventory generation model. Sections 4.3.1 - 4.3.4 introduce the data collection methods for roof plan dimension, roof type, number of stories, and roof pitch. The core of each method is a machine learning model, augmented by pre-processing and post-processing steps to generate the input data and refine the results.

4.3.1 Roof plan dimension measurement

4.3.1.1 Workflow overview

Roof plan dimensions, including roof area (A_r), bounding box area (A_b), roof length (L), and roof width (B), are measured based on roof outlines extracted from building-level satellite images. Publicly available building footprint datasets (e.g., OpenStreetMap (Haklay

and Weber, 2008) and FEMA USA Structures²) applied strong regularization algorithms to the building footprint polygons, which reduced the accuracy of building dimensions measured based on those building outlines. Moreover, building footprints in the aforementioned datasets are limited in availability for single-family dwellings. On the other hand, building area data provided by real estate datasets (e.g., ZTRAX database (Zillow, 2018)) are based on the living area, which can differ substantially from the roof area. Nevertheless, this data can still be used as the reference value to check the validity of roof dimensions measured from images.

To generate more accurate roof dimension data, a roof segmentation model is created to extract roof outlines from building-level satellite images. The workflow for the proposed dimension measurement process is depicted in Fig. 4.8. First, the building geolocation (i.e., longitude and latitude of the centroid of the building) is acquired based on the building address using Google Geocoding API ³. Using Google Maps Static API ⁴ with the zoom level set to be 20, the building-level satellite image is downloaded and fed into a roof segmentation model to extract the roof outline. The roof plan dimensions are then calculated based on the roof outline. Finally, the roof dimensions are cross-checked against real estate building area data and approximations are made to erroneous roof dimensions. In addition, the refined satellite image is generated by cropping the images using the roof outline, serving as the input for the roof type classification.

²<https://gis-fema.hub.arcgis.com/pages/usa-structures>

³<https://developers.google.com/maps/documentation/geocoding>

⁴<https://developers.google.com/maps/documentation/maps-static>

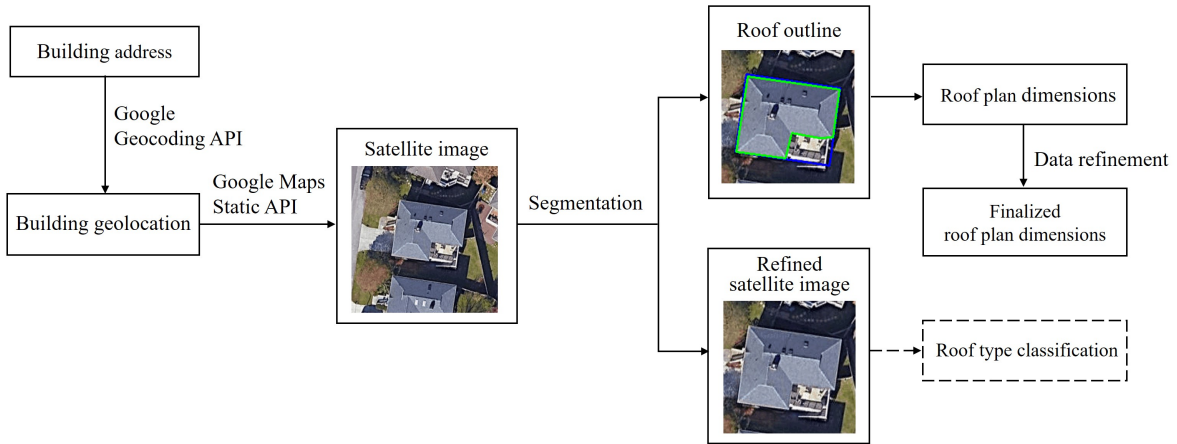


Figure 4.8: Workflow for roof plan dimension measurement process

4.3.1.2 Roof segmentation

A benchmark dataset consisting of 1,396 building-level satellite images for single-family houses was constructed to train the roof segmentation model. The images were manually annotated to create the roof segmentation masks. The dataset was split into 1,117 images for training and 279 images for validation. Data augmentation techniques, including rotation, mirror, and adjustment of brightness and exposure, were applied to the training images to expand the dataset and avoid overfitting. U-Net (Ronneberger et al., 2015), a Convolutional Neural Network (CNN) initially developed for biomedical image segmentation, was selected for the roof segmentation task. The architecture of the U-Net model is presented in Fig. 4.9. It works efficiently with small training datasets and has been widely used for automatic building detection and segmentation tasks on satellite and aerial imagery (Ji et al., 2019; Abdollahi et al., 2022; Wu et al., 2018). The model was trained for 400 epochs using Adam Optimizer with the learning rate = 0.0001, and the model with the lowest validation loss was selected. The Dice and Jaccard indices of the segmentation model evaluated on the

validation images are 0.963 and 0.932, which are calculated by:

$$Dice(A_p, A_{gt}) = \frac{2\|A_p \cap A_{gt}\|}{\|A_p\| + \|A_{gt}\|} \quad (4.3a)$$

$$Jaccard(A_p, A_{gt}) = \frac{\|A_p \cap A_{gt}\|}{\|A_p \cup A_{gt}\|} \quad (4.3b)$$

where A_p = predicted segmentation masks; A_{gt} = ground truth segmentation masks.

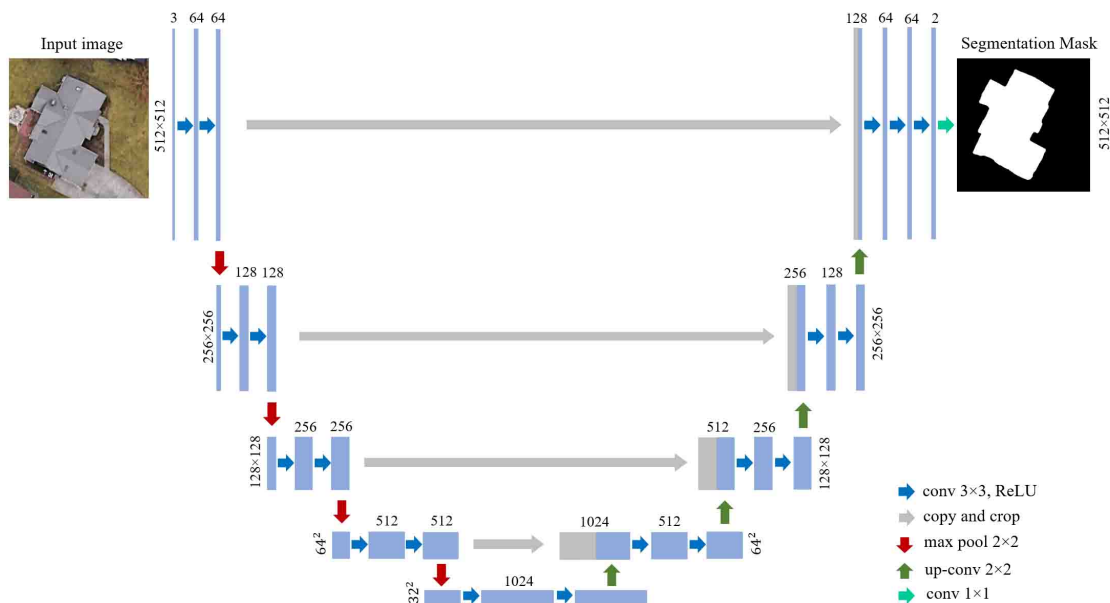


Figure 4.9: Illustration of the U-Net architecture

A testing dataset consisting of 277 building-level satellite images was created to evaluate the performance of the roof segmentation model. The Dice and Jaccard indices of the segmentation model evaluated on the test images are 0.847 and 0.739, respectively. For the purpose of this study, only the segmentation result for the target building (i.e., the building in the center of the image) is required, and the segmentation of neighboring buildings does not affect the measurement of dimensions for the target building. Therefore, the segmentation results were also assessed for solely the target building, and the resulting Dice and Jaccard indices are 0.881 and 0.791, respectively. Figure 4.10 compares the area of ground truth and predicted roof masks for testing images. The results indicate that the roof masks predicted

by the U-Net model can offer an accurate estimation of the roof area. For some buildings, the predicted roof masks underestimate the roof area, partially due to obstruction from trees.

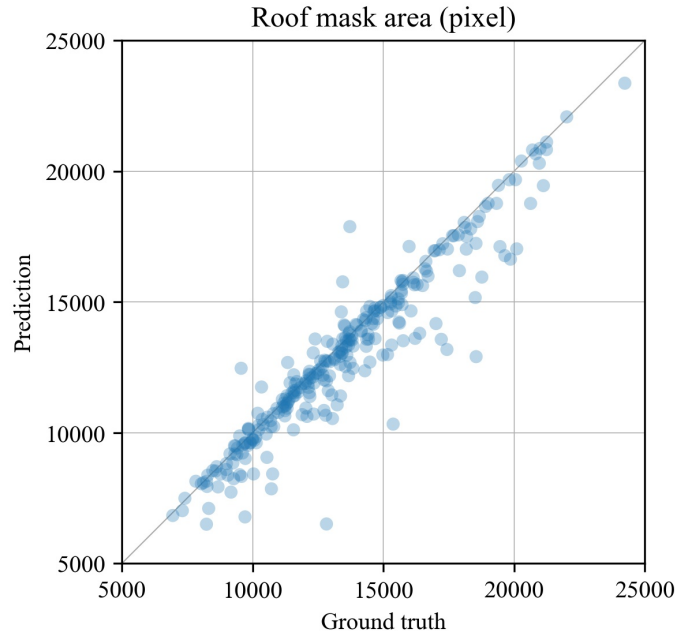


Figure 4.10: Roof mask area for the testing dataset

Following the roof segmentation, a series of post-processing steps (e.g., removal of noises and regularization of the roof polygons) are applied to the segmentation masks to produce the roof outlines. A bounding box is then fitted to the roof polygon for measuring roof length and width. The representative roof segmentation and outline extraction results are shown in Fig. 4.11. The roof outlines and boxing boxes are shown in green and blue lines, respectively. As depicted in Fig. 4.11 (e) and (f), the segmentation quality of the neighboring buildings does not affect the outline extraction for the target buildings.

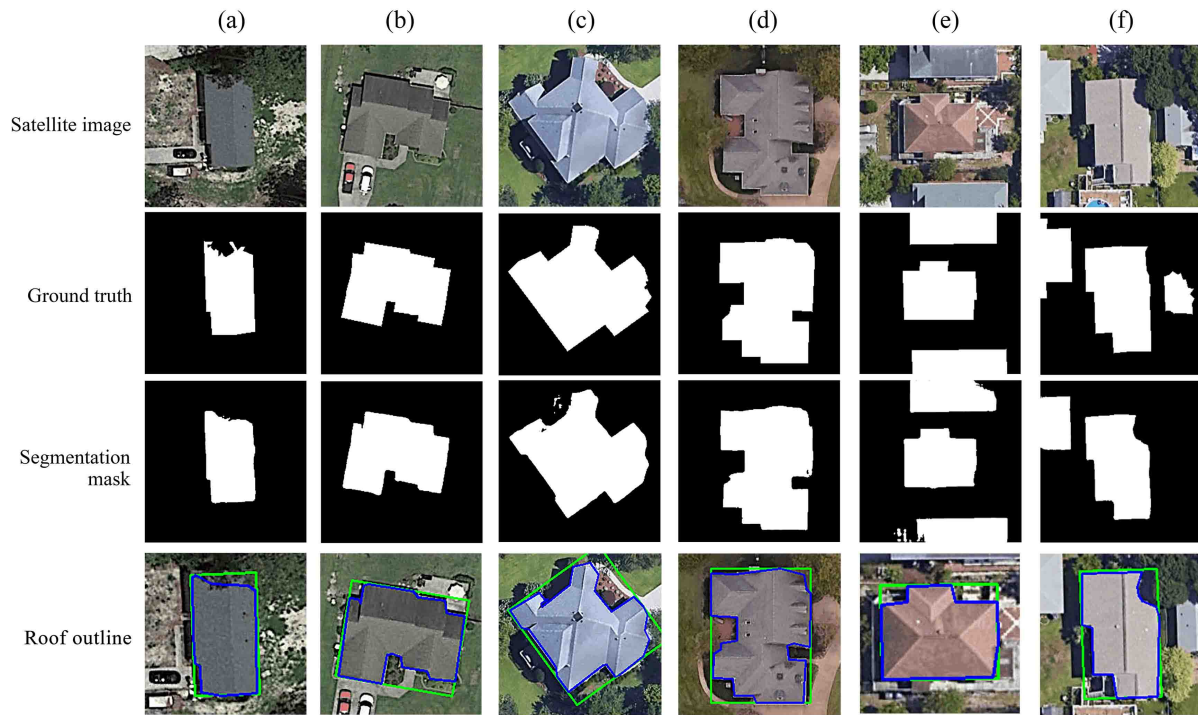


Figure 4.11: Representative roof segmentation and outline extraction results on the testing dataset

Figure 4.12 compares the building footprints obtained from our model and publicly available building footprint datasets for single-family houses in New Hanover County. As shown in Fig. 4.12, the roof segmentation model developed in this study produce more accurate roof outlines than existing datasets, especially for buildings with complex roof configurations. The refined roof outlines capture the details of roof structures and provide better estimation of the roof geometry.

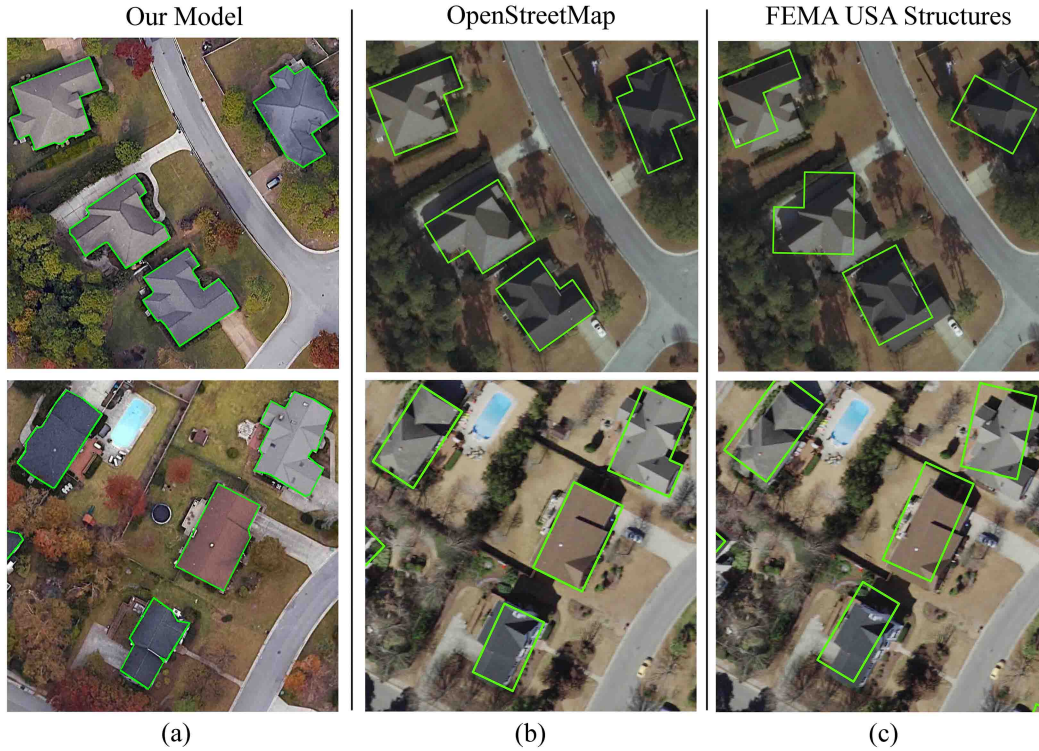


Figure 4.12: Comparison of building footprints: (a) The model developed in this study; (b) Microsoft OpenStreetMap; (c) FEMA USA Structures

4.3.1.3 Dimension refinement

Once the roof outline is identified, roof plan dimensions are measured in pixels and scaled following Eq. 4.1. However, low-quality satellite images caused by tree blockage (Fig. 4.13) can potentially reduce the accuracy of roof segmentation, resulting in erroneous roof dimensions. The usefulness of the low-quality images varies under different severity of tree occlusions. Heavily blocked rooftop images (Fig. 4.13 (c)) lead to inaccurate roof outlines and bounding boxes, while the images of slightly blocked roofs (Figs. 4.13 (a) and (b)) may still produce correct bounding box. Moreover, for rectangular-shaped buildings, the roof area may be correctly derived from the bounding box (Fig. 4.13 (a)) even if the roof outline is not accurate. Therefore, to take the best use of the segmentation results, the validities of the roof outline

and the bounding box are checked separately and different dimension refinement processes are applied to buildings with different roof types.

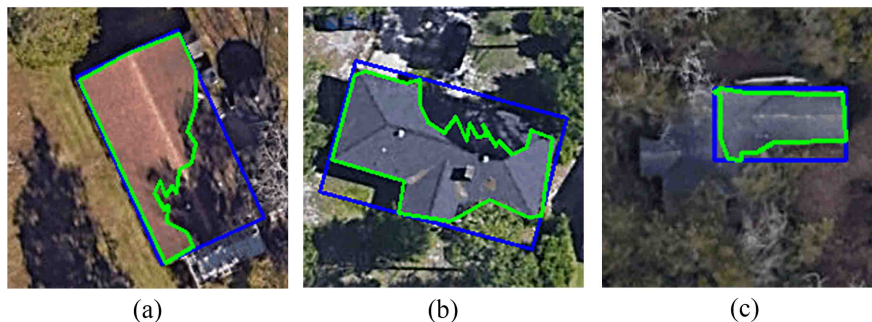


Figure 4.13: Incorrect roof outlines due to tree occlusion: (a) Slightly blocked rectangular roof with incorrect roof outline and correct bounding box; (b) Slightly blocked non-rectangular roof with incorrect roof outline and correct bounding box; (c) Heavily blocked roof with incorrect roof outline and bounding box

To ensure the validity of the roof dimensions obtained from images, the roof area (A_r) and bounding box area (A_b) are checked and refined using the building area data provided by the ZTRAX database. Different dimension refinement processes are applied to simple roofs (i.e., simple gable and simple hip) and complex roofs (i.e., simple cross-gable, complex cross-gable, and cross-hip), as described in Fig. 4.14. The roof-to-floor ratio (R_{rf}), box-to-floor ratio (R_{bf}), and aspect ratio (R_a) are calculated using the following equations:

$$R_{rf} = \frac{A_r}{A_f + A_g} \quad (4.4a)$$

$$R_{bf} = \frac{A_b}{A_f + A_g} \quad (4.4b)$$

$$R_a = \frac{L}{B} \quad (4.4c)$$

where A_f = first floor area; A_g = garage area. The incorrect roof dimensions are updated using the following equations:

For simple roofs,

$$A_r = R_{bf}^*(A_f + A_g) \quad (4.5a)$$

$$B = \sqrt{A_r/R_r^*} \quad (4.5b)$$

$$L = R_r^*B \quad (4.5c)$$

For complex roofs,

$$A_r = R_{rf}^*(A_f + A_g) \quad (4.6a)$$

$$A_b = R_{bf}^*(A_f + A_g) \quad (4.6b)$$

$$B = \sqrt{A_b/R_r^*} \quad (4.6c)$$

$$L = R_r^*B \quad (4.6d)$$

where R_{rf}^* = mean roof-to-wall ratio; R_{bf}^* = mean box-to-floor ratio; R_r^* = mean aspect ratio. For the case study, R_{rf}^* , R_{bf}^* , and R_r^* are calculated based on the baseline building inventory with respect to each roof type, as summarized in Table 4.3.

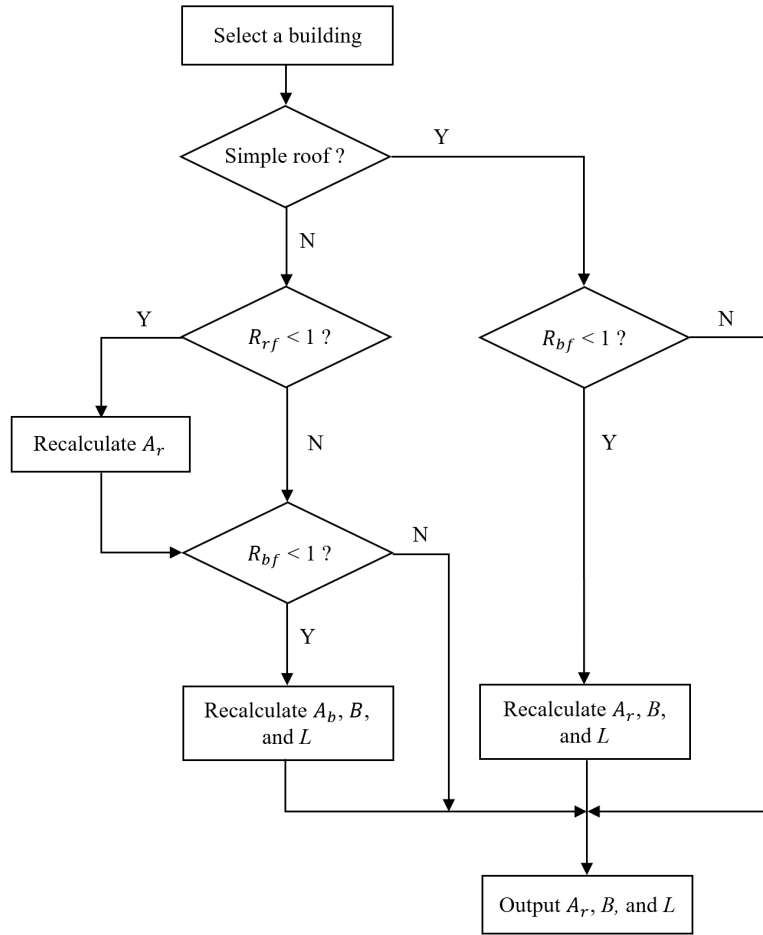


Figure 4.14: Flowchart of the roof dimension refinement process

Table 4.3: Mean roof geometry parameters calculated for the baseline building inventory

Roof type	Roof-to-floor ratio	Box-to-floor ratio	Aspect ratio
Simple gable	1.24	1.41	1.73
Simple cross-gable	1.22	1.51	1.52
Complex cross-gable	1.24	1.61	1.38
Simple hip	1.27	1.39	1.86
Cross-hip	1.26	1.60	1.59

4.3.2 Roof type classification

4.3.2.1 Roof classes

As introduced in Section 3.5, roofs for single-family dwellings are classified into five types based on their wind performance: simple gable, simple cross-gable, complex cross-gable, simple hip, and cross-hip. Among the five roof types, gable and hip roofs with different roof complexity are differentiated, providing a more detailed and realistic description of the building stock compared to the roof types used by existing models. In addition, buildings with a combination of gable and hip roof sections are classified as one of the five roof types based on visual similarity. Example building models with each type of roof are depicted in Fig. 4.15. In this study, roof types are predicted using the refined single-building-level satellite images produced by the roof segmentation process (Section 4.3.1). Following the image collection process described in Section 4.3.1.1, low-quality images that cannot provide sufficient information for rooftops may be obtained. As shown in Fig. 4.16, mainly three categories of images are considered to be low-quality: (1) unrecognizable roofs caused by tree occlusion, (2) mislocated images caused by incorrect building geolocation, and (3) demolished buildings. Among the three cases, tree occlusion is most frequently observed. To avoid erroneous roof data caused by low-quality images, an additional roof class, denoted as *unknown*, is considered in the model.

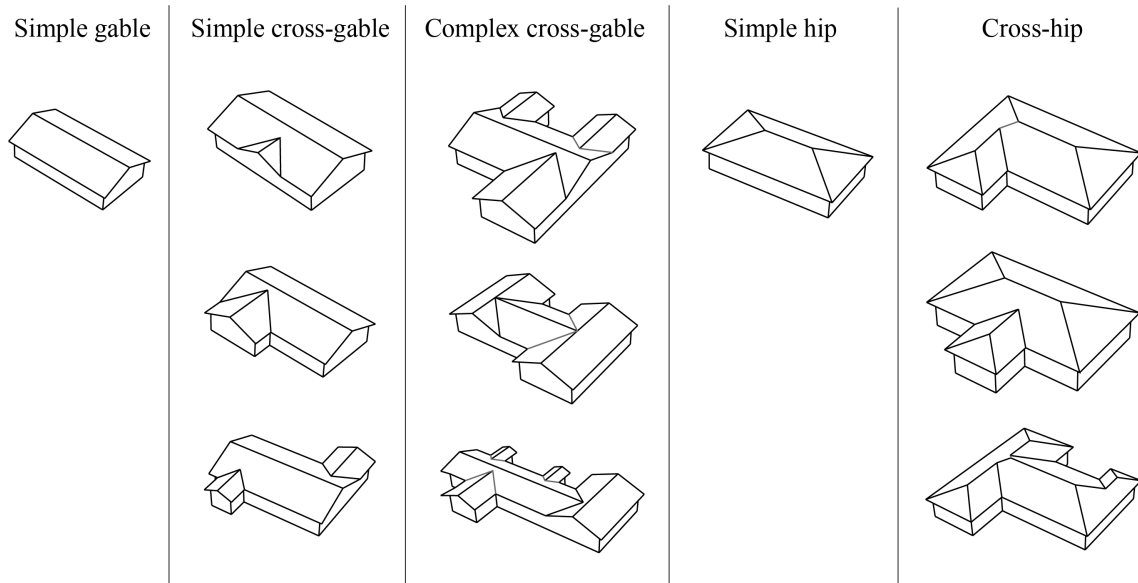


Figure 4.15: Example building models with different types of roofs

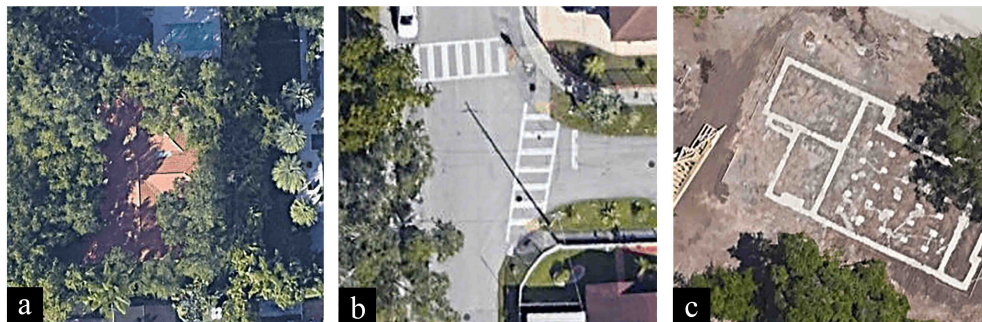


Figure 4.16: Example low-quality satellite images: (a) Rooftop is heavily blocked by trees; (b) Geolocation of the building is incorrect; (c) The building was demolished

4.3.2.2 Overall workflow

The proposed roof type classification workflow for single-family houses is shown in Fig 4.17. For a selected area, the refined satellite images obtained from the roof segmentation model are first used to predict the roof types. After the roof-type data for all buildings are generated, the neighboring buildings for buildings with missing roof types (i.e., roof types classified as

unknown) are identified. In the end, the missing roof data are populated by a data imputation algorithm using critical building attributes and neighborhood-level roof characteristics.

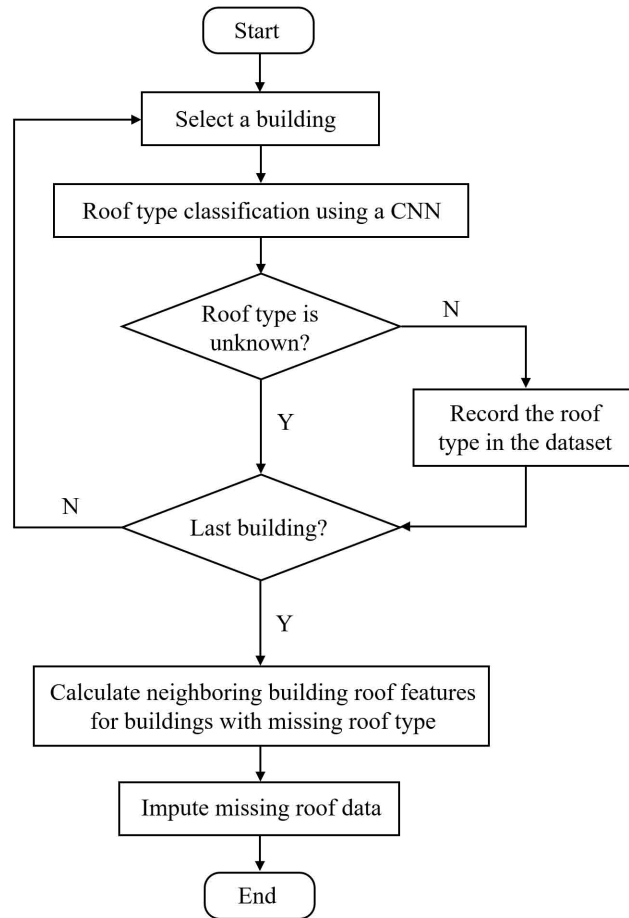


Figure 4.17: Flowchart for roof type classification

4.3.2.3 Training

A benchmark satellite image database was constructed to train the CNN model for the roof type classification. The dataset consists of 11,834 building-level satellite images collected from Google Maps for single-family houses on the eastern coast of the United States. The images were manually labeled and adjusted to ensure that each image only included one complete roof. Twenty percent of images for each category were randomly selected for

the validation dataset. The number of training and validation images for each class are summarized in Table 4.4. The representative satellite images for each roof class in the training dataset are shown in Fig. 4.18.

Table 4.4: Distribution of training and validation images for the roof classification model

Roof type	Number of images	
	Training	Validation
Simple gable	1820	455
Simple cross-gable	1805	451
Complex cross-gable	1160	290
Simple hip	1037	259
Cross-hip	1823	456
Unknown	1822	456



Figure 4.18: Examples satellite images in the training dataset for roof type classification

The generalizability (i.e., accuracy regarding unseen test data) of neural networks is considered to be related to the representativeness of the training sets (i.e., adequate samples to define the target data domain) (Schwendicke et al., 2021; Zhang et al., 2020). Fine-tuning, a branch of Transfer Learning methods, is a viable tool to improve the generalizability of neural networks on image-related tasks, specifically with limited observations. In this study, the roof classification model was obtained by fine-tuning a deep CNN architecture, VGG-19 (Simonyan and Zisserman, 2014) (Fig. 4.19), that is pre-trained on the ImageNet dataset (Russakovsky et al., 2015) with more than 10 million images. The pre-trained model has a Softmax layer of size 1000, which is associated with the 1000 image categories in the

ImageNet dataset. The VGG-19 architecture was proved to have the best performance on classification tasks on remote sensing data among the state-of-the-art CNN models, including roof classification using satellite images (Buyukdemircioglu et al., 2021) and building use type classification using street view images (Kang et al., 2018). Image augmentation techniques, including rotation, mirror, and adjustment of exposure and contrast, were applied to the training images to expand the training dataset and avoid overfitting. The images were re-scaled to the size of 224×224 pixels per the VGGNet architecture. The batch size is set to 32 images. The stochastic gradient descent (SGD) optimizer is used for the optimization process, with the learning rate and momentum selected to be 1×10^{-5} and 0.99, respectively. During training, the last fully connected layer and its Softmax layer (Fig. 4.19) are modified to have 6 dimensions regarding the 6 roof type classes. First, the new fully connected layers and the output layer are trained on the training dataset for 40 epochs, and the rest of the network is used as a fixed feature extractor. After the training of the fully connected layers is complete, all layers of the network are fine-tuned for 16 epochs. Early stopping based on the validation accuracy is applied to the training process, and the model with highest validation accuracy is selected. The overall validation accuracy of the selected model is 97%. The confusion matrix of the VGG-19 model evaluated on the validation dataset is shown in Fig. 4.20.

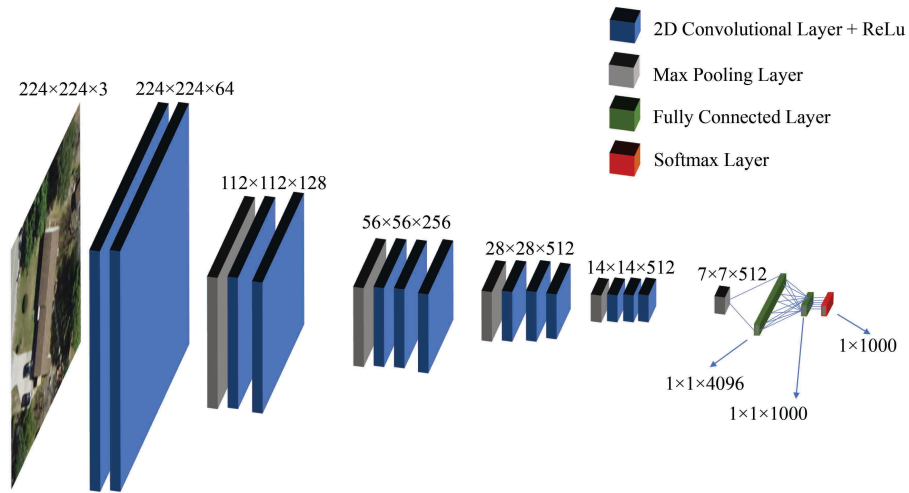


Figure 4.19: VGG-19 architecture adopted from Simonyan and Zisserman (2014)

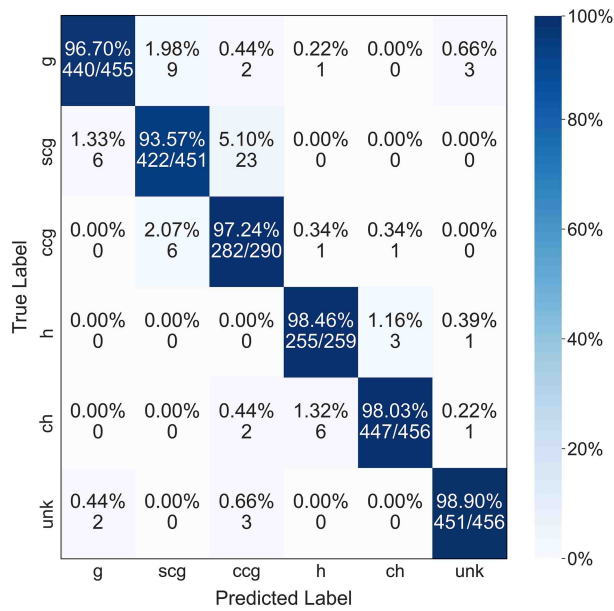


Figure 4.20: Confusion matrix of VGG-19 for roof type classification evaluated on validation dataset

4.3.2.4 Testing

Two testing datasets were constructed to evaluate the model performance on single-family houses in New Hanover County. All testing images were manually labeled. The first testing dataset—denoted as testing dataset A—consists of buildings with pure gable, pure hip, and unknown roofs. The second testing dataset—denoted as testing dataset B—is composed of buildings with mixed roof shapes (i.e., the roof has a combination of gable roof sections and hip roof sections) while the dominant roof type is still differentiable. For each testing set, the precision, recall, and F1 score were calculated for each roof class using the following equations:

$$Precision = \frac{TP}{TP + FP} \quad (4.7a)$$

$$Recall = \frac{TP}{TP + FN} \quad (4.7b)$$

$$F1\ score = \frac{2 \times Precision \times Recall}{Precision + Recall} \quad (4.7c)$$

where TP , FP , and FN are the number of *True Positive*, *False positive*, and *False Negative* prediction results. The overall Precision, Recall, and F1 score are determined using the weighted-average values among all classes.

Testing dataset A includes 500 building-level satellite images. The confusion matrix of the VGG-19 model evaluated on testing datasets A is shown in Fig. 4.21, and the scores of the model are summarized in Tables 4.5. As shown in Fig. 4.21, the model achieved high classification accuracy among all roof classes. Misclassification mainly happens between gable roofs with different complexity levels (i.e., simplex gable, simple cross-gable, and complex cross-gable) that have high inter-class variance and intra-class similarity. Moreover, the model achieved the F1 scores of 0.99 when predicting images labeled unknown, proving the capability of the model to filter out low-quality images.

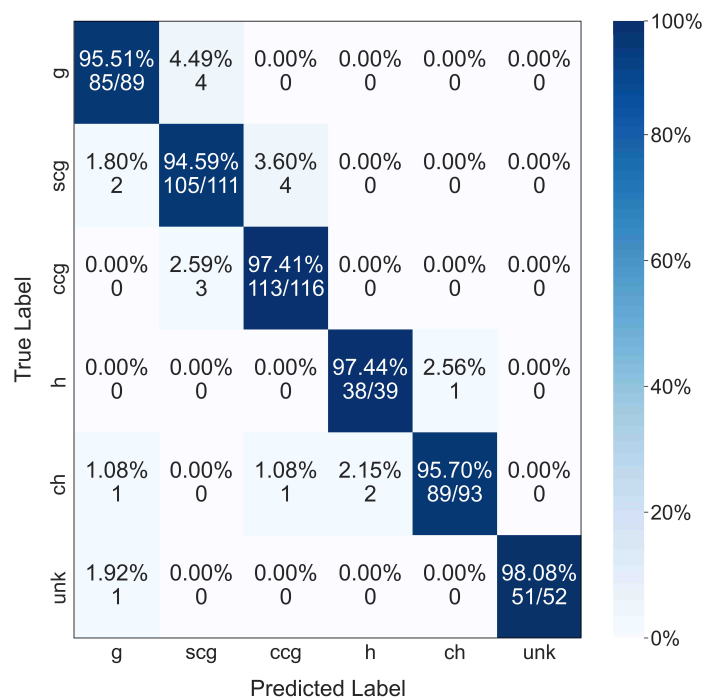


Figure 4.21: Confusion matrix of VGG-19 evaluated on test datasets A (buildings with pure gable, pure hip, and unknown-type roofs)

Table 4.5: Performance of VGG-19 on testing dataset A (buildings with pure gable, pure hip, and unknown-type roofs)

Roof type	Precision	Recall	F1 score	Support
Simple gable	0.96	0.96	0.96	89
Simple cross-gable	0.94	0.95	0.94	111
Complex cross-gable	0.96	0.97	0.97	116
Simple hip	0.95	0.97	0.96	39
Cross-hip	0.99	0.96	0.97	93
Unknown	1.00	0.98	0.99	52
Overall	0.96	0.96	0.96	500

Single-family houses with non-rectangular building shapes are often observed to have a combination of gable and hip roof shapes. However, mix-shaped roofs cannot be modeled using the existing wind risk assessment methodology. Following the roof type classification principles suggested by HAZUS-MH (Vickery, 2006), buildings with mixed roof shapes should be classified using the dominant roof type available in building archetypes. To assess the performance of the CNN model on buildings with mixed roof shapes, testing dataset B was created, which consists 150 images for mix-shaped roofs. Rectangular-shaped roofs with mixed roof shapes are rare in practice, and the dominant roof type for such roofs is hard to differentiate. Therefore, only non-rectangular houses were considered in the testing dataset. Each image was labeled with one of the complex roof classes (i.e., simple cross-gable, complex cross-gable, and cross-hip) based on the dominant roof shape. Example images for each roof class are shown in Fig. 4.22. The confusion matrix of the CNN model evaluated on the testing dataset B is depicted in Fig. 4.23, and the precision, recall, and F1 score for each class are listed in Table 4.6. As shown in Fig. 4.23, the prediction accuracy for mix-shaped roofs is lower than roofs with pure gable or hip roof styles. But the dominant roof type is still correctly identified for most mix-shaped roofs. In summary, the testing results prove the capability of the CNN model to generate reliable and reasonable roof-type data using satellite images.



Figure 4.22: Example satellite images in testing dataset B (buildings with complex and mixed roof shapes)

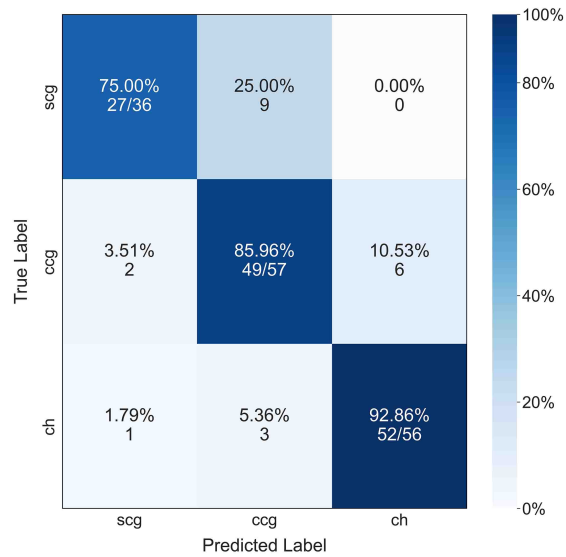


Figure 4.23: Confusion matrix of VGG-19 evaluated on testing dataset B (buildings with mixed roof shapes)

Table 4.6: Performance of VGG-19 on testing dataset B (buildings with mixed roof shapes)

Roof type	Precision	Recall	F1 score	Support
Simple cross-gable	0.90	0.75	0.82	36
Complex cross-gable	0.80	0.86	0.83	57
Cross-hip	0.90	0.91	0.90	57
Overall	0.86	0.85	0.86	150

4.3.2.5 Missing roof data population

As discussed in Section 4.3.2.1, low-quality images are identified by the CNN model, resulting in missing roof-type data in the building inventory. Roof type was found to be correlated with other building characteristics (e.g., year built and building area) (Pita et al., 2011; Hamid, 2021). To improve the completeness of the database and support more detailed analysis (e.g., neighborhood-level analysis), data imputation algorithms were developed to populate missing roof-type data. Valid roof-type data predicted by the CNN model are considered as the ground truth. Other critical building characteristics, including year built, building value, building area, and number of stories, were obtained from the ZTRAX database. Random Forest and Support Vector Machine were used for imputing missing data, which are machine learning models widely used for building-related classification tasks (Mohajeri et al., 2018; Castagno and Atkins, 2018; Taghinezhad et al., 2020; Soares et al., 2021). Based on wind tunnel tests (Shao et al., 2018; Parackal et al., 2016), roof type to be gable or hip has a more significant effect on wind pressures acting on the roof than the building shape. Therefore, different models were trained to predict roof type (gable/hip) and roof complexity (simple/complex) to simplify the classification task to binary classification and avoid cumulative errors. Figure 4.24 shows how roof features predicted by the imputation models are mapped to the roof types defined in Table 3.4. For simplification, complex cross-gable roofs are used for representing all complex gable roofs (i.e., simple cross-gable and complex cross-gable).

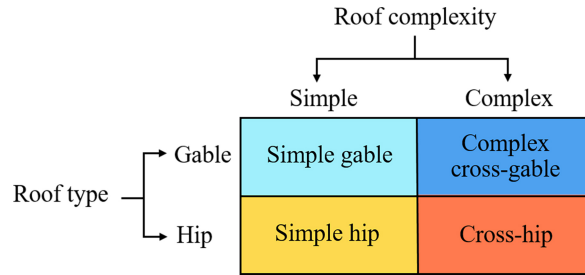


Figure 4.24: Process of mapping roof features predicted by imputation algorithms to roof types

Besides critical building characteristics, the spatial correlation of roof types is also considered to improve the performance of imputation models. As shown in Fig. 4.25, single-family houses in the same neighborhood tend to have similar roof styles. Therefore, roof type of a given building can be estimated based on the roof types of its neighboring buildings. The roof type (gable/hip) for each house in the building database is predicted using the dominant roof type (gable/hip) of the neighboring houses located within the search radius. For example, if more than 50% of neighbors for a given building have hip roofs, that building is predicted to have a hip roof. The *neighbor type* and the *neighbor complexity*, which represents the proportion of neighbors with gable roofs (i.e., simple gable, simple cross-gable, and complex cross-gable) and with complex roofs (i.e., simple cross-gable, complex cross-gable, and cross-hip), are calculated for each building and used as input features for training the machine learning models. The missing neighboring roof features were imputed using the mean values in the corresponding study area. The roof-type imputation process incorporating critical building characteristics and neighborhood-level roof characteristics is illustrated in Fig. 4.26. The training and testing of the roof-data imputation models are described through a case study in Section 4.4.1.



Figure 4.25: Neighborhoods with similar roof styles

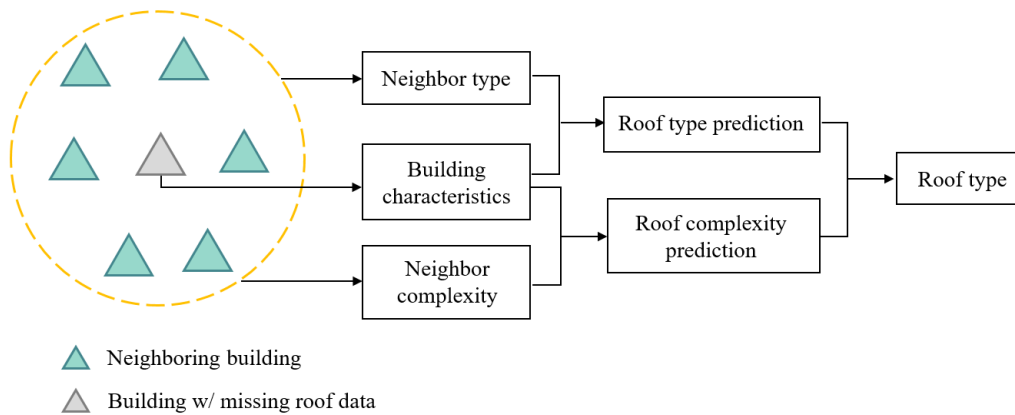


Figure 4.26: General steps of missing roof-type data imputation

4.3.3 Number of stories classification

4.3.3.1 Number of stories for single-family houses

As introduced in Section 2.1, the number of stories effects the wind vulnerability modeling on determining the building height and the distribution of openings. In the open terrain, wind pressures on roofs for two- and three-story buildings determined using ASCE 7-16 (ASCE, 2016) are about 7% and 15% higher than single-story buildings. Since the floor height is similar between single-family dwellings, the wall height can be estimated based on the number of stories. The distribution of the number of stories for single-family houses in New

Hanover County is listed in Table 4.7. As recorded in the ZTRAX database, most single-family houses are one- or two-story buildings, while very few houses have more than two stories.

Table 4.7: Distribution of number of stories for single family houses in New Hanover County (Zillow, 2018)

Number of stories	Number of buildings	Fraction
One-story	48670	71.0%
Two-story	19594	28.6%
Three-story and above	253	0.4%

When predicting the height of a single-family house based on the number of stories, special considerations need to be taken into account for elevated homes and houses with attics. In near-coastal areas, many homeowners choose to elevate their houses to reduce the impact of floods (English et al., 2017; Kreibich et al., 2005). The space beneath these elevated houses, referred to as the *base floor*, can be either enclosed or open with a height similar to the typical floor height (Fig. 4.27). However, the base floor of elevated houses is not recorded in the ZTRAX database, which can lead to underestimating the building height. On the other hand, many one-story houses with attics (Fig. 4.28) are considered having two stories in the ZTRAX database, which may result in an overestimation of the roof height.



Figure 4.27: Typical elevated single-family houses with different enclosure condition of the base floor: (a) Enclosed; (b) Partially enclosed; (c) Partially open



Figure 4.28: Single-story houses with attics considered to be two-story in ZTRAX

Consequently, two indicators of the number of building stories, n_s^h and n_s^o , are defined for estimating the building height and the opening layout, respectively. When counting n_s^h , attics are neglected, and the base floor of an elevated home is included. The value of n_s^o is determined by

$$n_s^o = \begin{cases} n_s^h, & \text{if } n_s^h < n_s^z. \\ n_s^z, & \text{otherwise.} \end{cases} \quad (4.8)$$

where n_s^z = number of stories obtained from ZTRAX. The number of stories for different types of houses are illustrated in Fig. 4.29. A CNN model is created to identify n_s^h using street view images. The prediction of n_s^h is treated as a classification problem since limited options of the number of stories are available for single-family houses. The houses are classified to

be one-, two-, or three-story, among which three-story houses are mainly represent elevated homes along the coastal line.

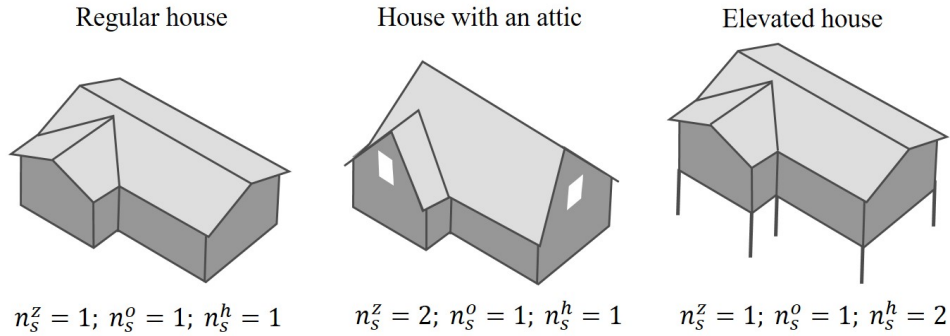


Figure 4.29: Number of stories for single-family houses

4.3.3.2 Overall workflow

The proposed workflow for predicting n_s^h is shown in Fig. 4.30. First, street view images are downloaded from Google Maps using Google Maps Street View Static API⁵. Next, images are fed into an image filter to remove the low-quality images that do not include a clear view of the house. Then, n_s^h for buildings with low-quality images is determined using the value of n_s^z , while n_s^h for the rest of buildings is classified based on the street view image using a CNN model developed in this study.

⁵<https://developers.google.com/maps/documentation/streetview>

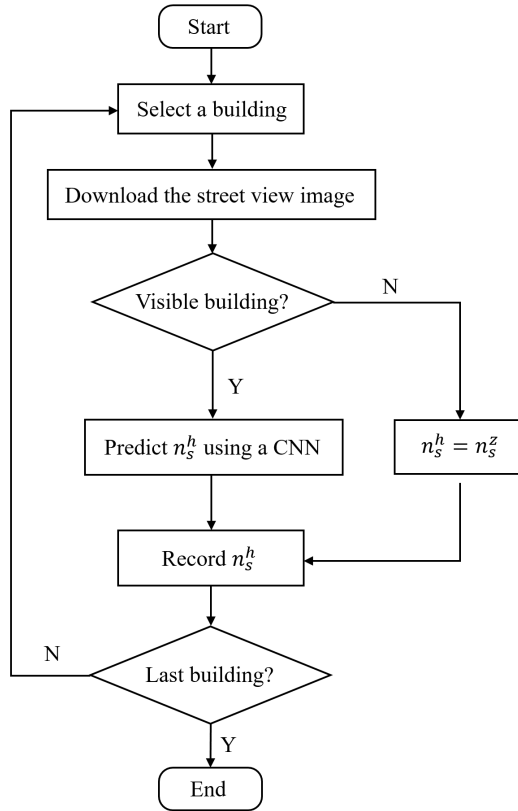


Figure 4.30: Flowchart for the number of stories classification process

Google Maps Street View Static API enables batch download of street view images. Given the building address, the camera is directed to the building by default. The parameter for defining the zoom level, fov , is set to be 60 for single-family houses. Images are downloaded to be the size of 400×400 pixels, and resized to be 224×224 pixels. Similar to the satellite images, low-quality street view images can also be obtained due to various reasons. The building can be blocked by the street trees (Fig. 4.31(a)), blurred as requested by house owners (Fig. 4.31(b)), or unavailable in the gated communities (Fig. 4.31(c)). The pre-trained Places365-ResNet (Zhou et al., 2017) is used to filter out the low-quality street view images by predicting the scene of the image. The Places365-CNNs are trained on the Places2 Dataset, including about 1.8 million images from 365 scene categories. The top 3 prediction results on the example street view images using pre-trained Places365-ResNet are

shown in Fig. 4.32. If the top 3 prediction results do not include any building-related scene category (e.g., house, garage/outdoor, and manufactured home), the image is considered to be low-quality and removed from the image dataset for the number of stories classification.

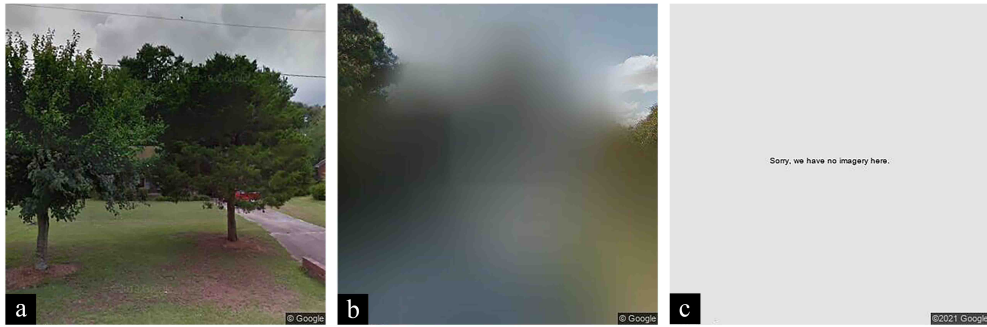


Figure 4.31: Example low-quality street view images: (a) The building is heavily blocked by trees; (b) The building is blurred; (c) The image is unavailable



Figure 4.32: Top 3 prediction results on example street view images using Places365-ResNet: (a) The building can be clearly viewed; (b) The building is heavily obscured; (c) The building is not visible

4.3.3.3 Training

A street view image dataset including 4,200 images, 1,400 images per class, is created for training the CNN model for the number of stories classification task. The dataset is split into 80% (1120 images per class) for training and 20% (280 images per class) for validation.

All images are manually classified into the three classes. The training images are mirrored to expand the training dataset. The representative training images for each class are shown in Fig. 4.33. A one-story house with an attic is labelled to be one-story, and the houses with a half second floor are considered as two-story buildings. The base floor of the raised houses is considered to be an additional floor. For example, the elevated one-story house is classified to be two-story. Similar to the roof type classification discussed in Section 4.3.2, the pre-trained VGG-19 network (Simonyan and Zisserman, 2014; Russakovsky et al., 2015) is fine-tuned using the aforementioned street view image dataset. The training parameters are set to be the same as those for training the VGG-19 model for roof classification. The fully connected layers are fine-tuned first for 26 epochs, and then the whole network is fine-tuned for 23 epochs. The confusion matrix of the CNN model evaluated on the validation dataset is shown in Fig 4.34. The overall prediction accuracy is 98.8%,

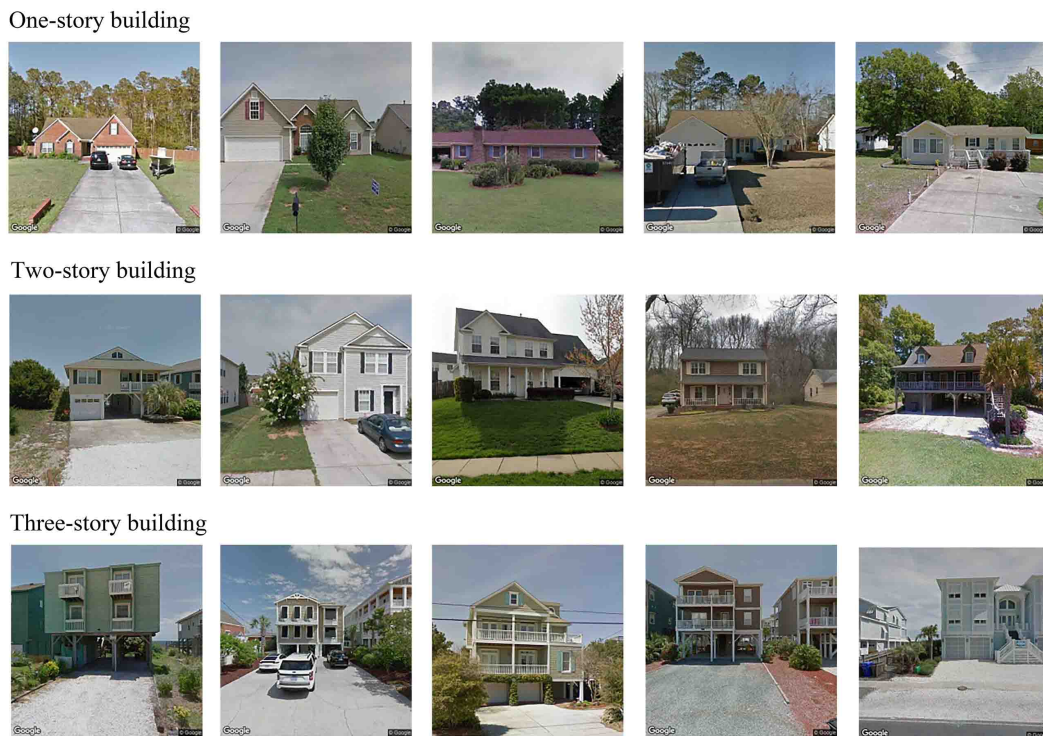


Figure 4.33: Example street view images in the training dataset for number of stories classification

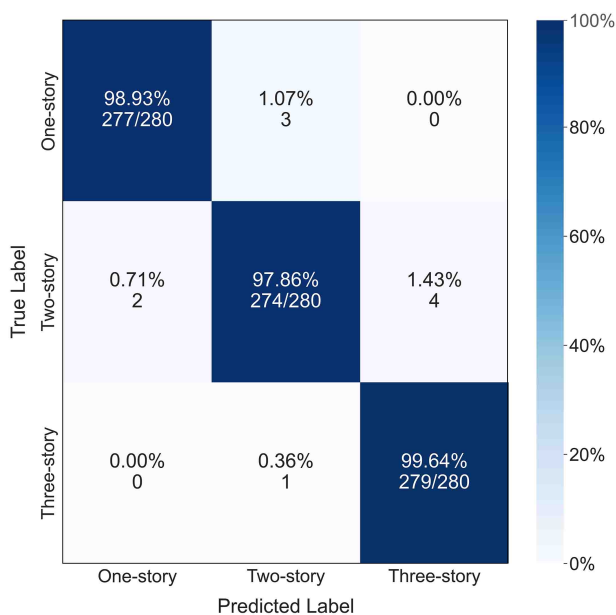


Figure 4.34: Confusion matrix of the number of stories classification model evaluated on the validation dataset

4.3.3.4 Testing

A testing dataset consisting of 500 street view images is constructed to evaluate the performance of the CNN model on classifying the number of stories. The testing images are randomly selected for single-family houses in New Hanover County and manually labelled. The example images in the testing dataset are shown in Fig. 4.35. The confusion matrix and the classification metrics of the VGG-19 network evaluated on the testing dataset are shown in Fig. 4.36 and Table 4.8. The CNN model shows high prediction accuracy for all classes. Lower prediction accuracy can be seen for two-story buildings compared to one- and three-story buildings. It is partially caused by the two-story houses with half second floor, which are hard to be differentiated from the one-story houses with attics. In summary, the CNN model is proved to be capable of identifying the number of stories efficiently and accurately. The image-based number of stories data also provide more reasonable estimation

of the mean roof height than using the real-estate number of stories data.

One-story building



Two-story building



Three-story building



Figure 4.35: Example street view images in the testing dataset for single-family houses in New Hanover County

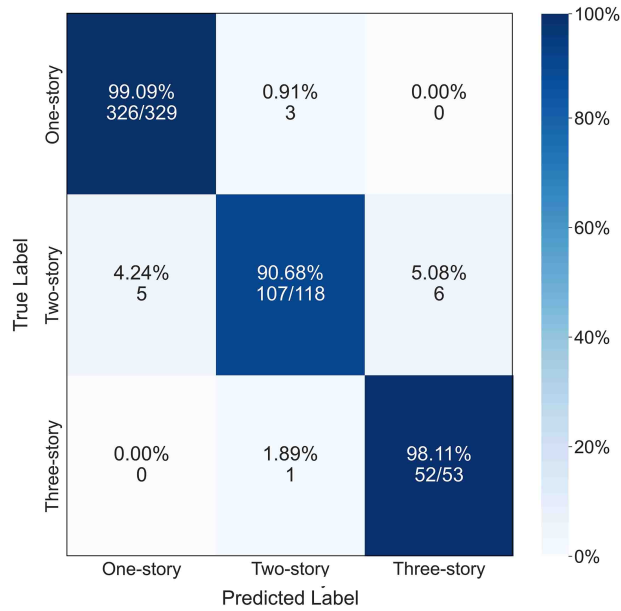


Figure 4.36: Confusion matrix of the number of stories classification model evaluated on the testing dataset

Table 4.8: Performance of the number of stories classification model on the testing dataset

Number of stories	Precision	Recall	F1 score	Support
One-story	0.98	0.99	0.99	329
Two-story	0.96	0.91	0.93	118
Three-story	0.90	0.98	0.94	53
Overall	0.97	0.97	0.97	500

4.3.4 Roof pitch prediction

4.3.4.1 Introduction

Roof pitch is a critical roof characteristic for 3D roof modeling. It affects the magnitude of the wind pressure on the roof, the layout of the roof components (e.g., roof sheathing

panels), and the resulting wind vulnerability. Roof pitch of 4/12 or 5/12 are adopted for defining the building archetypes for single-family dwellings in existing wind vulnerability models. Nevertheless, as shown in the roof distribution of the baseline building inventory (Fig. 4.7), considerable amount of houses have roof pitches beyond 5/12, which leads to significant difference in wind fragilities as discussed in Chapter 3. Therefore, the quality of roof pitch data is vital for the accuracy of the wind damage and loss calculation. Roof pitch data can be directly extracted from 3D LiDAR data (Mohajeri et al., 2018), which is costly and limited in availability. While the roof pitch can be measured from the building images following the steps described in Section 4.2, the process is difficult to be automated and generalized. Consequently, regression models were considered to predict the roof pitch using other building characteristics, which can produce roof pitch data efficiently with sufficient accuracy. The roof pitch data are converted to be in degrees for training and evaluating the models.

Since the roof pitch is not recorded in any available building inventory, the regression models are developed based on the baseline building inventory, as introduced in Section 4.2. Buildings with mixed-shape roofs were removed from the dataset, which resulted in 1,204 single-family houses in the building inventory. The available building features obtained from ZTRAX database and building images are summarized in Tables 4.1 and 4.2. De Barros Soares et al. (2021) used Random Forest to predict roof pitch with building features (e.g., roof material and roof type) for estimating solar potential of the rooftops. The resulting R^2 score and mean absolute error (MAE) of the model evaluated on the validation dataset are 0.37 and 5.5° , respectively. With different building characteristics available in our dataset, a feature selection process was implemented to find the most relevant building features, which can help reduce the quantities of input features, increase the efficiency of the model, and avoid overfitting.

4.3.4.2 Feature selection

As discussed in Chapter 3, roofs of pitch angles smaller and larger than 30° have significantly different wind fragilities for roof sheathing. Therefore, the roof pitch prediction model must be capable to differentiate steep-sloped roofs (larger or equal to $7/12$ (30°)) from the intermediate-sloped roofs ($3/12$ (14°) - $6/12$ (27°)). As required by building codes (ICC, 2018), attics of single-family houses needs to satisfy a minimum ceiling height, which relies on a relatively steep roof pitch (Fig. 4.37). Thus, identifying the attic condition of houses can largely enhance the model's performance in predicting steep roofs.



Figure 4.37: Representative single-family houses with attics and steep roofs. Roof pitch: (a) $8/12$ (34°); (b) $10/12$ (40°); (c) $16/12$ (53°)

Although not recorded in the ZTRAX database, the attic condition could be inferred from the available building area and number of stories data. An empirical equation is derived to determine if a single-family house has an attic

$$ATT = \begin{cases} 1, & \text{if } A_b + A_g - n_s^o(A_f + A_g) > 150 \text{ ft}^2 \text{ or } n_s^h < n_s^z. \\ 0, & \text{otherwise.} \end{cases} \quad (4.9)$$

where A_b , A_f , and A_g are the total building area, first floor area, and garage area provided in the ZTRAX database; n_s^z is the number of stories obtained from the ZTRAX database; n_s^o and n_s^h represent the number of stories for estimating the opening layout and the building

height. ATT equal to 1 indicates the building has an attic. The value of ATT is calculated for every building in the baseline building inventory. The distribution of roof pitch for houses with different attic conditions is presented in Fig. 4.38. Among buildings classified as having an attic, 97% of the buildings have roof pitch angles larger or equal to 7/12 (30.3°). It shows that Eq. 4.9 is effective in identifying the steep-sloped roofs.

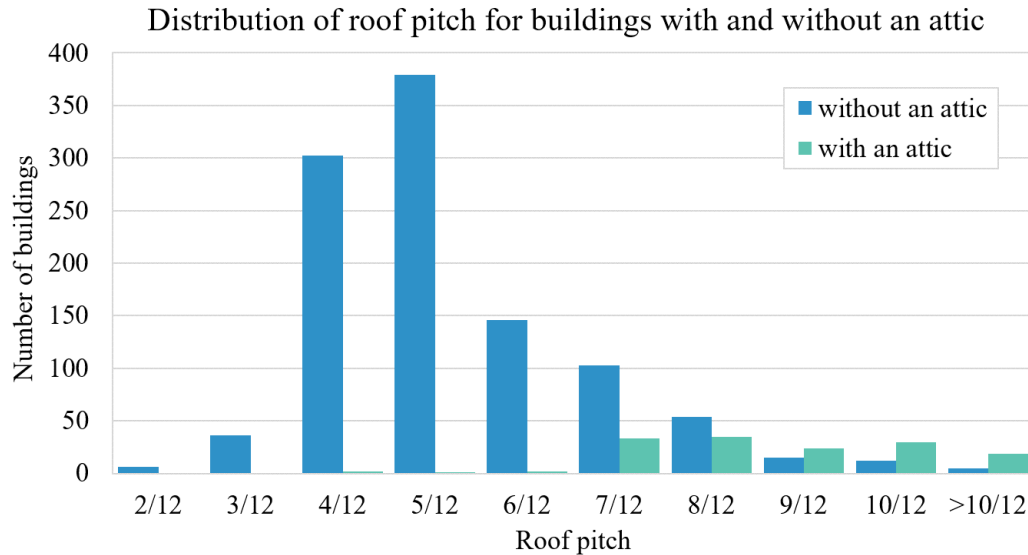


Figure 4.38: Distribution of roof pitch with different attic conditions for the baseline inventory

To identify collinear features, the hierarchical clustering analysis (HCA), which organizes the data points into groups based on their similarities, were implemented on the available building characteristics. The HCA was conducted on the Spearman rank-order correlations using Ward’s linkage. Dendrogram of the hierarchical clustering on the Spearman rank-order correlations and the heatmap of the correlation coefficients between the building features are shown in Fig. 4.39 (a) and (b). Different distance thresholds were evaluated to determine the optimal threshold for grouping the features. Random Forest is chosen to be fitted to the building data for predicting the roof pitch. For each threshold value, one feature is selected from each group and the model performance is assessed using 10-fold cross validation. The

comparison of model performance with different thresholds is shown in Fig. 4.40. It can be seen that the root mean square error (RMSE) stops decreasing after the threshold reaches 0.6. Accordingly, the tolerance threshold of 0.6 is chosen and nine groups of features are obtained. When selecting the features, the building attributes recorded in the ZTRAX database (e.g., first floor area) are prioritized over those extracted from the images (e.g., roof area) to avoid the erroneous data caused by the image-based data generation process. As a result, nine building features are selected after removing the collinear features: topography, garage area, year built, first floor area, exterior wall, roof type, number of stories, building value, and attic.

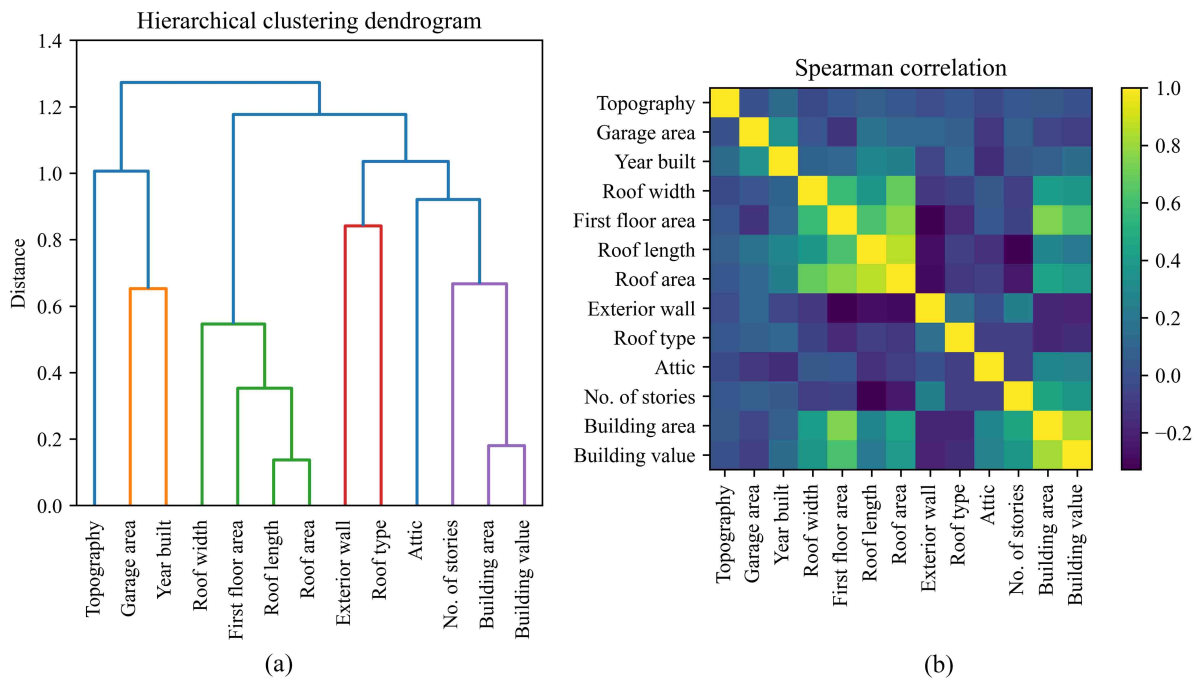


Figure 4.39: Correlation between building characteristics: (a) Dendrogram of the hierarchical clustering on the Spearman rank-order correlations; (b) Heatmap of the Spearman rank-order correlations

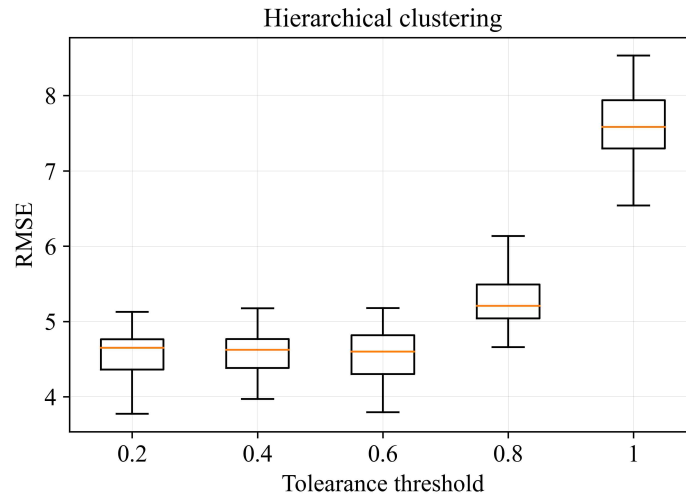


Figure 4.40: Comparison of the model performance on predicting roof pitch with different thresholds

To evaluate the relative contributions of building features in predicting roof pitch, permutation feature importance was calculated for each selected feature using the Random Forest Regressor. The building dataset was randomly split into 75% for training and 25% for validation. Figure 4.41 shows the permutation importance evaluated on the validation dataset. Results indicate that the attic condition and year built have the largest impact on the model performance, while building value, roof type, and first floor area also contribute to predicting the roof pitch. The rest of features, which showed minimal impact on prediction accuracy, were discarded. As a result, five features are used for roof pitch prediction, and the quantity of dependent variables is further condensed.

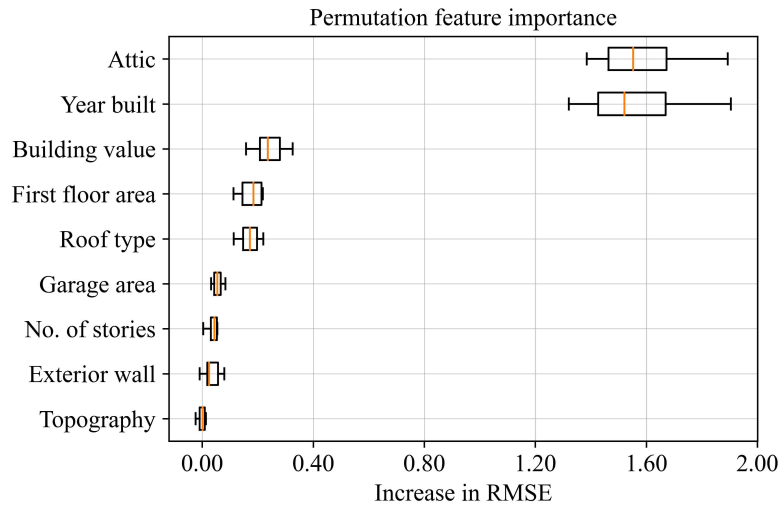


Figure 4.41: Permutation feature importance evaluated on validation dataset for roof pitch prediction using Random Forest

4.3.4.3 Training

Three advanced machine learning models, Random Forest, Support Vector Regression, and Gradient Boosted decision trees, are trained for predicting roof pitches. The hyperparameters of each model are tuned, and the performance of each model is evaluated using 10-fold cross-validation. The R^2 score and Root Mean Square Error (RMSE) calculated for each model are summarized in Table 4.9. The R^2 score represents the proportion of the total variance in the dependent variable that can be explained by the independent variables. A higher R^2 score indicates that the prediction results are closer to the ground truth. As shown in Table 4.9, the Random Forest algorithm outperformed the other two models and is thus selected for predicting roof pitch for the case study. The Random Forest model achieved a RMSE of 4.37° , which is approximately the difference between two adjacent standardized pitch values (e.g., the difference between roof pitches of 4/12 and 5/12 is 4.18°).

Table 4.9: Performance of machine learning models on roof pitch prediction

Model	R^2	RMSE
Random Forest	0.57	4.37°
Support Vector Regression	0.45	4.94°
Gradient Boosted decision trees	0.54	4.54°

4.3.4.4 Testing

To further evaluate the performance of the Random Forest algorithm on unseen data, a testing dataset comprised of 60 single-family houses in New Hanover County is created. The roof pitch for each testing building is measured from building images following the methods introduced in Section 4.2. The R^2 score and RMSE of the model evaluated on the testing dataset is 0.65 and 4.92 degree, respectively. For visualization of the results, the predicted roof pitch, which is in degree, is converted to the closest standard roof pitch (the ratio of inches rise per horizontal foot). The comparison between the predicted and ground truth roof pitch (Fig. 4.42) shows that the model could provide reasonable approximation of the roof pitch based on other building characteristics and many steep roofs are correctly identified. Figure 4.42 shows that the model tends to underestimate the roof pitch for steep roofs, which can result in conservative estimation of the wind damage.

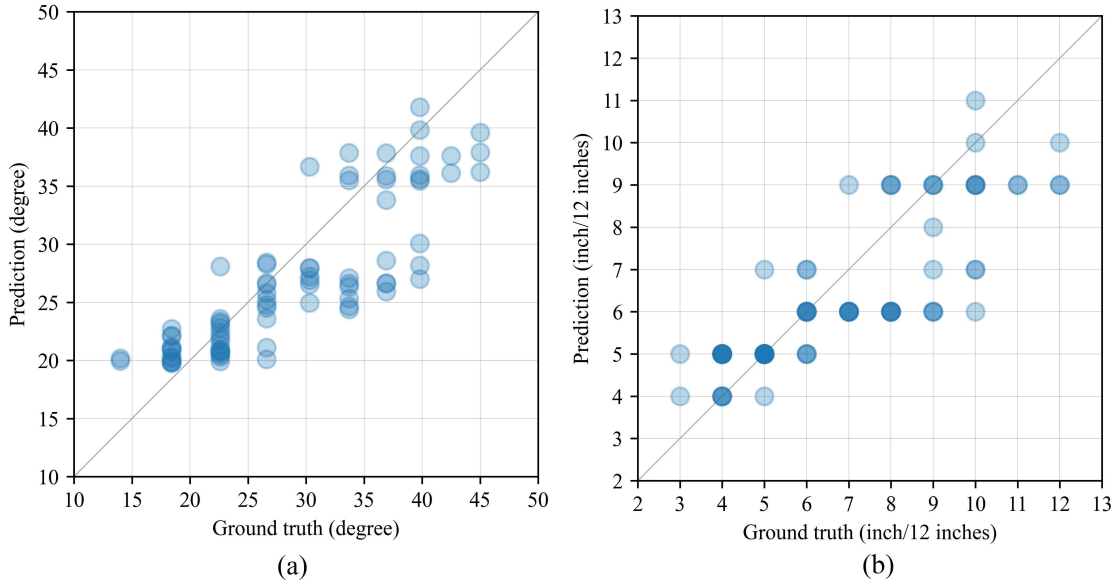


Figure 4.42: Prediction of roof pitch on testing dataset with Random Forest Regression: (a) Roof pitch in degree; (b) Standardized roof pitch

4.4 Case Study

Two sets of case studies were conducted to assess the generalizability of the proposed model in automatic building data collection. Section 4.4.1 presents the generation of city-level roof-type datasets using the roof type classification module described in Section 4.3.2. Section 4.4.2 presents the production of neighborhood-level building inventories, serving as the input for the wind loss model introduced in Chapter 5.

4.4.1 Roof type classification

As the essential building feature considered in existing wind vulnerability models, roof type is frequently missing from publicly available databases (Pita et al., 2008). To evaluate the distribution of roof types with the enriched roof classes proposed in this dissertation, the roof classification model was used to generate city-level roof-type datasets. Apart from New

Hanover County, the model was also applied to the central region of Miami-Dade County, FL (Fig. 4.43), where extensive studies on regional wind risk assessment have been conducted (Vickery, 2006; Pinelli et al., 2011). The building addresses for 68,504 and 93,268 single-family houses were obtained for New Hanover County and Miami-Dade County, respectively, from the ZTRAX database.

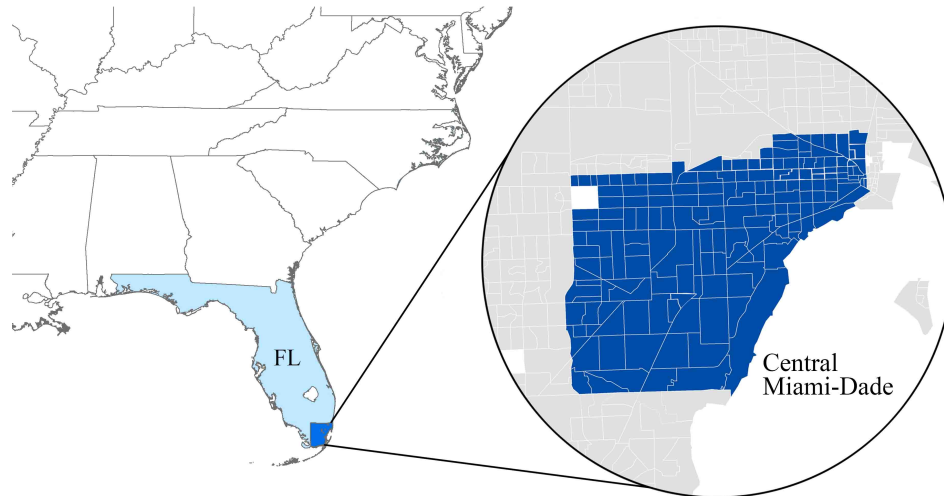


Figure 4.43: Case study area in Miami-Dade County and associated census tract boundaries

4.4.1.1 Roof type classification using satellite imagery

Given the building address, building-level satellite images were downloaded using Google APIs and cropped based on the floor area to optimize the scale of images. The CNN model was then applied to the obtained images to predict roof types. The predicted neighborhood-level roof type map is shown in Fig. 4.44, where roof-type labels are shown at building centroids obtained using Google Geocoding API. Valid roof-type data (i.e., roofs not classified as unknown) was obtained for more than 80% of buildings. Roof types for 17% and 11% of houses in New Hanover County and Miami-Dade County were classified as unknown, and the city-level roof type distribution for the rest of the houses is summarized in Fig. 4.45. It can be seen in Fig. 4.45 that gable roof is the dominant roof type in both areas, which is consistent

with the roof-type data collected by previous studies (Vickery, 2006; Crandell et al., 1993). The proportion of houses with hip roofs is 19% higher for New Hanover County than those for Miami-Dade County. The ratio between gable and hip roof in Miami-Dade County is 1.6:1, which is close to the ratio of 2:1 derived from tax appraisers' databases for Brevard County and Escambia County in Florida (Gurley et al., 2005). Regarding roof complexity, 72% and 63% of houses has complex roofs (i.e., simple cross-gable, complex cross-gable, and cross-hip) in New Hanover County and Miami-Dade County, respectively. On the other hand, a considerable amount of houses have simple rectangular roofs, and simple gable roof is the second most frequently observed roof type in both study areas.



Figure 4.44: Predicted roof type map for study areas

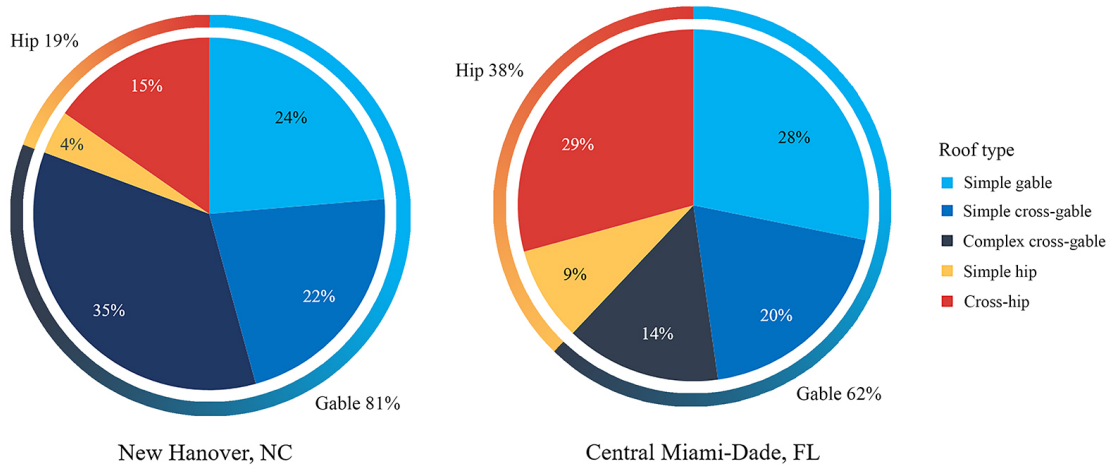


Figure 4.45: Roof type distribution for study areas

A census tract is often chosen as the geographic area unit for regional wind risk assessments. The distribution of building attributes, including roof type, is usually determined for each census tract to model the building stock. To investigate the distribution of roof type in the level of census tracts, the proportions of single-family houses with gable roofs (i.e., simple gable, simple cross-gable, and complex cross-gable) and complex roofs (i.e., simple cross-gable, complex cross-gable, and cross-hip) were calculated for each census tract in study areas and plotted in Figs. 4.46 and 4.47. As shown in Fig. 4.46, gable roof is the dominant roof type in all census tracts in New Hanover County, with the proportion of houses with gable roofs varying from 55% to 92%. On the contrary, in central Miami-Dade County, hip roof is the predominant roof type for 26% of census tracts. More than 80% of single-family houses have hip roofs in three census tracts. Regarding roof complexity, the proportion of houses with complex roofs varies between 39% and 97% in New Hanover County and between 16% and 97% in Miami-Dade County. Significant spatial variance in roof type distribution is shown at both city and census tract levels. Adjacent census tracts can have completely different roof type distribution. Therefore, detailed roof-type data is crucial for the accuracy of wind vulnerability assessments.

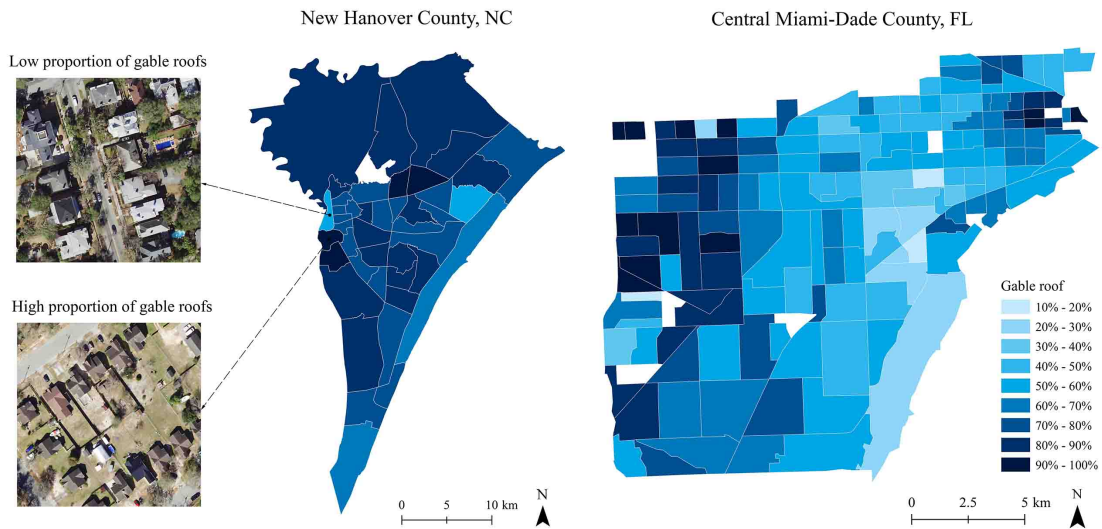


Figure 4.46: Fraction of single-family houses with gable roofs per census tract in study areas. (census tracts with less than ten houses were removed from the map)

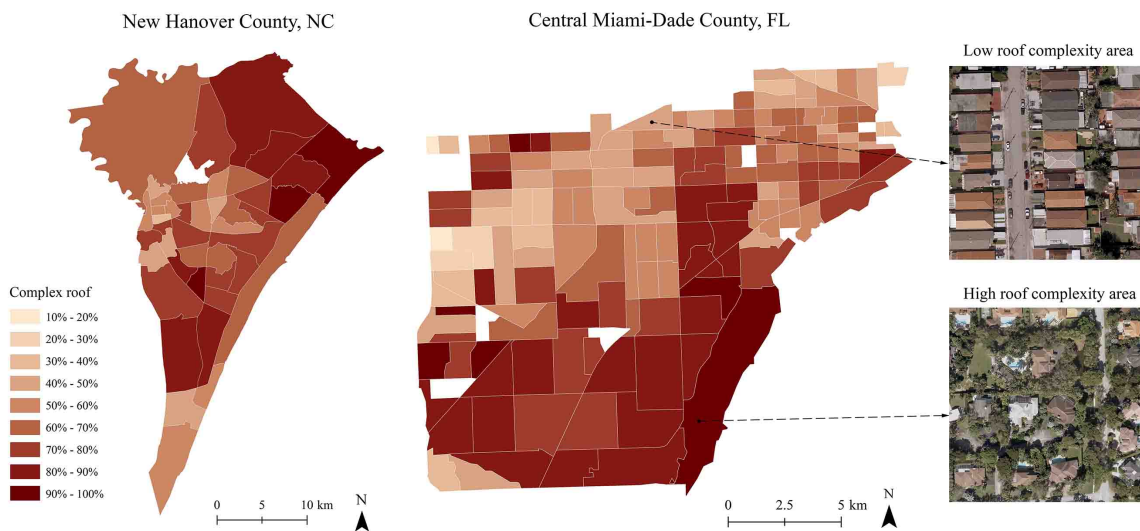


Figure 4.47: Fraction of single-family houses with complex roofs, including simple cross-gable, complex cross-gable and cross-hip roofs, per census tract in study areas (census tracts with less than ten houses were removed from the map)

4.4.1.2 Missing roof data population

As described in Section 4.3.2.5, data imputation models can be trained to predict missing roof types due to low-quality satellite images. Through the image-based roof classification, valid roof-type data was obtained for 56,863 and 76,045 single-family houses in New Hanover County and Miami-Dade County using the CNN model, which is considered as the ground truth for training the imputation models. Four values of search radius, 50m, 80m, 100m, and 150m (Fig. 4.48), were tested to find the optimal search radius for the neighboring buildings. Prediction accuracy was calculated based on the houses with neighboring houses available, and the proportion of homes without any neighbor within the search radius was counted. It can be seen in Table 4.10 that the prediction accuracy decreases with a larger search radius, while a smaller search radius results in a higher likelihood of failing to find neighbors. Consequently, a search radius of 80m is selected to ensure high prediction accuracy and data availability. The *neighbor type* and the *neighbor complexity* were calculated for each building and used as input features for training the machine learning models.



Figure 4.48: Candidate search radius used to calculate neighborhood-level roof type distribution for predicting missing roof-type data

Table 4.10: Prediction accuracy of roof type (gable or hip) using dominant roof type surrounding each building, and the proportion of buildings missing neighbors within the search radius

Search radius (m)	New Hanover		Miami-Dade	
	Accuracy	Missing data	Accuracy	Missing data
50	86.8%	6.5%	77.4%	4.3%
80	84.9%	1.6%	76.1%	0.7%
100	84.4%	0.9%	74.6%	0.2%
150	83.4%	0.5%	72.7%	0.2%

To select the most relevant features for predicting roof type, permutation feature importance was evaluated for all available building attributes, which measures the decrease in prediction accuracy when permuting a feature. Building database for each study area is split into 75% for training and 25% for validation. Permutation importance for each feature was calculated on the validation dataset for each model. Plots of permutation importance calculated based on Random Forest for buildings in Miami-Dade County are shown in Fig. 4.49 as an example. As expected, the roof style of neighboring buildings plays the most important role in roof type prediction. The *year built* and the *building area* are also found to be relevant for predicting the roof type, which is in agreement with conclusions drawn by Hamid (2021). The features selected for predicting roof type and roof complexity are summarized in Table 4.11.

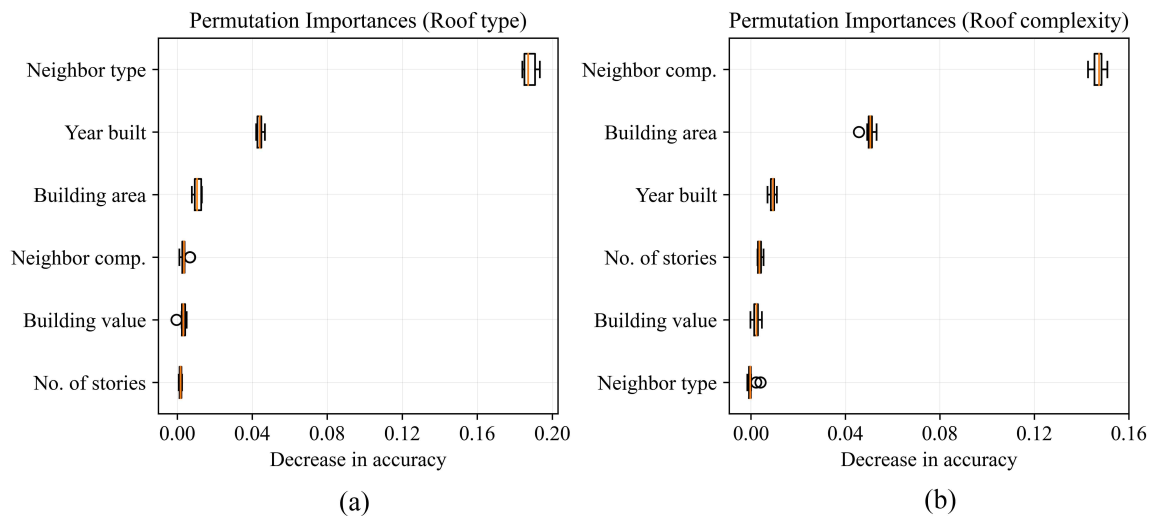


Figure 4.49: Permutation feature importance evaluated on validation dataset for Miami-Dade County with Random Forest : (a) Predicting roof to be gable or hip; (b) Predicting roof to be simple or complex

Table 4.11: Features used for roof type and roof complexity prediction with data imputation algorithms

Property	Category	Feature
Roof type	Gable/hip	Year built, building area, neighbor roof type
Roof complexity	Simple/complex	Year built, building area, neighbor roof complexity

Random Forest and Support Vector Machine algorithms were trained to predict roof type and roof complexity for each study area. The 10-fold cross-validation was implemented to assess the performance of each model. Two testing datasets, consisting of 200 houses with unknown roof types for each study area, were created to examine the capability of the models to predict missing roof data. Roof types of the testing buildings were manually labelled based on satellite and street view images downloaded from Google Maps. The locations and

the ground truth of roof types of the testing buildings are illustrated in Fig. 4.50. The validation and testing accuracy of each model predicting roof type and complexity are listed in Tables 4.12 and 4.13. Random Forest and Support Vector Machine show similar validation accuracy, while Random Forest performs better on the testing datasets. Moreover, the models achieved higher accuracy in predicting roof type than in predicting roof complexity. As shown in Tables 4.12 and 4.13, the testing accuracies are generally lower than the validation accuracies, which might be caused by the low-quality neighbor data for the buildings in the testing datasets. Buildings with unknown roof types are usually located in neighborhoods with high vegetation coverage, which increases the probability of those buildings having tree-blocked neighbors. In summary, the imputation models could provide reasonable estimation for the missing roof data, while the performance of the models drops in neighborhoods with high plant density. The prediction of the roof complexity is more sensitive to the quality of neighboring roof data than the prediction of roof type to be gable or hip.

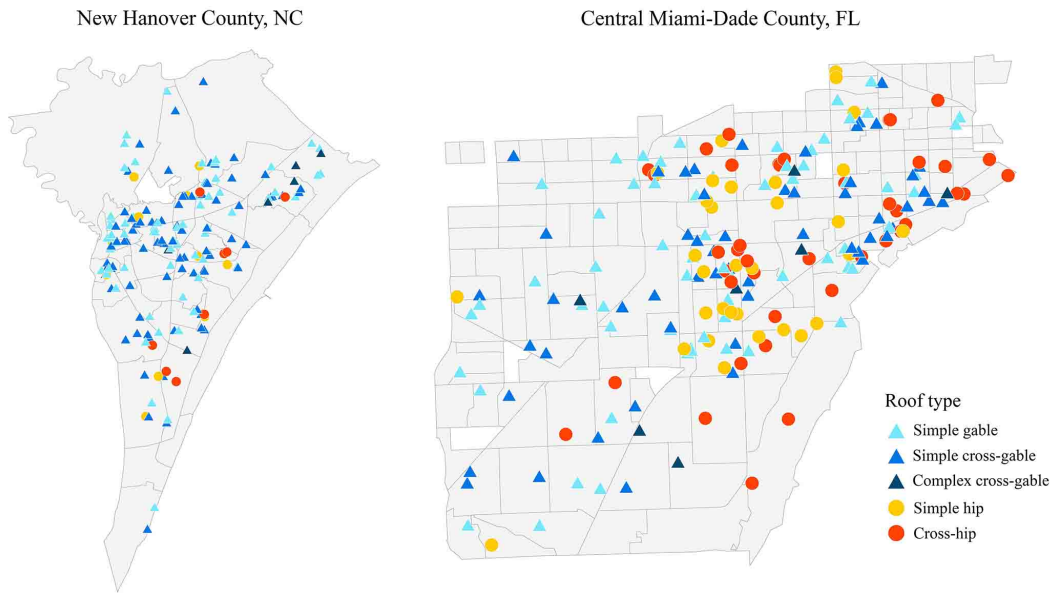


Figure 4.50: Location and ground truth roof type of buildings in the testing dataset

Table 4.12: Validation and testing accuracy of predicting roof type (gable or hip) with different models

Model	New Hanover		Miami-Dade	
	10-fold Cross Validation	Testing accuracy	10-fold Cross Validation	Testing accuracy
Random Forest	0.85	0.89	0.78	0.72
Support Vector Machine	0.85	0.88	0.77	0.68

Table 4.13: Validation and testing accuracy of predicting roof complexity (simple or complex) with different models

Model	New Hanover		Miami-Dade	
	10-fold Cross Validation	Testing accuracy	10-fold Cross Validation	Testing accuracy
Random Forest	0.81	0.64	0.77	0.66
Support Vector Machine	0.82	0.64	0.77	0.64

4.4.2 Building inventory generation

The building inventory generation model was implemented to the two neighborhoods introduced in Section 1.3. It can be seen from bird’s eye view images (Fig. 4.51) that study area 1 has lower building density and higher vegetation coverage than study area 2. In addition, houses in study area 1 are mainly single-story buildings, while many houses in study area 2 are multi-story elevated houses. As recorded in the ZTRAX database, there are 816 and 930 single-family houses in study areas 1 and 2, respectively. Building metadata was collected for each house following the process described in Section 4.1.



Figure 4.51: Bird eye's view images of study areas (images are from Google Earth)

Basic building information (e.g., year built, building value, and building area) was first gathered from the ZTRAX database. Distributions of year built and building value are shown in Figs. 4.52 and 4.53 with respect to the study area. As shown in Fig. 4.52, the year built for houses in study area 1 spreads between 1960 and 2000, while buildings in study area 2 were largely built around 2000. Twenty-one percent and eleven percent of single-family houses in study areas 1 and 2 were constructed before 1968, which may lead to lower wind resistance for those buildings. Regarding the building value (Fig. 4.53), houses in study area 2 are generally more expensive than those in study area 1. Building value for study area 2 is also observed to have a higher variance. The mean and standard deviation of building value are \$255,287 and \$75,552 dollars for study area 1, and \$376,127 and \$116,731 dollars for study area 2.

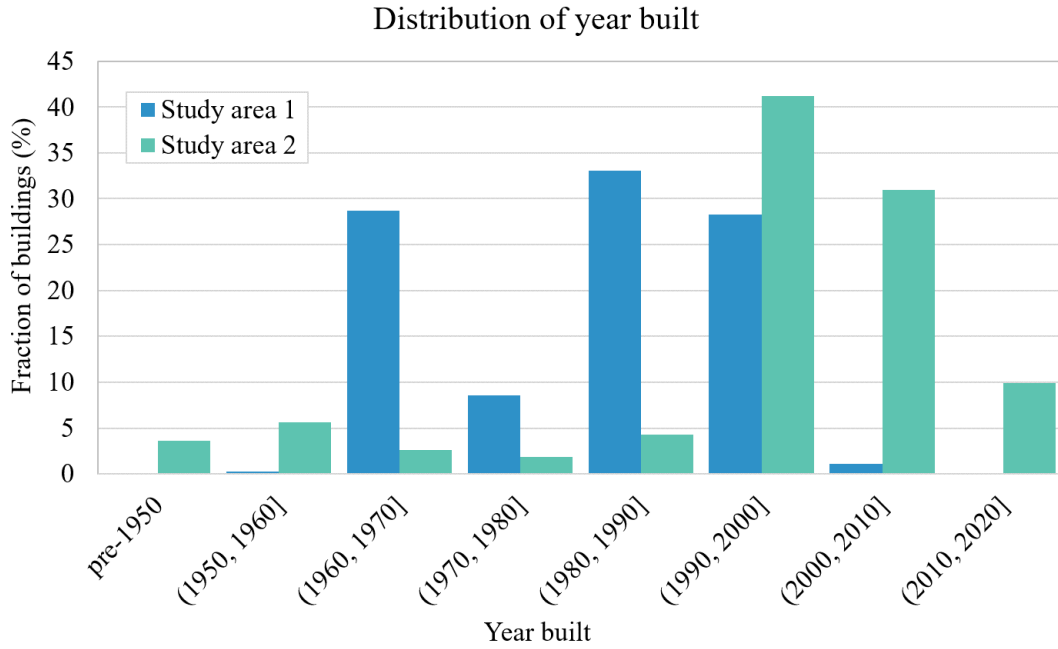


Figure 4.52: Distribution of year built for study areas

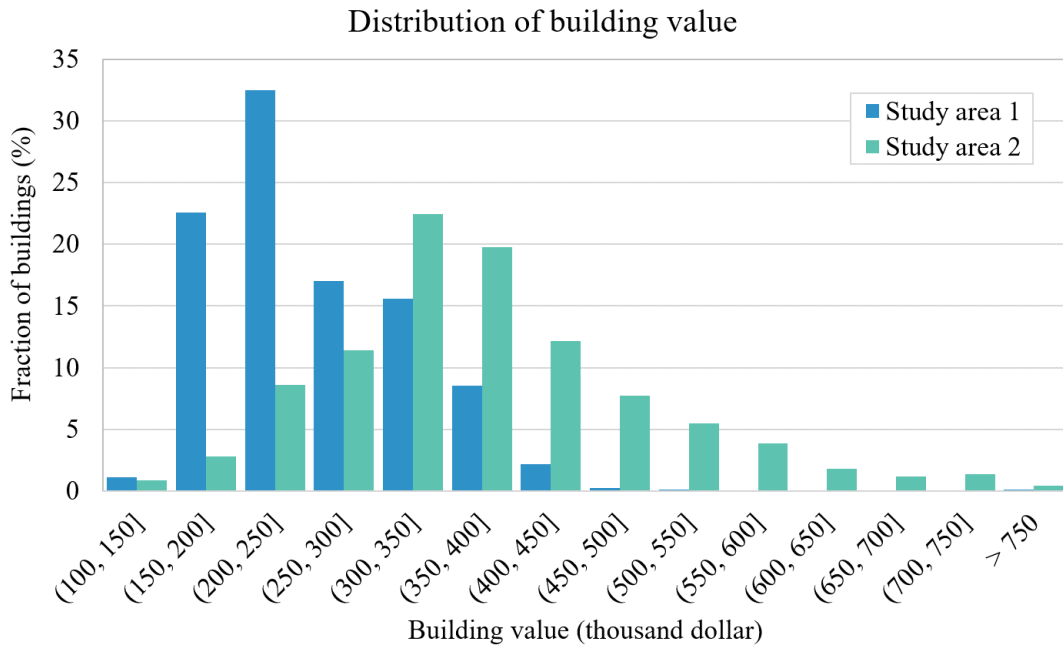


Figure 4.53: Distribution of building value for study areas

To measure basic roof plan dimensions (i.e., roof area, length, and width), roof outlines were extracted from satellite images using a roof segmentation model. Through the dimension correction and refinement process described in Section 4.3.1.3, plan dimensions of 12% (95 out of 816 buildings) and 17% (154 out of 930 buildings) of houses in study areas 1 and 2 were identified to be incorrect and recalculated based on building areas. Similar distributions of roof areas can be seen in Fig. 4.54 for study areas 1 and 2. The average roof areas for study areas 1 and 2 are 2749 sqft and 2111 sqft, respectively. The roof segmentation model also produced refined satellite images (Fig. 4.55) that reduced the disturbance from surrounding buildings, used as the input for the roof type classification module.

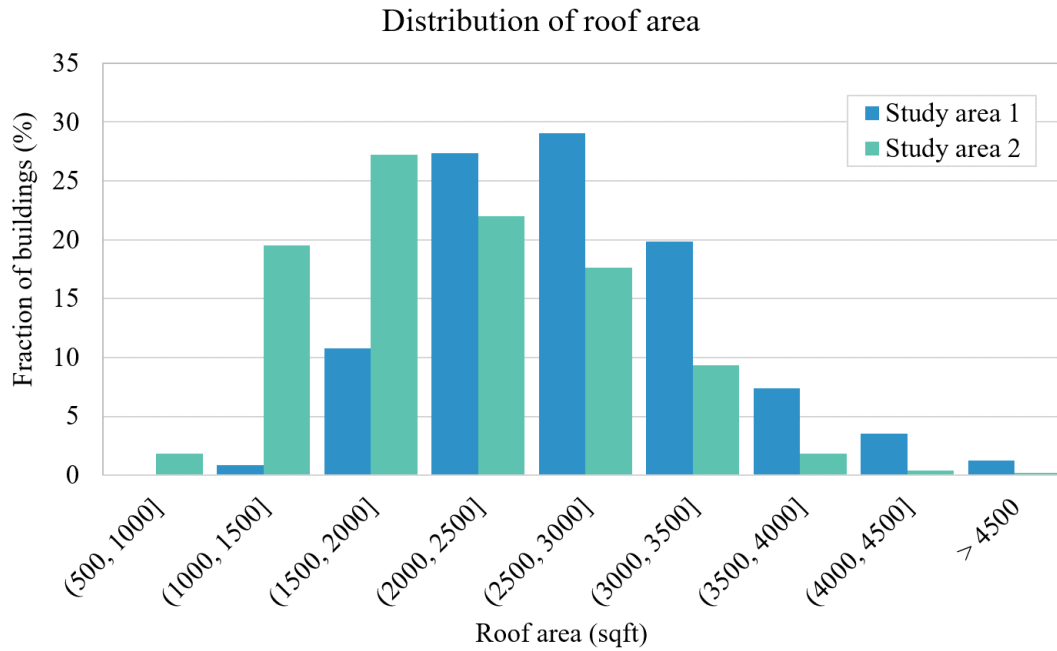


Figure 4.54: Distribution of roof area for study areas



Figure 4.55: Comparison between original images from Google Maps and refined images produced by the roof segmentation model

The VGG-19 network was then applied to refined satellite images to predict roof types. Roof types for 1% (9 out of 816 buildings) and 5% (47 out of 930 buildings) of buildings in study areas 1 and 2 were classified as unknown due to low-quality images. In study area 1, tree occlusion is the main cause of unknown roof types, while demolished houses account for most low-quality images in study area 2. Missing roof-type data were imputed using the Random Forest model following the process described in Section 4.4.1.2. Figure 4.56 presents distributions of roof types for study areas. As consistent with the city-level roof type distribution (Fig. 4.45), the gable roof is the dominant roof type in both neighborhoods. Nevertheless, the proportion of buildings with gable roofs is 26% higher in study area 1 than those in study area 2. In both study areas, nearly 60% of houses have complex roofs, and simple gable roof is the most frequently observed roof type.

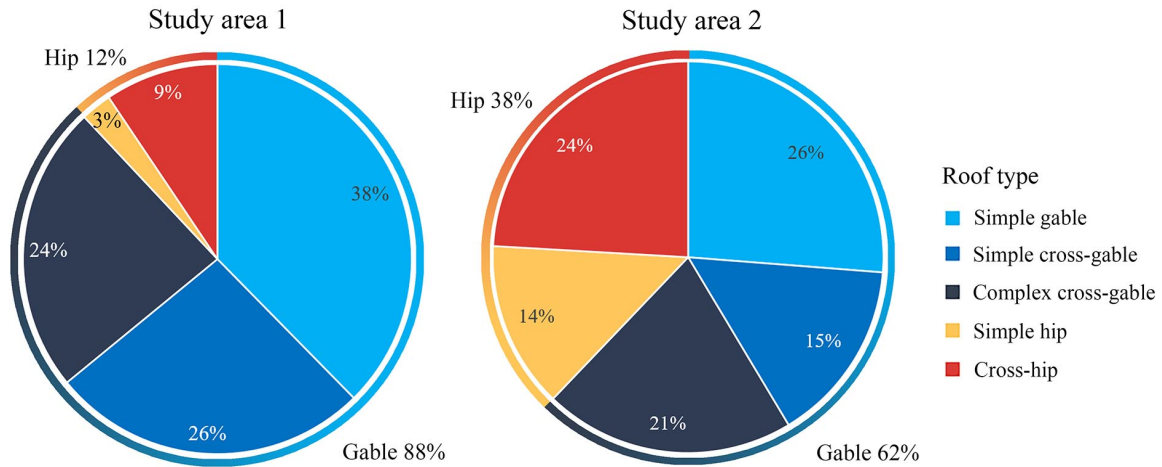


Figure 4.56: Distribution of roof type for study areas

The number of stories for estimating the building height (n_s^h) was extracted from street view images following the process presented in Section 4.3.3. First, the pre-trained Places365-ResNet was used to filter out low-quality images by predicting the image scene. Street view images for 65% (529 out of 816 buildings) and 92% (858 out of 930 buildings) of buildings in study areas 1 and 2 were identified to contain a clear view of the building, which is consistent with the fact that the study area 1 has a higher tree coverage. Next, a CNN was used to predict n_s^h based on street view images, and the missing n_s^h values were simply replaced by n_s^z (the number of stories provided by the ZTRAX database). The distribution of n_s^h is presented in Fig. 4.57, together with the distribution of n_s^z . The value of n_s^h differs from n_s^z for 9% (74 out of 816 buildings) and 45% (422 out of 930 buildings) houses in study areas 1 and 2. In study area 1, the existence of houses with attics resulted in lower proportion of two-story houses for n_s^h . While in the study area 2, elevated houses caused higher n_s^h values than n_s^z .

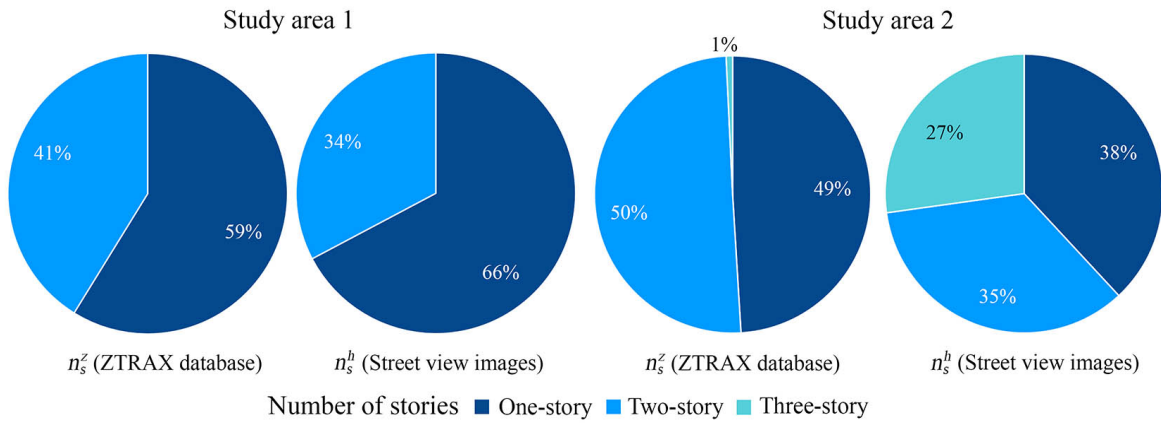


Figure 4.57: Distribution of number of stories for study areas

As the last step of the building inventory generation process, the roof pitch for each building was predicted using the Random Forest model based on critical building characteristics. Different roof pitch distributions (Fig. 4.58) were obtained for study areas 1 and 2 due to the variance in other building features (e.g., year built and building value) as discussed earlier. Roof pitches for buildings in study areas range from 4/12 (18°) to 10/12 (40°). The identification of very steep roofs was facilitated by considering the attic condition. Determined by Eq. 4.9, 26% and 43% of houses in study areas 1 and 2 are classified as having an attic. As observed from the prediction results, houses with attics were predicted to have roof pitches of at least 8/12 (34°). Houses with roofs steeper than 30° , which have substantial different wind performance than intermediate-sloped roofs, account for 46% and 75% of buildings in study areas 1 and 2.

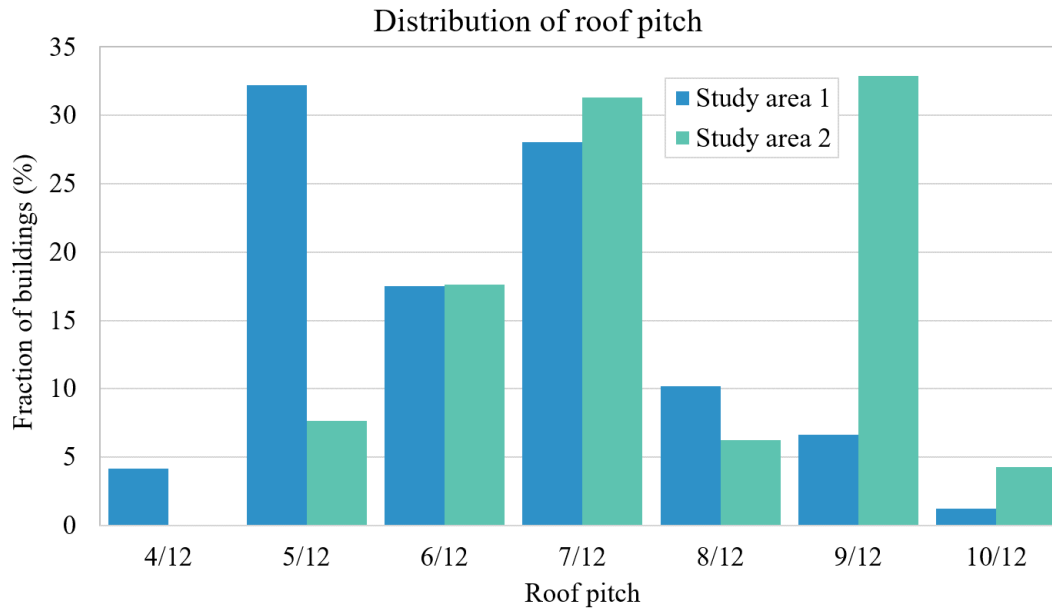


Figure 4.58: Distribution of roof pitch for study areas

The application of the building inventory generation model on study areas shows good generalizability of the data collection methods. Despite the complex residential environment, high-quality building images were obtained for most single-family houses. Data refinement and imputation algorithms incorporated into each data collection module enhanced the validity and completeness of the building inventory data. Special considerations for houses with attics and elevated homes further improve the accuracy of predicting building height and roof pitch. High-resolution building inventories created by the model revealed the variance of critical building characteristics in the neighborhood scale. More realistic building archetypes and more detailed regional wind loss models can be developed based on the high-resolution building inventory created by the proposed model.

4.5 Summary

This chapter presents an automated building inventory generation model for producing large-scale inventories for single-family houses. The process of creating building metadata was made efficient and low-cost by integrating remote sensing and real estate data with machine learning models. High prediction accuracy was achieved when evaluating each data collection module on labelled data in the study area. Considering deficiencies in the building images, validation and correction process is incorporated into data collection modules to identify low-quality images and incorrect prediction results. Corresponding imputation algorithms were developed to populate missing data and update erroneous data, which largely improve the reliability and completeness of the building inventory.

The proposed model demonstrated good generalizability in creating regional building inventories through case studies. The obtained building data offer insight into the distribution of critical building characteristics. High spatial variances of key building features were observed, showing that the quality and level of detail of the building inventory is crucial for the accuracy of regional wind damage and loss estimations. The high-resolution building database provides guidance for developing more realistic building archetypes compared to those adopted by existing wind vulnerability models. The building inventory produced by the proposed model can also be used as inputs for assessing the risk for other types of hazards (e.g., flood and earthquake). In Chapter 5, an automated site-specific wind risk assessment model is developed based on the enriched building inventory.

CHAPTER 5

DAMAGE AND LOSS ASSESSMENT MODEL

This chapter describes a regional loss model built upon the building feature data collected through the inventory generation model introduced in Chapter 4. The proposed model evaluates the direct loss due to wind pressure damage for single-family houses. The aggregated regional loss is calculated based on site-specific risk assessments applied to every house in the area of interest. To improve the accuracy of damage estimation, an automated building modeling workflow, which is developed based on roof archetypes constructed in Chapter 3, is integrated into the damage model. This model aims to improve the accuracy of damage and loss estimation by adopting more realistic and detailed building models. The building-level damage and loss results are used to evaluate the overall variance of the building's wind performance, considering uncertainties in architectural and structural properties. A case study of 1,746 single-family houses is conducted to evaluate the effects of architectural and structural features on the building's wind vulnerability. The change in regional loss consequences due to refined building models is also discussed.

Section 5.1 details the key components of the regional loss model. The hazard scenarios and building inventory are first described, followed by a thorough explanation of the site-specific risk assessment pipeline, which involves building modeling, damage analysis, and loss analysis. Section 5.2 presents the representative building models created for the damage analysis. Sections 5.1.5 - 5.4 show the damage and loss results for buildings in the study area. Finally, the limitations of the proposed model are discussed in Section 5.5.

5.1 Model Description

5.1.1 Overview

The regional loss model evaluates hurricane-induced loss for wood-frame single-family residential building stock through site-specific risk assessments. The model is developed based on parcel-based building inventories, which include architectural features, component resistances, and value of every single-family house in the region of interest. As shown in Fig. 5.1, the site-specific loss estimation consists of several steps conducted in sequence. For a given building, a 3D building model and associated component layouts are created based on architectural features, such as roof type and number of stories. Next, a component-based damage model is used to assess the damage condition for each modeled component. The damage model produces the distribution of component damage ratio as a function of wind speeds. Finally, the annual expected loss due to component damage is determined based on a set of probabilistic hurricane scenarios, which include the wind speed at the building location and the annual occurrence probability of each hurricane event.

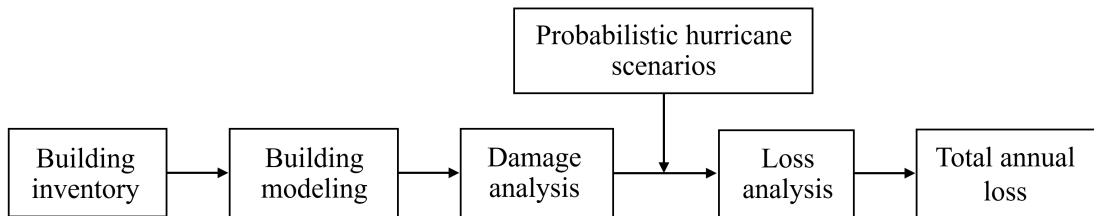


Figure 5.1: General steps for the site-specific wind loss model

Compared to existing regional loss models such as HAZUS-MH and FPHLM, several improvements are made to the proposed model: (1) The damage analysis includes non-rectangular buildings with complex-shaped roofs; (2) The variability of more building features (e.g., plan dimensions and roof pitch) are considered in the building models, which are treated as deterministic values in existing models; (3) Damage and loss estimation is conducted at individual building level, taking into account the correlations between different

building features.

5.1.2 Probabilistic hurricane scenario

The regional wind hazard was represented using a set of probabilistic hurricane scenarios developed by Apivatanagul et al. (2011). The hurricane scenario dataset was developed for the eastern half of North Carolina using the optimization-based probabilistic scenario (OPS) method. First, a large set of candidate hurricane scenarios, including over 50,000 scenarios that cover the entire study area and the full range of intensities, was constructed using the empirical track method (ETM) (Vickery et al., 2000). For each hurricane scenario, the wind speed was calculated for the centroid of each census tract. A reduced set of hurricanes that match the true hazard scenario was then selected using a mixed-integer linear optimization model (Apivatanagul et al., 2011). Finally, the adjusted annual occurrence probability was calculated for each hurricane event in the reduced set. The resulting hurricane scenario dataset consists of 97 hurricane scenarios with corresponding annual occurrence probability. For each hurricane scenario, the 3-sec gust wind speed at 10 m (33 ft) above ground is available for each 2010 census tract in the study area. The reduced hurricane dataset enables computationally efficient analysis of regional losses and captures the spatial correlation of wind speeds.

Buildings in each selected neighborhood are located within the same census tract. Consequently, the wind speed associated with each hurricane scenario is consistent among buildings in the same study area. The cumulative annual occurrence probability of the 97 hurricane scenarios for the study area is plotted in Fig. 5.2. The wind speeds associated with Saffir-Simpson hurricane wind scales are provided by ASCE 7-16 (ASCE, 2016). As shown in Fig. 5.2, the regional hazard scenarios used for the wind loss analysis are very similar between the two neighborhoods. The probability of at least one hurricane affecting the study area each year is approximately 32%. For study areas 1 and 2, the probabilities of experiencing at least one Category 1 hurricane per year are 4% and 5%, respectively.

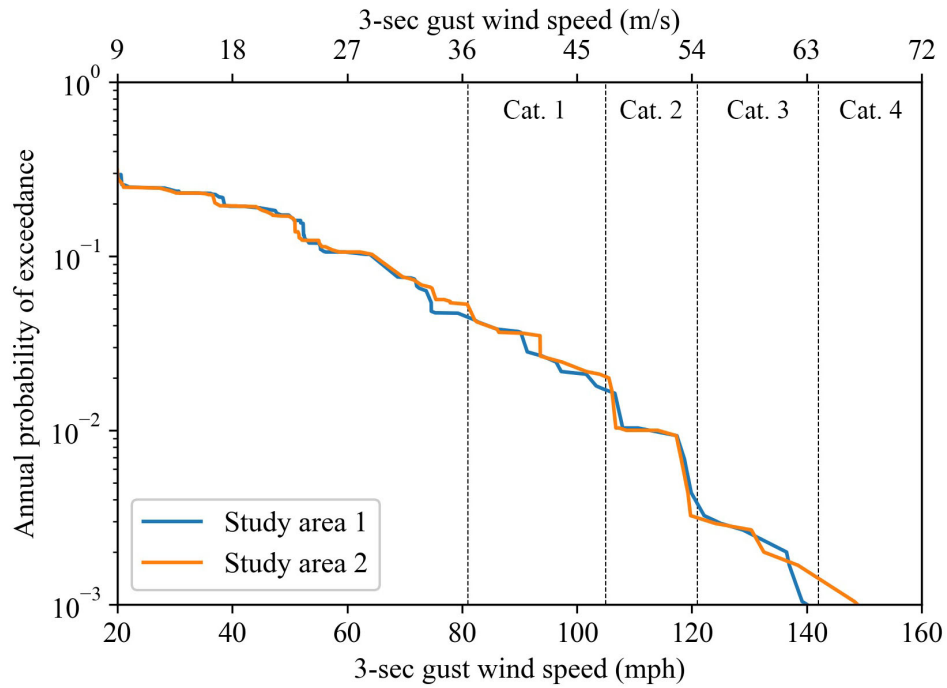


Figure 5.2: Annual exceedance probability of wind speed and associated hurricane categories for hurricane scenarios

5.1.3 Building inventory

The building inventory required for the loss model consists of three key components (Fig. 5.3): building geolocation, building configuration, and structural configuration. The building configuration includes the architectural features, as well as other critical building information such as construction year and building value. The structural configuration of each building, referred to as the component types and their associated wind resistance. The geolocation and building configurations for buildings in the study area were collected using the inventory generation model described in Chapter 4. Regarding the structural configuration, single-family houses in the United States typically are not engineered, and the building components usually have very similar configurations. With the evolution of building design code, wind mitigation strategies may be applied for different components to enhance the wind resistance. The

probability of having such alternations can be estimated based on the building’s geolocation and construction year (Peng, 2013; Hamid, 2021).

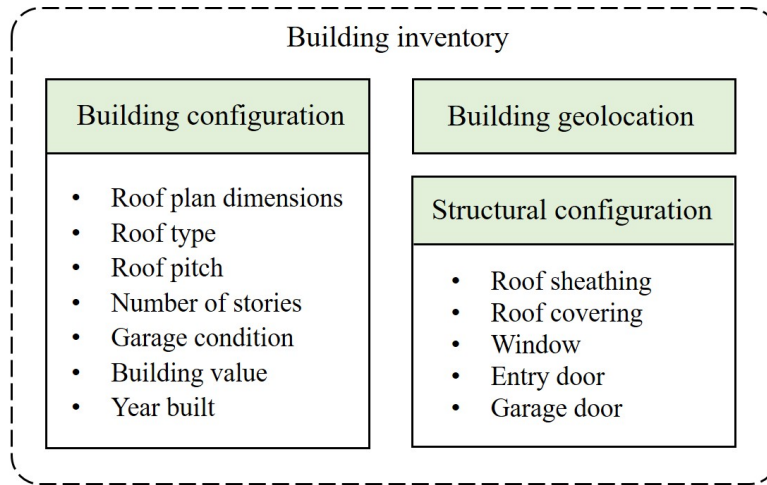


Figure 5.3: Key components of the building inventory

For the wind vulnerability model developed in this study, wind pressures are determined using a prescriptive approach based on ASCE 7-16 (ASCE, 2016). In the ASCE 7 standard, wind loads are calculated following different procedures for Main Wind Force Resisting System (MWFRS) and Components and Cladding (C&C). The MWFRS is defined as the structural components that resist wind loads transferred from other components, while C&C represents the building envelope components that experience wind loads directly, which are mainly non-structural components. The building components generally considered in wind damage analysis for wood-frame single-family houses are summarized in Table 5.1.

Table 5.1: Building components for wind damage modeling of wood-frame residential buildings

Component type	Component
Components and Cladding	Roof covering, roof sheathing, window, entry door, garage door
Main Wind Force Resisting System	Roof-to-wall connection, wall structure

While the code provisions are primarily developed for rectangular-shaped buildings with simple roof shapes, wind pressures on C&C for non-rectangular buildings can be determined using ASCE 7 (ASCE, 2016) by adjusting the wind zones, as introduced in Section 3.3.4. On the other hand, the calculation method for wind pressures on MWFRS is currently unavailable for buildings with irregular footprints due to the lack of experimental data. Furthermore, damage of the envelope components and the resulting water intrusion are the major causes of the wind loss (Ellingwood et al., 2004; Pita et al., 2012). Given these reasons, only C&C is considered in the damage and loss calculation in this dissertation. The proposed model can be easily adjusted to incorporate the MWFRS when wind data becomes available in the future.

Peng (2013) investigated typical component configurations and their retrofitted alternatives for single-family houses in New Hanover County. Multiple configurations were defined for each component type based on building design codes, local retrofit policies, common construction practices, and expert judgements. In this study, component configurations suggested by Peng (2013) are adopted for estimating the structural configuration for individual buildings, with modifications made to component capacities according to available literature. The component configurations and associated resistance statistics are summarized in Table 5.2. Peng (2013) also estimated the fraction of the building stock with each component configuration based on the building location (coastal or not) and year built. Since all buildings in the study area locate in the coastal area, distribution of component con-

figurations is simply determined by the year built (Table 5.3), resulting in total 9 different combinations of component configurations. The component configurations are sampled to each building based on the predefined probability, assuming that different component types occur independently.

Table 5.3: Estimated distribution of component configurations by year built (modified from Peng (2013))

Component	Configuration	Year built		
		Pre 1968	1968-1997	Post 1997
Roof covering (RC)	1	1	0.1	0
	2	0	0.9	1
Roof sheathing (RS)	1	1	1	0.5
	2	0	0	0.5
Openings (O)	1	1	0.8	0.5
	2	0	0.1	0.25
	3	0	0.1	0.25

5.1.4 Building modeling

The 3D building model is created for each home to determine the building and component geometries, which affect the quantity of component units and associated wind loads considered in the damage analysis. Based on the location of building components, C&C for single-family houses can be classified into roof components and wall components. Roof components consist of roof covering and roof sheathing, and wall components include windows, entry doors, and garage doors. The component-based wind vulnerability assessment requires the geometry and spatial location of each component unit, which is complicated and computationally expensive to be calculated with regular programming languages (e.g., Python and

Table 5.2: Resistance statistics of Components and Claddings (modified from Peng (2013))

Component	Config.	Description	Mean (psf)	COV	Distribution	Reference ^a
Roof covering (RC)	1	Standard asphalt shingles	50	0.4	Normal	1
	2	High wind asphalt shingles	70	0.15	Normal	1
Roof sheathing (RS)	1	8d C6/12	129	0.1	Lognormal	2
	2	8d C6/6	205	0.1	Lognormal	2
Openings (O)	1	Standard windows	70	0.2	Normal	1
		Standard doors	75	0.2	Normal	1
		Standard garage doors	50	0.2	Normal	1
Openings (O)	2	Impact resistant windows	140	0.2	Normal	1
		Standard doors	75	0.2	Normal	1
		Wind reinforced garage doors	75	0.2	Normal	1, 3
Openings (O)	3	Hurricane shutters on windows	105	0.2	Normal	1
		Hurricane shutters on doors	113	0.2	Normal	1
		Wind reinforced garage doors	75	0.2	Normal	1, 3

^a References: 1 = Gurley et al. 2005; 2 = Datin et al. 2011; 3 = Peng 2013.

MATLAB). Therefore, Grasshopper¹, a visual programming language for parametric modeling, is adopted to generate individual building models and component layouts. Grasshopper runs within Rhinoceros 3D computer-aided design application (Rhino)², and the modeling of a batch of buildings can be automated through the built-in Python editor in Rhino. The general steps for building modeling are shown in Fig. 5.4. First, the roof model is created based on roof geometries and roof type, followed by the generation of roof components. The wall structure is then modeled based on the roof outline and number of stories. Finally, the openings are created on each face of the building.

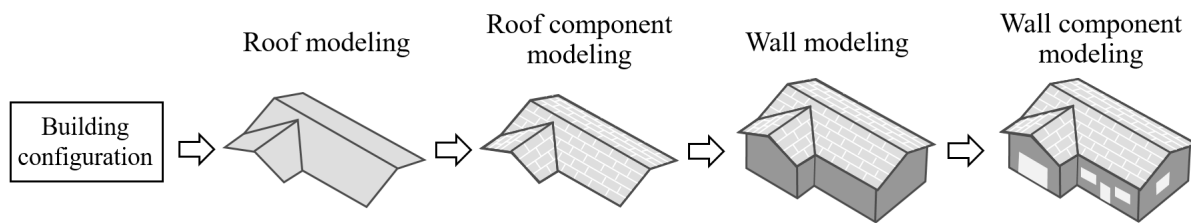


Figure 5.4: General steps for the building modeling process

Roof modeling

In previous studies, the construction of site-specific building models was achieved using 3D LiDAR data (Kashani et al., 2016; Zhou and Gong, 2018). However, creating such models requires high-quality remote sensing data, which are usually expensive and limited in availability. In addition, single-family houses often have irregular roof planes and mixed-shaped roofs, which are beyond the capability of existing damage assessment methodologies. Consequently, a simplified modeling approach (Fig. 5.5) is developed to produce computationally feasible roof models for damage calculations. Based on the sensitivity analysis described in Chapter 3, roof models are created by combining archetype roof plans (Fig. 3.18) with site-specific roof geometries (i.e., roof plan dimensions and roof pitch). The simplified roof

¹<https://www.grasshopper3d.com/>

²<https://www.rhino3d.com/>

model is expected to have similar wind performance (i.e., roof covering and roof sheathing fragility) to the true roof structure. Inputs needed for the roof modeling are the roof type (Table 3.4), roof plan dimensions (i.e., roof area, length, and width), and roof pitch.

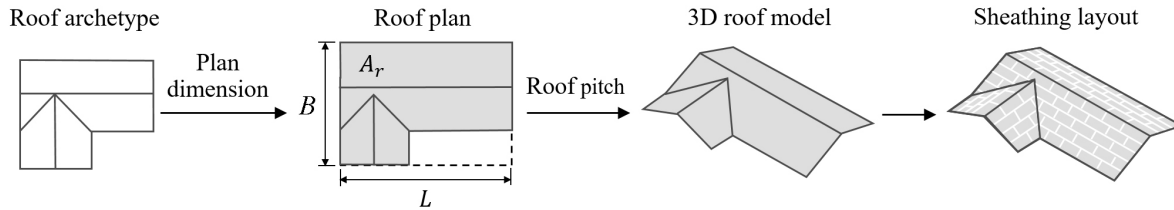


Figure 5.5: Roof modeling process

The roof modeling process begins with selecting the archetype roof plan based on the roof type. The detailed dimensions of the roof plan are then calculated through iterations to meet the basic roof plan dimensions. Based on the roof pitch, the roof plan is converted to the 3D roof model. One single roof pitch is used to model the entire roof, assuming all roof segments have the same roof slope. Following the creation of the roof model, roof sheathing panels are placed on each roof plane based on the common practice in single-family residential construction. Roof covering is modeled using the same layout as the roof sheathing instead of using their actual dimension for simplification (Gurley et al., 2005). Example roof plans and roof panel layouts for cross-hip roofs with different basic plan dimensions are illustrated in Fig. 5.6. The proposed method largely simplifies the requirements for input data for roof reconstruction. Meanwhile, the accuracy of the damage estimation is improved by adopting site-specific roof dimensions, compared to using building archetypes with deterministic dimensions.

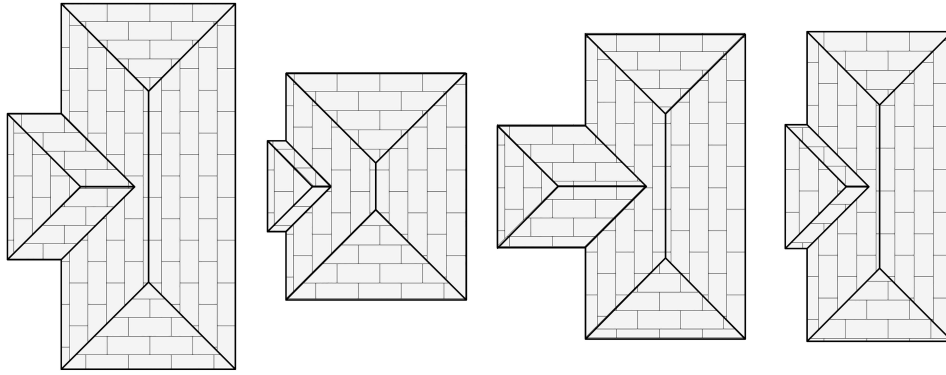


Figure 5.6: Roof plan and panel layout for cross-hip roofs with different plan dimensions

Wall modeling

Following the construction of roof model, outline of the wall structure is determined by offsetting the roof outline, assuming a roof overhang of 12 inches. The wall height is estimated by multiplying n_s^h by the story height, which is assumed to be 9 ft (Peng, 2013). Once the wall structure is modeled, openings are created on each face of the building. One single size is employed for each opening type, as shown in Table 5.4. First, windows are generated on each wall section along each story with spacing set to 15 ft. Next, two entry doors are placed on the front and back sides of the building. If the building has an attached garage, a garage door is modeled in the front face of the building. Finally, any window that overlaps with doors is removed. The opening layouts created for buildings with different roof shapes are depicted in Fig. 5.7.

Table 5.4: Dimension of openings for building modeling

Component	Width (ft)	Height (ft)
Window	6	3.5
Entry door	3	7
Garage door	9	7

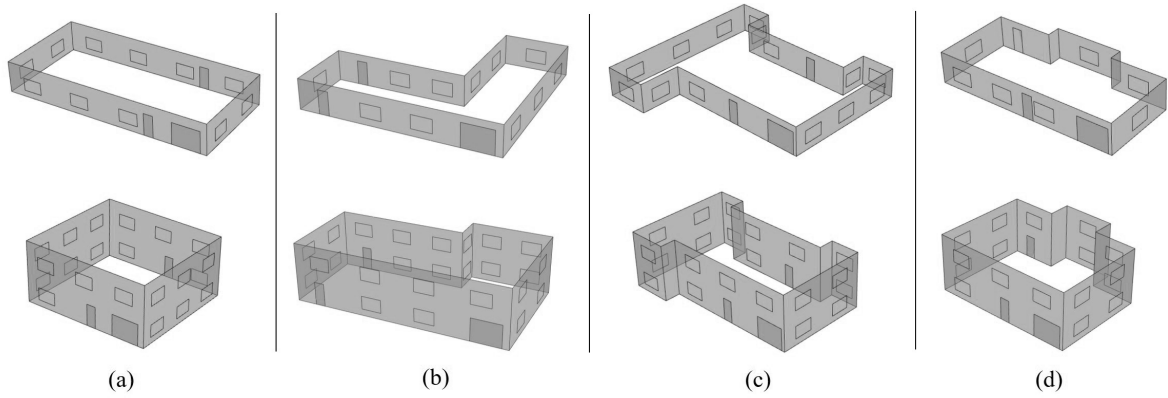


Figure 5.7: Opening layouts for buildings with different roof types: (a) Simple gable and hip; (b) Simple cross-gable; (c) Complex cross-gable; (d) Cross-hip

As introduced in Section 4.3.3, two indicators, n_s^h and n_s^o , are used to describe the number of stories for building height estimation and opening modeling. An elevated home can be identified using the following equation:

$$ELE = \begin{cases} 1, & \text{if } n_s^h > n_s^o. \\ 0, & \text{otherwise.} \end{cases} \quad (5.1)$$

where n_s^o is determined based on Eq. 4.8; $ELE = 1$ indicates that the house is elevated. In order to achieve a more accurate representation of the opening distribution, the opening generation for an elevated home simply skips the first floor, as demonstrated in Fig. 5.8.

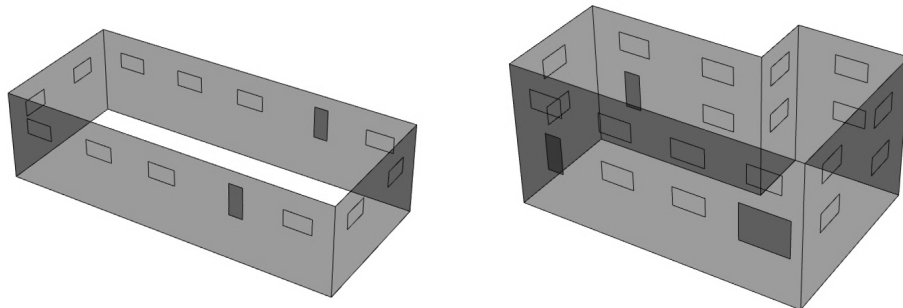


Figure 5.8: Opening layouts for elevated houses

5.1.5 Damage analysis

The estimation of wind-induced pressure damage is implemented with a component-based damage model. Each building is treated as a collection of building components, and each component consists of multiple units. The damage condition is checked for each component unit by comparing the wind load with resistance. The physical damage condition for component unit i is represented using a limit state function:

$$g(R_i, W_i, D_i) = R_i - (W_i - D_i) \quad (5.2)$$

where R_i = component capacity, W_i = wind load acting on the component, D_i = dead load (only applicable for roof components). The failure of individual component unit is defined as $g(\cdot) < 0$. The limit states considered in the proposed model are: (1) uplift of roof covering, (2) uplift of roof sheathing, (3) breakage of window, and (4) failure of entry door and garage door. To evaluate the damage condition in the building level, several damage states are defined to reflect the overall damage severity based on the damage condition of individual component, as proposed by HAZUS-MH (Hamid et al., 2011). The description of building damage states is summarized in Table 5.5. The damage ratio of roof components (i.e., roof covering and roof sheathing) is defined as the percentage of area damaged, while the damage ratio of openings is defined as the percentage of failed units. It should be noted that the damage to the roof-to-wall connection and wall structure is not considered for describing the building-level damage states since they are not modeled in this study, which only affects the DS4 defined by HAZUS-MH (Hamid et al., 2011).

Table 5.5: Damage states for wood-frame residential buildings

Damage state	Description	Roof covering failure	Roof sheathing failure	Opening failure
1	Minor damage	$> 2\%$ and $\leq 15\%^a$	No	One window, door, or garage door failure ^a
2	Moderate damage	$> 15\%$ and $\leq 50\%^a$	1 – 3 ^a	> 1 and \leq the larger of 20% and 3 ^a
3	Severe damage	$> 50\%^a$	> 3 and $\leq 25\%^a$	$>$ the larger of 20% and 3 and $\leq 50\%^a$
4	Destruction	Typically $> 50\%$	$> 25\%^a$	$> 50\%^a$

Note: Each damage state is defined as the occurrence of any component failure condition in the corresponding row marked with ^a.

Vulnerability and fragility curves are developed to visualize the damage results and compare the damage condition among different buildings. The component vulnerability is defined as the mean damage ratio of the corresponding component under a given wind speed. Based on the damage states defined in Table 5.5, the wind fragilities at the component level can be defined as the conditional probability of exceeding a specific damage state under a given wind speed v , which can be expressed as

$$Fr(V) = P[DS > ds_i | V = v] \quad (5.3)$$

At the building level, the fragility curve for damage state j is defined as the conditional probability of exceeding any of the marked component damage state at row j of Table 5.5 under a given wind speed v

$$Fr(V) = P[\bigcup_i (DS > ds_{ij}) | V = v] \quad (5.4)$$

Dead load is considered in the limit state function for roof components, which acts in the opposite direction as the uplift wind pressure. The dead load for roof cover, which is the self-weight asphalt shingles, is modeled by a normal distribution with the mean value of 2 psf and the coefficient of variation of 0.1 (Masoomi et al., 2018). The dead load of roof sheathing is considered as the sum of self-weights for roof covering and roof sheathing, which are sampled independently. The statistics for the self-weight of roof sheathing is summarized in Table 3.3.

Wind pressure acting on each component unit is determined using Eqs. 3.3 and 3.4. It is assumed that wind comes from any possible direction, and the wind directionality factor (K_d) is applied to account for the reduced probability of maximum winds coming from any direction and maximum wind pressure occurring for any given wind direction. The velocity pressure exposure coefficient (K_z) and external pressure coefficient (GC_p) vary among component units. K_z is determined based on the height of the component, which is assumed to be the height of the centroid for openings and the mean roof height for roof components. The aggregated GC_p for each component unit is calculated using the weighted-average method (Lee and Rosowsky, 2005), based on wind zones projected on the building model. The wind zones for C&C on roofs and walls are illustrated in Figs. 3.6 and 5.9, respectively. The nominal negative GC_p for zones 4 and 5 are -1.1 and -1.4 (ASCE, 2016). GC_p for roof zones, which is a function of roof type and roof pitch, are summarized in Appendix A. To be consistent with the FPHLM model (Gurley et al., 2005), the exposure category for the study area is assumed to be Exposure C. The statistics for other wind pressure coefficients are summarized in Table 3.3.

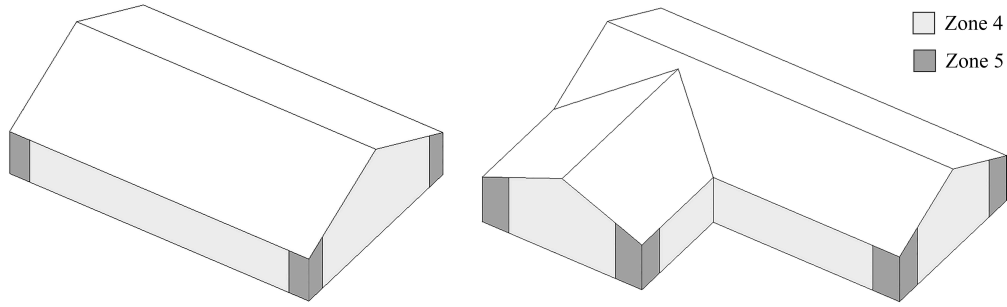


Figure 5.9: Wind pressure zones for GC_p for C&C on walls

Breaches in the building envelope caused by the failure of roof sheathing or openings have a substantial effect on internal pressure, which can trigger progressive damage to the structural system (Ji et al., 2020; Qin and Stewart, 2019). The effect of opening damage on internal pressures is coupled with wind directions (Gurley et al., 2005; Ji et al., 2020), which cannot be integrated into the proposed model due to a lack of experimental data for irregular buildings. Consequently, only the change of internal pressure due to roof sheathing failure is considered, and the deterministic approach (Lee and Rosowsky, 2005; Masoomi et al., 2018) described in Section 3.3.4 is adopted again for the building damage model.

Component resistance is sampled based on the predefined configurations using the corresponding distribution shown in Table 5.2. The capacities of building components in the same building are assumed to be partially correlated due to similar environment, material, and craftsmanship conditions (He and Hong, 2012). Correlation coefficients for capacities are assumed to be 0.4 between different units of the same component type (e.g., different roof sheathing panels), and 0.2 between different component types (e.g., roof sheathing and window) (Peng, 2013). For each building sample, the resistances for building components are generated from a multivariate normal distribution with the aforementioned correlation coefficients.

The damage analysis for individual buildings is performed through a Monte-Carlo simulation with 2,000 samples. A flowchart of the damage model is shown in Fig. 5.10. Forty-eight

discrete wind speeds and forty discrete damage ratio values are defined for the damage analysis, which are summarized in Appendix C. For each wind speed, the component damage condition is evaluated using a two-step check, as proposed by FPHLM (Gurley et al., 2005). During the initial failure check, the building envelope is considered to be intact, and the internal pressure is determined based on an enclosed building. The damage for roof covering and roof sheathing is checked based on randomized resistance, dead load, and wind load. Once the initial check is completed, the dead load and internal pressure are updated according to the damage condition of roof components. If a roof cover unit is damaged, the self-weight of roof covering will be excluded from the dead load for the roof sheathing at the same location. Conversely, the roof cover placed over a failed roof panel is directly set to be failed. If one roof sheathing panel fails, the internal pressure will be recalculated based on a partially enclosed building. Then, the final failure check is applied to all modeled components based on the updated loading condition, and the final damage ratio is computed for each component. Through 2,000 iterations, the probability of falling into each predefined damage ratio interval is calculated for each component.

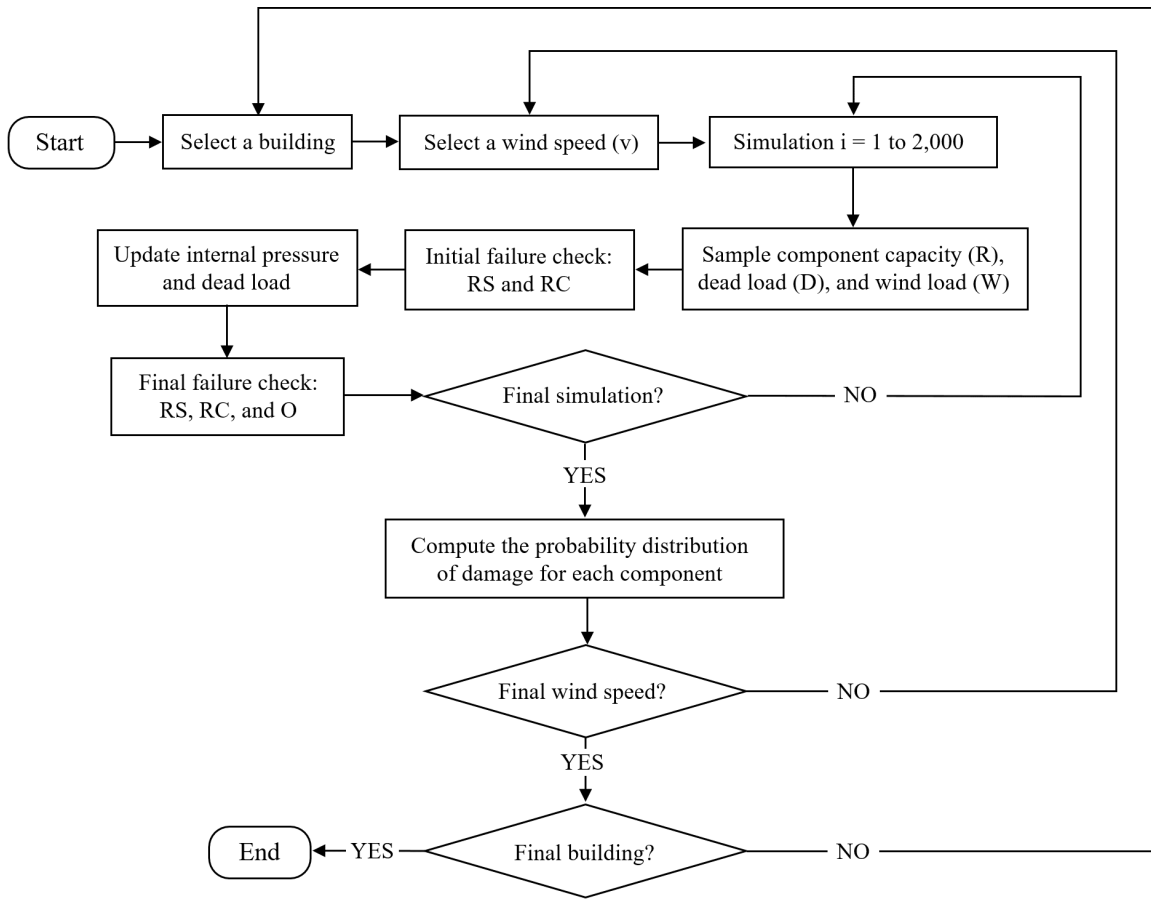


Figure 5.10: Flowchart of wind damage analysis

5.1.6 Loss analysis

The direct loss resulting from both exterior and interior damage is assessed for individual buildings. The exterior damage, represented by the damage ratio of building envelope components, is calculated using the damage model described in Section 5.1.5. The damage ratio of interior and utility components is estimated based on exterior damage, using a set of empirical equations developed by FPHLM (Gurley et al., 2005). The process of determining of interior damage is summarized in Appendix D for brevity. The economic loss is defined as the cost required to replace the damaged components, which is assumed to be proportional to the cost of constructing a new building of the same type. The replacement cost

ratio of each component, defined as the cost of replacing the component divided by the cost of constructing a new house, is calculated for a typical wood-frame single-family house in the FPHLM model. The replacement cost ratios for exterior and interior components, as provided by FPHLM, are summarized in Table 5.6.

Table 5.6: Component replacement ratio

Component	Replacement ratio (%)	Component	Replacement ratio (%)
Roof sheathing	5	Interior	35
Roof cover	6	Mechanical	7
Window	6	Electrical	9
Entry door	1	Plumbing	11
Garage door	2		

Additionally, the replacement threshold of roof sheathing and roof covering is set to be 35% (Gurley et al., 2005). It means that if more than 35% of roof sheathing or roof covering fails, all roof sheathing or roof covering units need to be replaced. The cost of replacing the whole building is estimated using the building value (BV) provided by the ZTRAX database. Using the probabilistic hurricane scenarios described in Section 5.1.2, the expected annual loss (EAL) for individual buildings is determined by

$$EAL = \sum_{i=1}^{n_c} \sum_{j=1}^{n_h} \sum_{k=1}^{n_d} BV \cdot C_i \cdot P_i[DR = dr_k | V = v_j] \cdot h_j \quad (5.5)$$

where n_c = number of components; n_h = number of hurricanes; n_d = number of damage ratios; C_i = replacement cost ratio of component i ; dr_k = damage ratio k ; v_j = wind speed of hurricane scenario j ; $P_i[DR|V]$ = probability of component i experiencing damage ratio DR given wind speed V ; h_j = annual occurrence probability of hurricane scenario j . The regional loss is computed by summing up the EAL for every house in the study area.

5.2 Building Modeling Results

Building models are created for houses in the study area following the process described in Section 5.1.4. Representative building models with the associated true structures are depicted in Fig. 5.11. In the case of buildings with rectangular footprints and simple roof shapes (Figs. 5.11 (a) and (d)), building models closely match the actual structure because the archetype roof configuration for simple roofs is identical to the actual roof configuration. For non-rectangular buildings (Figs. 5.11 (b), (c), and (e)), roof models are simplified by the roof archetypes, which capture the dominant roof type (gable/hip) and relative roof complexity. Additionally, special building features, such as the steep roof of building with an attic (Figs. 5.11 (c)) and the increased height of elevated houses (Figs. 5.11 (e)), are reflected in the building models. The incorporation of a variety of site-specific variables into the modeling process largely reduces the inherent uncertainty in quantifying the building resistance. From the perspective of disaster risk assessment, the simplification and idealization of the building models are beneficial and necessary. For instance, irregular roof planes (Fig. 5.11 (a)) and vertical irregularities (Fig. 5.11 (f)) are frequently observed in residential constructions, which are beyond the capability of existing damage analysis methods. However, those features are automatically disregarded through the modeling process, resulting in building models that are suitable for the site-specific risk assessment.

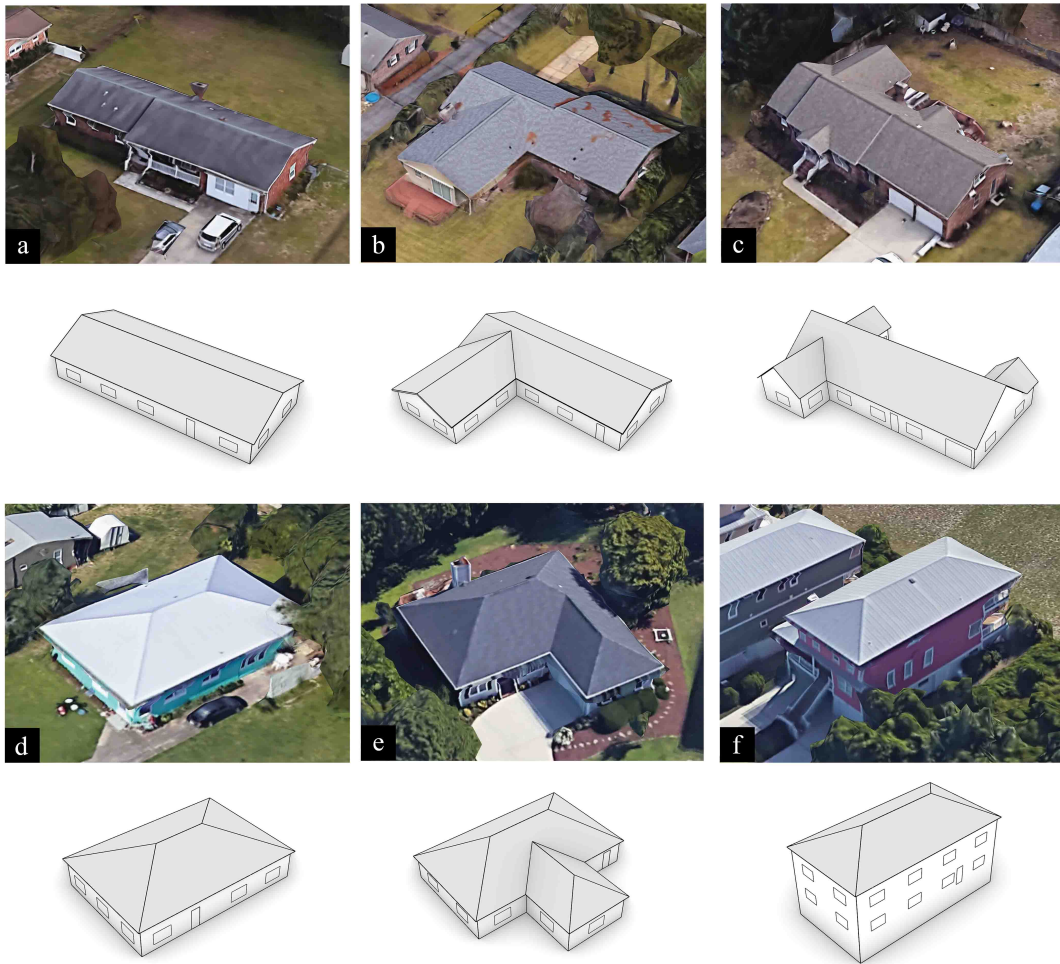


Figure 5.11: Comparison between building models and actual structures (building images are from Google Earth)

5.3 Damage Results

The pressure-induced wind damage is assessed for 1,746 houses in the two neighborhoods using the component-based damage model described in Section 5.1.5. The damage results are presented in both component and building levels based on the damage states defined in Table 5.5. The large-scale building inventory adopted for the damage analysis incorporates most possible combinations of critical building characteristics, providing a good representa-

tion of the overall distribution of wind vulnerabilities for single-family houses.

5.3.1 Component-level damage results

The damage vulnerability curves of roof components (i.e., roof covering and roof sheathing) are plotted in Fig. 5.12 with respect to different component configurations. The component configurations considered for the case study are described in Table 5.2. As shown in Fig. 5.12 (a), damage curves for buildings with a strong roof sheathing configuration (RS2) are all on the right side of those with the standard configuration (RS1). It demonstrates that, regardless of variations in the building configuration, buildings with RS1 are expected to experience more severe roof sheathing damage than those with RS2. In the case of roof cover vulnerabilities (Fig. 5.12 (b)), roof covering with higher capacities (RC2) also show substantially lower damage ratios. Nevertheless, it can be seen that several curves associated with different roof cover types cross over each other, indicating that buildings with RC2 may have a higher expected damage ratio than those with RC1 due to the differences in architectural features (e.g., roof type and number of stories). Additionally, substantial variances in the damage curves are observed for buildings with the same roof sheathing or roof covering configuration, indicating that the building configuration effects the roof vulnerability considerably. The variance in roof vulnerabilities for the same component type is attributed to the site-specific building features considered in the building models, including roof type, roof pitch, roof dimension, and mean roof height. These variables impact both the number of component units and the wind pressure acting on each unit. Under a Category 3 hurricane (122-142 mph), the differences in mean damage ratios among different buildings can be up to 16% and 38% for RS1 and RC1, respectively.

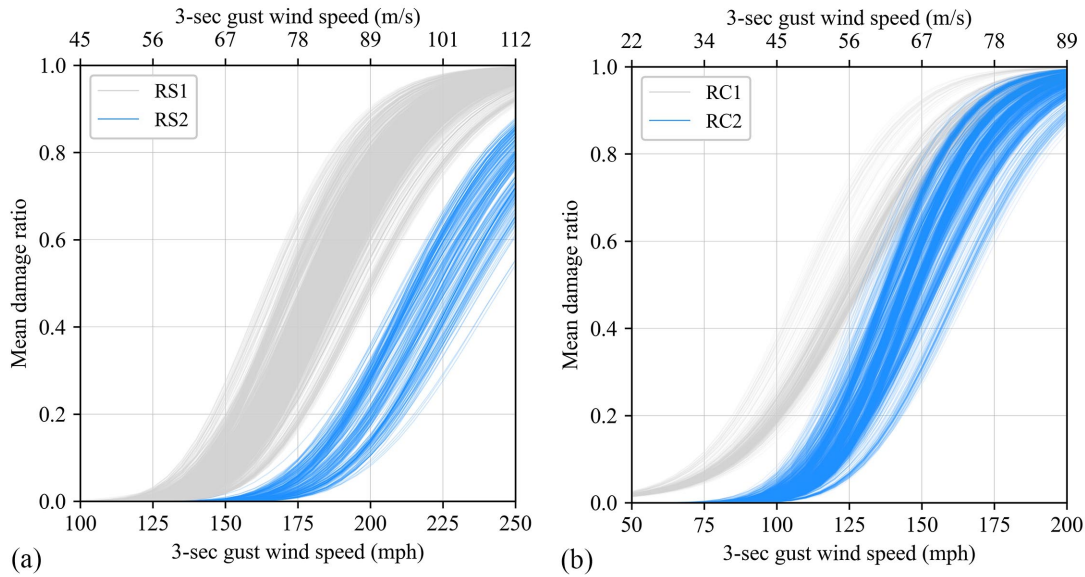


Figure 5.12: Damage vulnerability for roof components: (a) Roof sheathing; (b) Roof covering

Figure 5.13 shows the roof sheathing fragility curves for exceeding DS1 and DS3. The fragility curves for exceeding DS1 (Fig. 5.13 (a)) exhibit wide variability, with several buildings with RS2 having higher fragilities than those with RS1. As shown in Fig. 5.13 (b), the fragility curves associated with the same sheathing type demonstrate lower variance for DS3 than for DS1. This suggests that the impact of building configuration is reduced for more severe damage states, which may be partially due to the exclusion of the roof-to-wall connection damage in the damage model. Conversely, the difference between fragility curves of RC1 and RC2 (Fig. 5.14) is smaller for DS2 than for DS1. For all evaluated buildings, the average median wind speeds for RC1 and RC2 are 101 mph and 130 mph, respectively, for exceeding DS1, and 127 mph and 149 mph, respectively, for exceeding DS2. The overall variance among fragility curves for roof covering is less than that for roof sheathing, taking into account the variability in architectural and structural properties.

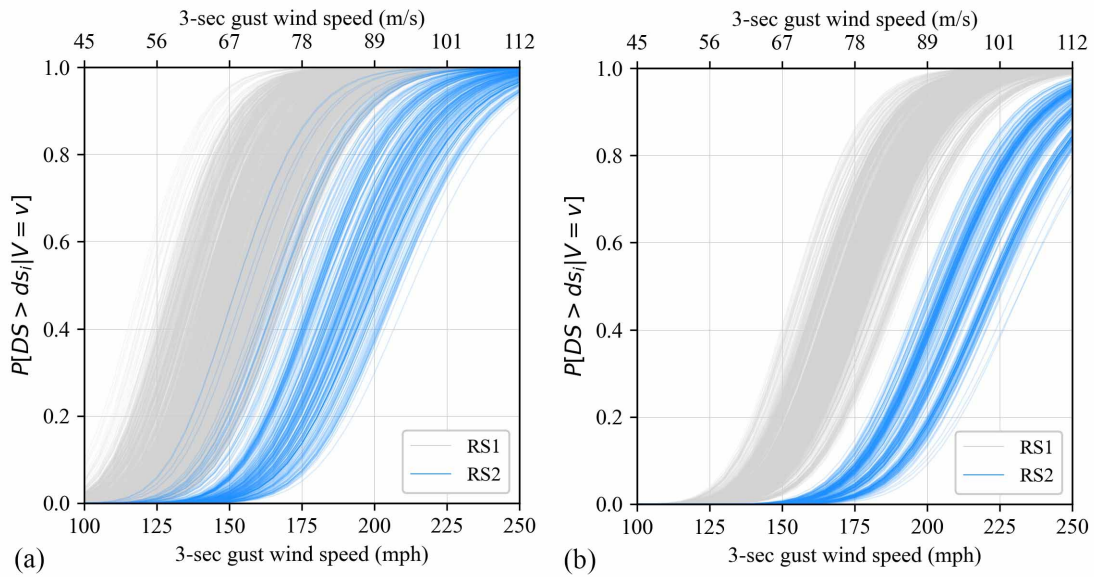


Figure 5.13: Fragility curves for roof sheathing damage: (a) DS1 (no roof sheathing failure); (b) DS3 (25% of roof sheathing failure)

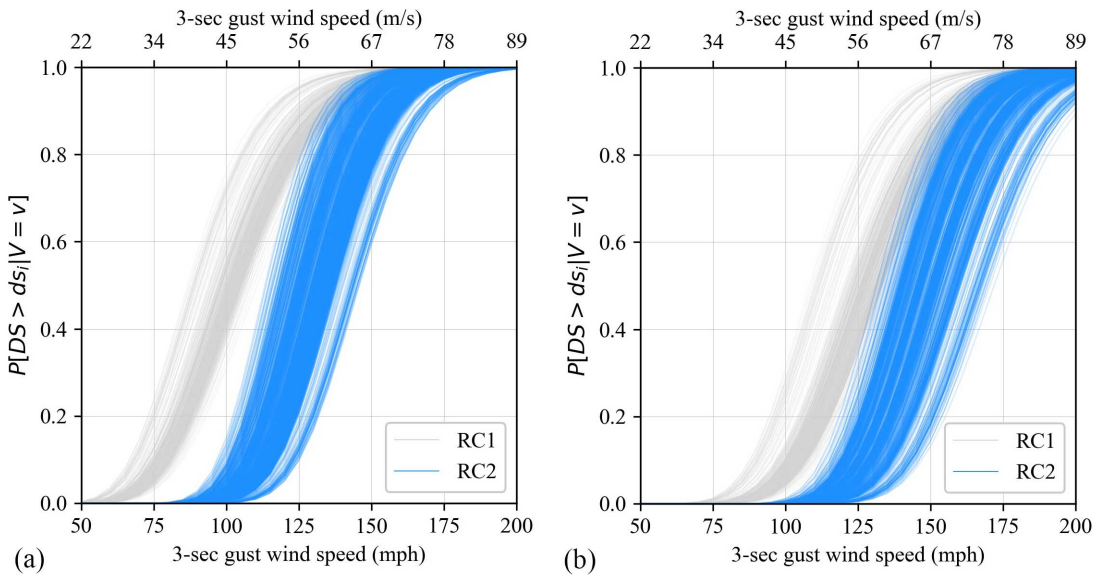


Figure 5.14: Fragility curves for roof covering damage: (a) DS1 (15% of roof covering failure); (b) DS2 (50% of roof covering failure)

To compare the wind vulnerability of openings across different buildings, window damage

curves are plotted in Fig. 5.15. Similar to roof components, component resistance is the most critical factor in determining the vulnerability of windows. Buildings with higher window capacities are expected to suffer substantially less window damage, regardless of other building variables. The variance in damage ratios for the same type of window is primarily due to differences in plan dimensions and the number of stories, which affect the number and elevation of windows. The increased opening height considered for elevated homes also results in higher wind pressures on each window and higher probabilities of window damage. Additionally, the pressure damage of windows is correlated with the damage condition of roof sheathing, which affects the internal pressures acting on windows.

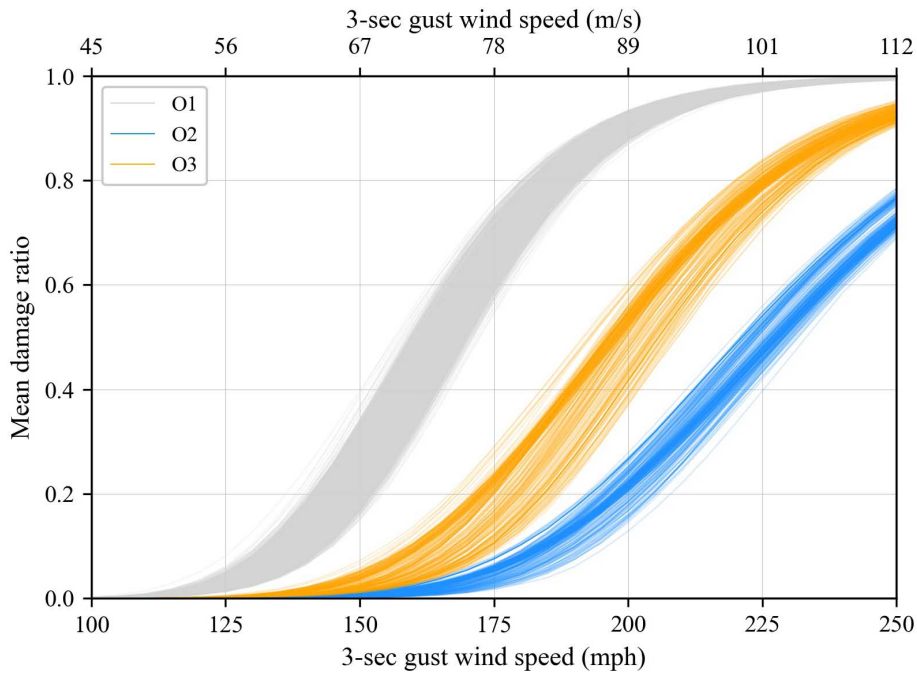


Figure 5.15: Window damage vulnerability

In summary, the wind vulnerability at component level is mainly controlled by the component configuration, which determines the wind resistance. Based on the vulnerability and fragility curves, components with higher capacities are expected to sustain significantly less damage. However, it is observed that the variance in architectural features, which impacts

the number and wind loads of component units, can also affect the component damage condition considerably. In certain cases, due to different building configurations, buildings with retrofitted components may suffer more severe damage than those with standard components.

5.3.2 Building-level damage results

The building-level fragility curves are depicted in Fig. 5.16 based on damage states defined in Table 5.5. Building-level fragility curves generally show greater variance than those for individual components since the building-level damage states can be triggered by multiple failure modes defined based on different components. The median wind speeds exceeding DS1 range between 86 mph and 144 mph, respectively, and the median wind speeds exceeding DS4 vary between 150 mph and 216 mph, respectively. A total of nine combinations of component configurations are assigned to buildings in the study area. Newly constructed houses are more likely to implement hurricane mitigation strategies, which result in higher component capacities. It can be observed from Fig. 5.16 that the fragility curves for each damage state can be classified into two groups, which are caused by different component configurations. Damage states 1-3 are mainly controlled by roof covering damage, while damage state 4 is primarily attributed to roof sheathing failure. Similar to the component-level fragilities, the variation in architectural features also leads to a significant discrepancy in the fragilities at the building level, even among buildings with identical component configurations.

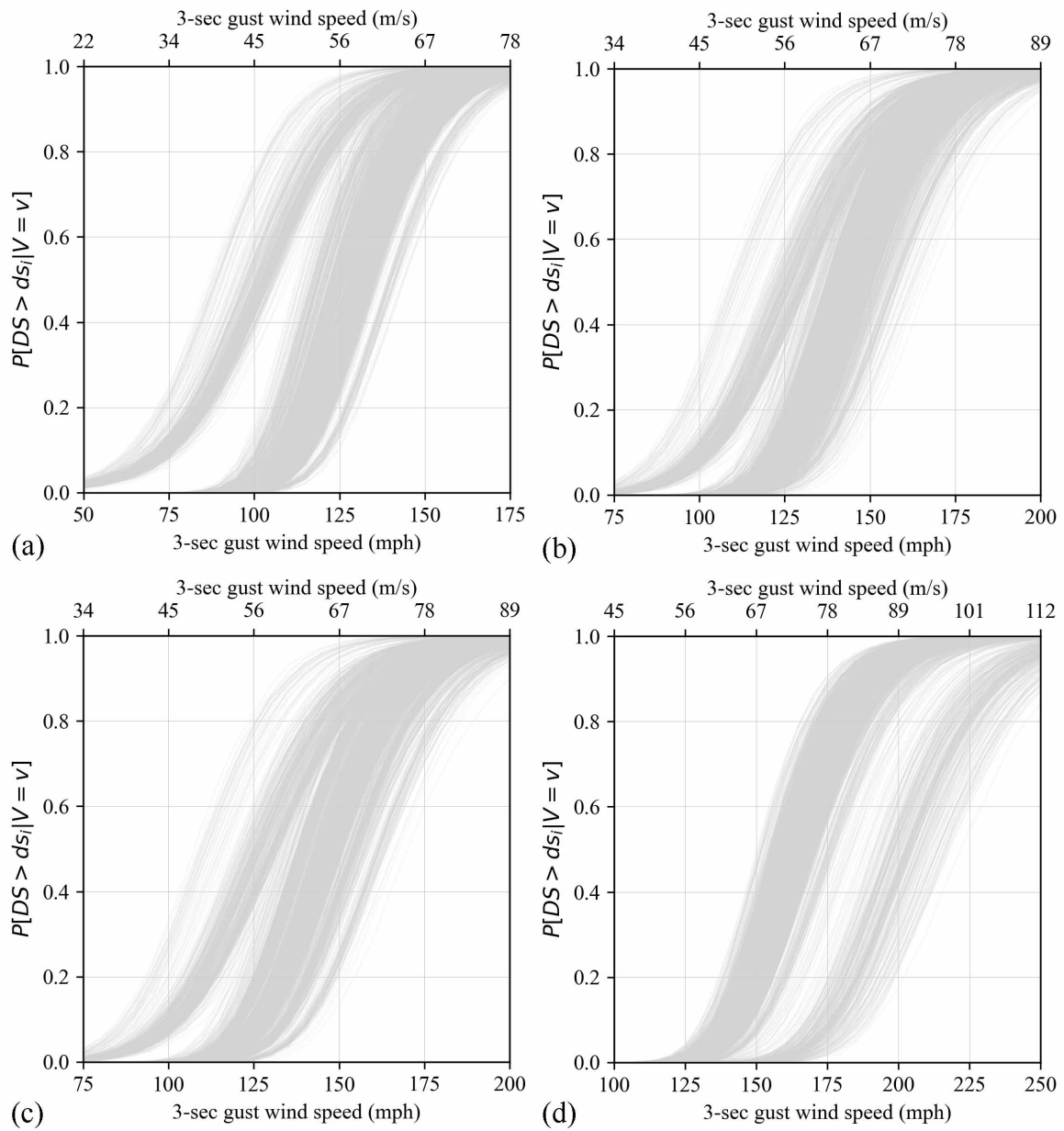


Figure 5.16: Building-level fragility curves: (a) DS1; (b) DS2; (c) DS3; (d) DS4

5.4 Loss Results

The expected annual loss (*EAL*) due to exterior and interior damage was calculated for every single-family house in the study area. By summing up the losses for individual buildings, the aggregated regional losses of \$162,829 and \$229,215 are obtained for study areas 1 and 2, respectively. Figure 5.17 shows the distribution of building-level *EAL* for each study area. The mean and standard deviation of *EAL* for individual houses is \$200 and \$202 for study area 1 and \$246 and \$180 for study area 2. Under similar hazard scenarios, the distributions of *EAL* are similar between the two study areas. On the other hand, substantial variance is observed in building-level *EAL* in both residential communities due to different architectural features, component capacities, and building values.

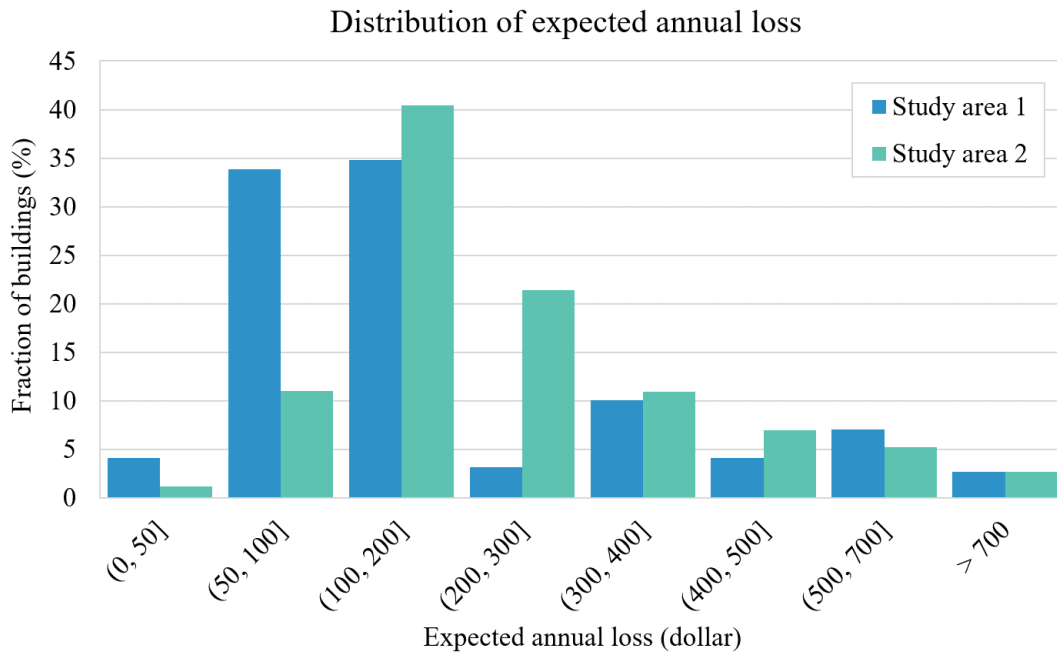


Figure 5.17: Distribution of expected annual loss at building level

Based on the probabilistic hurricane scenarios considered in the loss calculation, Figure 5.18 plots the annual probabilities of exceedance of building-level losses. The results

show that houses can potentially suffer significantly higher losses than the annual expected values under strong hurricanes. The variance in building-level losses increases substantially under more severe hurricane scenarios. The greater divergence observed among the loss curves in study area 2 may be caused by the higher variance in building values for study area 2 (Fig. 4.53).

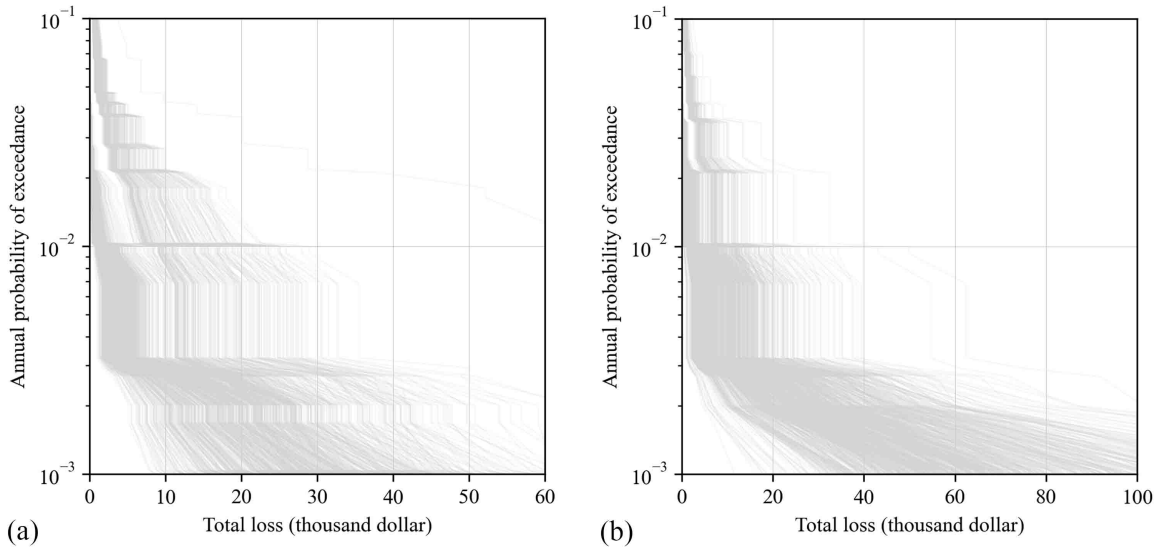


Figure 5.18: Annual probabilities of loss exceedance for individual buildings: (a) Study area 1; (b) Study area 2

To evaluate the effect of refined building models on regional loss estimation, an alternative approach was applied to calculate aggregated regional loss using building archetypes, referred to as the archetype-based assessment. The difference between the archetype-based assessment and the assessment developed in this study is that the building archetypes incorporate fewer variables related to architectural features. Based on building archetypes adopted by existing regional loss models (Vickery, 2006; Gurley et al., 2005; Peng, 2013), variations of three architectural features are considered for modeling single-family houses: roof type (gable or hip), number of stories (one or two), and garage condition (Y or N). Table 5.7 summarizes the differences between the building archetypes and site-specific mod-

els constructed in this study. Deterministic building geometries (e.g., plan dimension and roof pitch) for building archetypes were determined based on the values used by Peng (2013) and Gurley et al. (2005). They are also close to the mean value of each parameter derived from the baseline building inventory (Section 4.2). Other building characteristics, such as overhang and wall height, are identical between the building prototypes and site-specific models. As a result, eight building archetypes are created and mapped to houses in the study area. The building archetypes for houses with garages are illustrated in Fig. 5.19. The number of stories for mapping the archetypes is determined based on n_s^o . Buildings larger or equal to two stories are all modeled by two-story archetypes. Apart from building models, the structural configuration and building value used for the damage and loss analysis are the same between the two types of assessments.

Table 5.7: Comparison between building archetypes and site-specific building models

Building property	Archetype	Site-specific model
Plan dimension	60 ft \times 30 ft	Varies
Roof pitch	5/12 ($\sim 22.6^\circ$)	Varies
Roof type ^a	g/h	g/scg/ccg/h/ch
Number of stories	one/two	one/two/three
Elevated home ^b	N	Y

^a Roof types are defined in Table 3.5.

^b Increased building and component height for elevated houses.

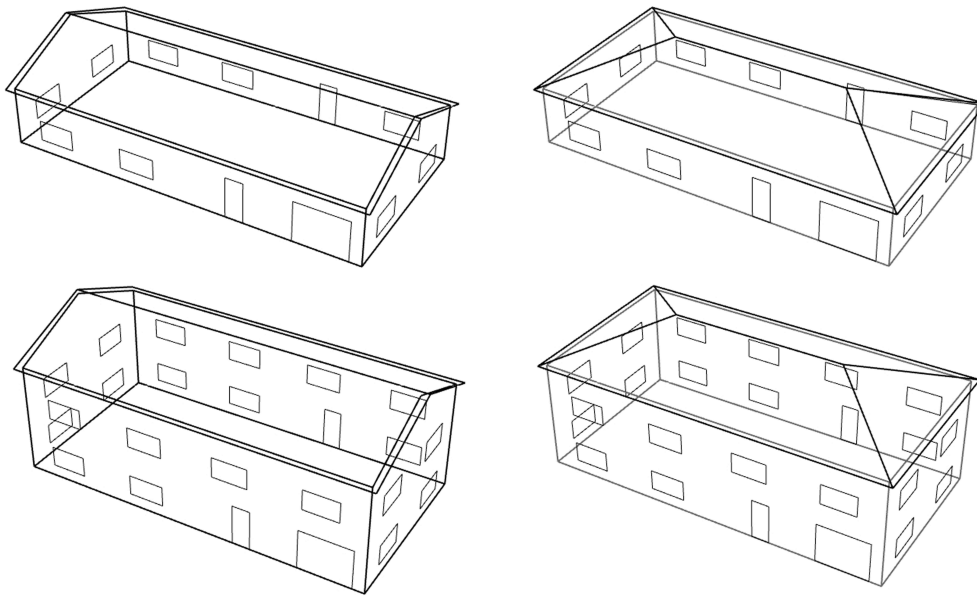


Figure 5.19: Building models and opening layouts for archetype-based loss assessment

The building-level expected annual losses calculated based on two types of assessments are compared in Fig. 5.20. For the majority of houses, the archetype-based assessment produces a lower loss estimation compared to the assessment using site-specific models. The increased building-level loss is primarily caused by the inclusion of non-rectangular building models in the damage analysis, which have substantially higher roof fragilities than those for rectangular buildings. As shown in Fig. 4.56, most houses in both study areas have complex roof shapes and non-rectangular building footprints. Moreover, a large portion of houses in study area 2 are elevated. The increased building height for elevated homes, which is considered in the site-specific model, results in a higher probability of roof and opening damage. To compare the loss results at regional level, the aggregated regional losses calculated using different assessment methods are presented in Fig. 5.21. Compared to the archetype-based assessment, the loss assessment based on site-specific building models predicts 20% and 32% higher regional losses for study areas 1 and 2, respectively. In total, the assessment based on site-specific models produced 27% higher loss estimation than the

archetype-based assessment. Due to the existence of elevated houses in study area 2, the difference in predicted regional loss between the two approaches is more significant for study area 2 than for study area 1. The results suggest that the building archetypes used by existing loss models may lead to underestimating the regional loss consequences. The accuracy of regional loss estimation can be improved substantially by adopting more realistic and detailed building models for damage analysis.

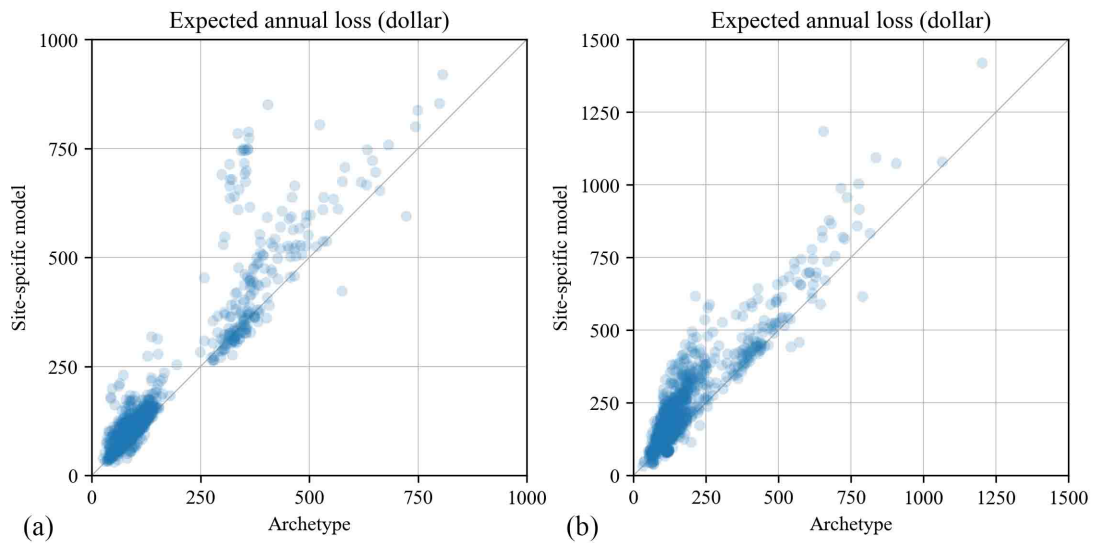


Figure 5.20: Building-level expected annual losses calculated using different types of assessments: (a) Study area 1; (b) Study area 2

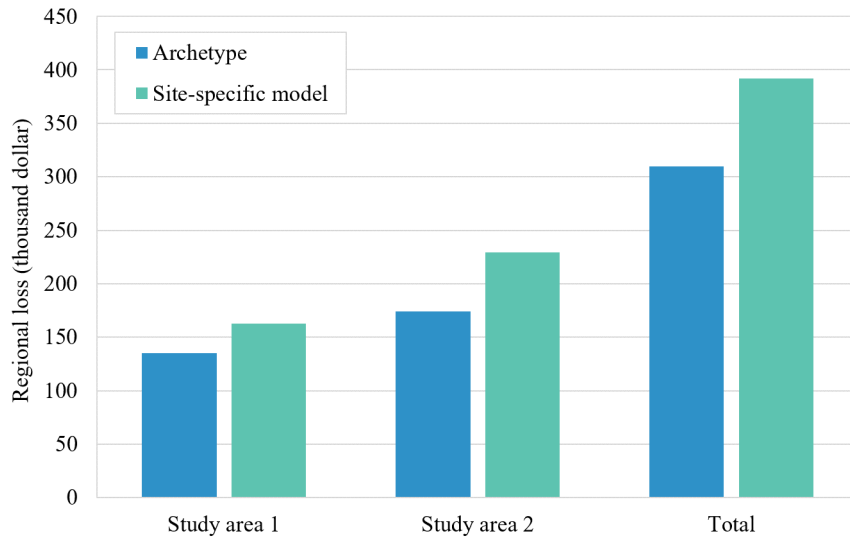


Figure 5.21: Comparison of regional losses between assessments using building archetypes and site-specific building models

5.5 Model Limitations

Facilitated by parcel-based building inventories with enriched building attribute data, the wind damage model was developed based on site-specific building models that are more realistic and detailed than building archetypes adopted by existing models. A major improvement for the building model is the inclusion of complex roof geometries and associated non-rectangular building footprints. To incorporate non-rectangular buildings in the damage assessment, a prescriptive approach was adopted to calculate wind loads based on previous research on fragility analysis for non-rectangular buildings (Amini and van de Lindt, 2014; Masoomi et al., 2018). Due to the lack of data on wind pressures on complex-shaped buildings, key assumptions and simplifications were made for the proposed model.

First, the external wind pressures acting on building envelope components are determined under the worst loading scenario assuming all possible wind directions since direction-specified wind pressure data are not available for non-rectangular buildings. This method

is not applicable to MWFRS components for non-rectangular buildings, including roof-to-wall connections and wall structures. Therefore, only the damage to C&C is considered for the component-based damage model. As defined by the Saffir-Simpson Hurricane Wind Scale (Taylor et al., 2010), site-built houses are expected to experience roof structure and wall structure damage under Category Four Hurricanes (143-172 mph). Consequently, excluding MWFRS in the damage calculation may underestimate the wind losses under very high wind speeds.

Second, the wind damage model only considered the pressure damage to the components. However, wind-borne debris is also a major cause of structural damage under hurricanes, which is usually generated from the damaged components of surrounding buildings (Twisdale et al., 1996; Minor, 2005). The debris effect can cause window breakage at a relatively low wind speed and induce internal pressurization, which can then exacerbate the pressure damage (Chung Yau et al., 2011). While under higher wind speeds, the pressure damage gradually controls the damage to windows, causing the loss attributed to pressure damage to be predominant (Unnikrishnan and Barbato, 2016). Thus, neglecting the debris effect in the damage model results in underestimating the loss at lower loss levels. Unfortunately, previous research on modeling the envelope damage due to wind-borne debris only considered rectangular buildings, and the available methods are coupled with the wind directions (Chung Yau et al., 2011; Ji et al., 2020), which cannot be integrated into the proposed model in this dissertation.

Third, the change in internal pressure due to the damage of openings (e.g., windows and doors) is not considered in the damage analysis. Similar to the modeling of window damage due to debris effect, the internal pressurization due to opening damage is also correlated with the directions of winds (Ji et al., 2020; Stewart et al., 2018; Gurley et al., 2005), which cannot be captured by the proposed model. Considering the increase of internal pressures due to opening damage would lead to higher estimated losses than those shown in this dissertation.

Last, only the losses due to the replacement cost of damaged envelope components and

associated interior damage are considered in the proposed model. Incorporating contents loss and the interior loss due to MWFRS damage in the loss estimation would increase the loss results at both building and regional levels. The difference between the regional losses estimated using different approaches presented in Section 5.4 would also be amplified.

5.6 Summary

This chapter presents a regional wind loss model used to estimate the direct loss due to building envelope damage to single-family dwellings. In the proposed model, site-specific damage and loss analysis is conducted on individual houses in the area of interest. The damage of building envelope components is assessed based on building models that incorporate a variety of site-specific building features. A set of roof archetypes is employed to simplify the modeling process while capturing the distinctive wind performance between roofs with different shapes and complexities.

The proposed model was used to estimate hurricane-induced damage and loss for two residential communities in New Hanover County, which include 1,746 single-family houses. The damage results indicate that component capacities have a more critical effect on the building performance than the combined effect of architectural features. The adoption of hazard mitigation measurements, which increases the wind resistance of building components, significantly reduces the component failure probabilities, and enhances the building performance under extreme winds. Although architectural features have less significant effects compared to component configurations, they still contribute to substantial uncertainties in component and building-level fragilities. Furthermore, the regional losses calculated based on different building modeling approaches were compared. The aggregated regional losses calculated using building archetypes and site-specific building models differ by 20%. The results suggest that the building archetypes adopted by existing regional loss models may lead to underestimating the wind loss. It also demonstrates that the refined building mod-

els developed in this dissertation, which provide a more realistic representation of the real structures, can efficiently improve the accuracy of damage and loss estimation.

CHAPTER 6

CONCLUSIONS AND FUTURE WORK

6.1 Conclusions

This dissertation focuses on improving the structural characterization phase in the wind risk assessment framework for wood-frame single-family houses. To develop efficient and accurate building modeling methodologies, the relative importance of different building variables in wind vulnerability modeling was evaluated. Building shape and roof pitch, the variations of which are not considered in existing loss models, show significant effects on the building performance under extreme winds. Non-rectangular buildings with complex roof geometries should be incorporated into the building models to avoid underestimating the structural damage. Additionally, roofs with similar features (e.g., number of ridgelines) exhibit similar wind vulnerabilities.

Moreover, site-specific risk assessments applied to a large number of buildings provides insights into the relative contribution of building variables to the damage and loss estimation at building and regional levels. The damage results indicate that component capacities have a more critical effect on the building performance than the combined effect of architectural features, while the variation in exterior building features can also cause substantial difference in the building vulnerability. The regional loss results demonstrate that a better representation of the building stock (e.g., including non-rectangular building models, modeling elevated homes with increased building height) significantly increases the estimated regional loss, which in turn addresses that the building archetypes adopted by existing loss

models can potentially underestimate the hurricane-induced loss.

To support the construction of detailed building models, AI-aided data collection tools were developed to extract exterior building features from remote sensing data. The machine learning models show good generalizability and achieve high accuracy in predicting various building characteristics that are not available in publicly available datasets. The proposed building inventory generation model enables the production of large-scale and high-resolution building inventories with enrich building property data. The case studies reveal a great spatial variance in the distribution of critical building characteristics, which can lead to distinctive local hurricane risk.

An automated modeling process was built upon the parcel-based building inventories to create 3D building models for individual buildings. Five archetype roof configurations were designed to simplify the modeling of roof structures while capturing the distinctive wind performance between roofs with different shapes and complexities. The adoption of site-specific building models for damage analysis largely reduces the inherent uncertainties in hurricane risk prediction and enables the damage and loss estimation at individual building level. The high-resolution damage and loss results produced by the framework can accurately reflect the spatial distribution of building inventories and associated local risk conditions, which facilitates the improvement of hazard risk mitigation and post-disaster management strategies.

6.2 Future Work

Future work can be conducted in following areas to improve the proposed framework:

- With more wind pressure data for complex-shaped buildings available in the future, the wind directionality can be incorporated into the damage analysis, which can further enable the evaluation of the debris effect and the adjustment of internal pressures due to opening damage.

- The building inventory generation model can be improved to collect building information related to the structural configuration. Building images contain useful information for component configurations (e.g., roof covering type) and hurricane retrofit strategies (e.g., hurricane shutters), which can be extracted using deep learning models. The structural properties obtained based on image-processing can greatly reduce the uncertainties associated with the wind resistance of buildings.
- Based on the building-level damage results derived in this study, machine learning models can be trained to predict fragility parameters (e.g., mean and standard deviation of component fragility curves) directly from critical building characteristics, without the need for structural analysis. This can significantly reduce the computational cost of assessing the wind risk of a large geographic area while still capturing the variation in wind vulnerability between individual buildings.
- The storm surge flood risk assessment can be integrated into the proposed framework. The inventory generation model is capable of identifying elevated houses, which is one of the most common flood mitigation measurements for single-family houses. Given the available building inventory data, site-specific floor risk assessment can be added to the framework to provide a more comprehensive evaluation of hurricane-induced losses.

APPENDIX A

EXTERNAL WIND PRESSURE COEFFICIENTS

Tables A.1 and A.2 summarize the negative external wind pressure coefficients (GC_p) for C&C on gable and hip roofs, as defined in ASCEC 7-16 (ASCE, 2016). GC_p is defined as a function of roof pitch and effective wind area for each wind zone. The wind zones associated with gable and hip roofs are illustrated in Fig. 3.6. The GC_p values shown in Tables A.1 and A.2 are used to determine wind pressures on roof sheathing and roof covering, which have effective wind area smaller than 10 ft² (Rosowsky and Schiff, 1996).

Table A.1: Nominal value of negative GC_p for C&C on gable roofs

Location	Roof pitch	Wind zone					
		1	2e	2n	2r	3e	3r
Roof	3/12 and 4/12	-2.0	-2.0	-3.0	-3.0	-3.0	-3.6
	5/12 and 6/12	-1.5	-1.5	-2.5	-2.5	-2.5	-3.6
	Larger than 6/12	-1.8	-1.8	-2.0	-1.8	-3.2	-2.0
Overhang	3/12 and 4/12	-2.5	-2.5	-3.5	-3.5	-4.1	-4.7
	5/12 and 6/12	-2.0	-2.0	-3.0	-3.0	-3.6	-4.7
	Larger than 6/12	-2.6	-2.6	-2.8	-2.6	-4.0	-2.8

Table A.2: Nominal value of negative GC_p for C&C on hip roofs

Location	Roof pitch	Wind zone			
		1	2e	2r	3
Roof	3/12 and 4/12	-1.3	-1.8	-2.4	-1.8
	5/12 and 6/12	-1.4	-2.0	-2.0	-2.0
	7/12	-1.2	-1.8	-1.5	-2.0
	8/12	-1.3	-2.1	-1.8	-2.4
	9/12	-1.4	-2.3	-2.0	-2.7
	10/12	-1.4	-2.5	-2.3	-3.0
	11/12	-1.5	-2.6	-2.5	-3.3
	12/12	-1.5	-2.8	-2.7	-3.6
Overhang	3/12 and 4/12	-1.8	-2.3	-2.9	-2.9
	5/12 and 6/12	-1.9	2.5	-2.5	-3.1
	7/12	-2.0	-2.6	-2.3	-2.8
	8/12	-2.1	-2.9	-2.6	-3.2
	9/12	-2.2	-3.1	-2.8	-3.5
	10/12	-2.2	-3.3	-3.1	-3.8
	11/12	-2.3	-3.4	-3.3	-4.1
	12/12	-2.3	-3.6	-3.5	-4.4

APPENDIX B

FRAGILITY PARAMETERS FOR ROOF SHEATHING

Tables B.1 - B.5 summarize the lognormal parameters for roof sheathing fragility curves developed for the sensitivity analysis described in Chapter 3. Tables B.6 and B.7 present the results of the ANOVA tests on the median of fragility curves between different model groups in building model set 1. The building models used for the fragility analysis are introduced in Section 3.2, and the damage states for roof sheathing are described in Section 3.3.1.

Table B.1: Lognormal parameters for roof sheathing fragilities (building model set 1)

Structure type	Damage state							
	1		2		3		4	
	λ	ξ	λ	ξ	λ	ξ	λ	ξ
1	5.011	0.122	5.022	0.119	5.084	0.118	5.147	0.118
2	4.964	0.123	4.979	0.120	5.055	0.118	5.127	0.118
3	4.972	0.123	4.987	0.120	5.068	0.118	5.139	0.118
4	4.965	0.122	4.982	0.119	5.064	0.118	5.133	0.118
5	4.965	0.123	4.980	0.120	5.057	0.118	5.129	0.119
6	4.935	0.121	4.948	0.119	5.019	0.117	5.086	0.118
7	4.951	0.121	4.962	0.119	5.030	0.117	5.091	0.117
8	4.940	0.120	4.951	0.119	5.021	0.118	5.092	0.118
9	4.951	0.123	4.962	0.120	5.028	0.118	5.087	0.119
10	4.923	0.122	4.935	0.119	5.004	0.117	5.067	0.118
11	4.926	0.121	4.939	0.119	5.005	0.117	5.068	0.118

12	4.936	0.121	4.949	0.119	5.026	0.118	5.091	0.118
13	4.943	0.121	4.954	0.119	5.019	0.117	5.080	0.118
14	4.928	0.121	4.941	0.119	5.013	0.118	5.081	0.118
15	4.920	0.121	4.931	0.119	4.995	0.118	5.066	0.118
16	4.916	0.120	4.926	0.118	4.989	0.117	5.054	0.118
17	4.920	0.119	4.932	0.117	4.994	0.117	5.054	0.117
18	4.915	0.122	4.927	0.119	4.994	0.118	5.059	0.118
19	4.917	0.120	4.926	0.117	4.985	0.116	5.041	0.117
20	4.912	0.119	4.921	0.118	4.980	0.117	5.040	0.117
21	4.898	0.121	4.910	0.119	4.976	0.118	5.049	0.118
22	4.913	0.120	4.923	0.118	4.982	0.118	5.037	0.117
23	4.914	0.121	4.925	0.119	4.985	0.118	5.047	0.118
24	5.078	0.120	5.084	0.119	5.117	0.118	5.170	0.118
25	5.072	0.119	5.076	0.118	5.103	0.117	5.143	0.118
26	5.072	0.118	5.077	0.117	5.104	0.116	5.145	0.118
27	5.071	0.118	5.076	0.117	5.102	0.117	5.143	0.118
28	5.072	0.119	5.077	0.118	5.103	0.118	5.145	0.118
29	5.075	0.119	5.079	0.118	5.107	0.118	5.148	0.118
30	5.076	0.119	5.081	0.118	5.110	0.117	5.154	0.118
31	5.077	0.119	5.081	0.118	5.110	0.117	5.152	0.118
32	5.077	0.119	5.081	0.118	5.109	0.117	5.152	0.118
33	5.073	0.120	5.078	0.118	5.105	0.118	5.146	0.118
34	5.073	0.119	5.077	0.118	5.103	0.118	5.143	0.119
35	5.071	0.119	5.075	0.118	5.100	0.117	5.138	0.118
36	5.072	0.119	5.076	0.118	5.103	0.117	5.144	0.118
37	5.073	0.119	5.078	0.118	5.104	0.117	5.143	0.117
38	5.076	0.119	5.080	0.118	5.107	0.118	5.147	0.118
39	5.075	0.119	5.079	0.118	5.106	0.117	5.145	0.118
40	5.076	0.119	5.081	0.118	5.108	0.118	5.147	0.118
41	5.074	0.119	5.078	0.118	5.105	0.117	5.145	0.118
42	5.072	0.118	5.076	0.117	5.102	0.117	5.141	0.118
43	5.075	0.119	5.079	0.118	5.106	0.117	5.146	0.118

44	5.072	0.119	5.076	0.118	5.101	0.117	5.139	0.118
45	5.079	0.119	5.084	0.118	5.112	0.117	5.152	0.118
46	5.078	0.120	5.082	0.119	5.109	0.117	5.150	0.118
47	5.073	0.119	5.077	0.118	5.102	0.117	5.141	0.118

Table B.2: Lognormal parameters for roof sheathing fragilities (Structure Type A)

Roof pitch	Damage state							
	1		2		3		4	
	λ	ξ	λ	ξ	λ	ξ	λ	ξ
3/12	4.930	0.121	4.940	0.119	4.996	0.117	5.057	0.118
4/12	4.915	0.121	4.926	0.119	4.980	0.118	5.047	0.118
5/12	4.987	0.123	5.000	0.121	5.070	0.118	5.143	0.118
6/12	5.011	0.122	5.022	0.119	5.084	0.118	5.147	0.118
7/12	5.018	0.123	5.033	0.120	5.097	0.118	5.141	0.118
8/12	5.018	0.123	5.032	0.120	5.096	0.118	5.140	0.118
9/12	5.016	0.124	5.030	0.121	5.093	0.118	5.135	0.118
10/12	5.014	0.124	5.028	0.121	5.090	0.118	5.132	0.118
11/12	5.014	0.124	5.028	0.121	5.090	0.118	5.131	0.119
12/12	5.011	0.124	5.025	0.121	5.088	0.118	5.130	0.118

Table B.3: Lognormal parameters for roof sheathing fragilities (Structure Type B)

Roof pitch	Damage state							
	1		2		3		4	
	λ	ξ	λ	ξ	λ	ξ	λ	ξ
3/12	4.913	0.121	4.922	0.118	4.972	0.116	5.028	0.117
4/12	4.916	0.120	4.926	0.118	4.974	0.116	5.027	0.117
5/12	4.958	0.121	4.969	0.119	5.038	0.117	5.100	0.117
6/12	4.951	0.121	4.962	0.119	5.030	0.117	5.091	0.117

7/12	4.976	0.123	4.991	0.120	5.079	0.118	5.133	0.119
8/12	4.975	0.124	4.990	0.121	5.076	0.118	5.130	0.118
9/12	4.972	0.123	4.988	0.121	5.074	0.118	5.129	0.119
10/12	4.972	0.123	4.987	0.120	5.073	0.118	5.128	0.118
11/12	4.970	0.123	4.984	0.121	5.071	0.119	5.127	0.118
12/12	4.968	0.124	4.982	0.121	5.067	0.119	5.122	0.119

Table B.4: Lognormal parameters for roof sheathing fragilities (Structure Type C)

Roof pitch	Damage state							
	1		2		3		4	
	λ	ξ	λ	ξ	λ	ξ	λ	ξ
3/12	5.085	0.121	5.091	0.119	5.127	0.119	5.174	0.119
4/12	5.075	0.121	5.082	0.119	5.120	0.118	5.168	0.119
5/12	5.081	0.119	5.086	0.118	5.118	0.118	5.172	0.119
6/12	5.078	0.119	5.083	0.119	5.117	0.117	5.170	0.118
7/12	5.096	0.119	5.101	0.119	5.138	0.118	5.212	0.120
8/12	5.045	0.119	5.050	0.118	5.090	0.118	5.163	0.118
9/12	5.000	0.120	5.007	0.119	5.047	0.117	5.114	0.118
10/12	4.961	0.119	4.968	0.118	5.010	0.117	5.073	0.117
11/12	4.929	0.119	4.937	0.118	4.980	0.117	5.045	0.117
12/12	4.901	0.120	4.908	0.119	4.954	0.117	5.020	0.117

Table B.5: Lognormal parameters for roof sheathing fragilities (Structure Type D)

Roof pitch	Damage state							
	1		2		3		4	
	λ	ξ	λ	ξ	λ	ξ	λ	ξ
3/12	5.054	0.120	5.061	0.118	5.099	0.117	5.146	0.118
4/12	5.053	0.120	5.060	0.118	5.097	0.117	5.144	0.118

5/12	5.076	0.120	5.081	0.118	5.109	0.118	5.150	0.118
6/12	5.076	0.119	5.081	0.118	5.107	0.118	5.148	0.118
7/12	5.096	0.119	5.101	0.118	5.134	0.118	5.192	0.119
8/12	5.041	0.119	5.046	0.118	5.083	0.117	5.139	0.118
9/12	4.994	0.120	5.000	0.119	5.038	0.118	5.092	0.118
10/12	4.955	0.119	4.961	0.118	5.000	0.118	5.050	0.118
11/12	4.919	0.119	4.926	0.118	4.966	0.116	5.015	0.117
12/12	4.888	0.118	4.896	0.117	4.936	0.117	4.984	0.117

Table B.6: ANOVA test on the median of fragility curves between gable-roof building model groups

Group A	Group B	p-value			
		DS1	DS2	DS3	DS4
1	2	0.001	0.001	0.041	0.341
1	3	0.001	0.001	0.001	0.001
1	4	0.001	0.001	0.001	0.001
1	5	0.001	0.001	0.001	0.001
1	6	0.001	0.001	0.001	0.001
2	3	0.002	0.001	0.001	0.001
2	4	0.001	0.001	0.001	0.001
2	5	0.001	0.001	0.001	0.001
2	6	0.001	0.001	0.001	0.001
3	4	0.085	0.076	0.131	0.137
3	5	0.001	0.001	0.001	0.001
3	6	0.001	0.001	0.001	0.001
4	5	0.064	0.028	0.001	0.004
4	6	0.001	0.001	0.001	0.001
5	6	0.597	0.408	0.103	0.024

Table B.7: ANOVA test on the median of fragility curves of complex hip-roof building model groups (Groups 7-11)

Damage state 1				
	Sum of squares	df	F-value	p-value
Between groups	0.000044	4	2.739	0.061
Within groups	0.000072	18		
Damage state 2				
	Sum of squares	df	F-value	p-value
Between groups	0.000043	4	2.441	0.084
Within groups	0.000080	18		
Damage state 3				
	Sum of squares	df	F-value	p-value
Between groups	0.000055	4	1.450	0.258
Within groups	0.000172	18		
Damage state 4				
	Sum of squares	df	F-value	p-value
Between groups	0.000072	4	0.977	0.444
Within groups	0.000333	18		

APPENDIX C

BASIC PARAMETERS FOR DAMAGE ANALYSIS

Table C.1 summarizes the discrete wind speeds selected for the damage analysis. The wind speeds are the 3-second gust wind speeds measured at 10 meters above the ground. Table C.2 lists the discrete component damage ratios used for damage and loss calculation. Smaller intervals are adopted for lower damage ratios, which usually have higher occurrence probabilities.

Table C.1: Wind speed

Index	Wind speed (mph)	Index	Wind speed (mph)	Index	Wind speed (mph)
1	0	17	95	33	175
2	20	18	100	34	180
3	25	19	105	35	185
4	30	20	110	36	190
5	35	21	115	37	195
6	40	22	120	38	200
7	45	23	125	39	205
8	50	24	130	40	210
9	55	25	135	41	215
10	60	26	140	42	220
11	65	27	145	43	225
12	70	28	150	44	230
13	75	29	155	45	235
14	80	30	160	46	240
15	85	31	165	47	245
16	90	32	170	48	250

Table C.2: Component damage ratio

Index	Damage ratio	Index	Damage ratio	Index	Damage ratio
1	0	15	0.12	28	0.52
2	0.004	16	0.14	29	0.56
3	0.008	17	0.16	30	0.60
4	0.012	18	0.18	36	0.64
5	0.016	19	0.20	37	0.68
6	0.020	20	0.22	38	0.72
7	0.024	21	0.24	39	0.76
8	0.028	22	0.28	40	0.80
9	0.032	23	0.32	41	0.84
10	0.036	24	0.36	42	0.88
11	0.04	25	0.40	43	0.92
12	0.06	26	0.44	44	0.96
13	0.08	27	0.48	45	1.00
14	0.10				

APPENDIX D

INTERIOR DAMAGE CALCULATION

The damage ratios of interior and utility components are calculated based on the damage ratios of building envelope components, using a set of empirical equations developed by FPHLM (Gurley et al., 2005). The process of interior and utility damage calculation is summarized below:

1. Calculate the damage ratio of each building envelope component, x , using the damage model described in Section 5.1.5.
2. For each building envelope component, compute the interior damage ratio, y , using the corresponding interior equation shown in Table D.1. In the equations shown in following steps, R is a Weibull random variable with a mean of 1.
3. Calculate the damage ratio of interior components as $Y_{int} = \max(y)$, where $Y_{int} \in [0, 1]$.
4. Calculate the damage ratio of mechanical components as $Y_{mech} = \max(0.4Ry)$, where $Y_{mech} \in [0, 1]$.
5. Calculate the damage ratio of electrical components as $Y_{elec} = \max(0.5Ry)$, where $Y_{elec} \in [0, 1]$.
6. Calculate the damage ratio of plumbing components as $Y_{plum} = \max(0.35Ry)$, where $Y_{plum} \in [0, 1]$.

Table D.1: Interior damage equations

Component	Interior equation
Roof sheathing	$y = 1.29x$
Roof cover	$y = 0.62x^2 - 0.2x$
Window	$y = 0.39x^2 + 0.31x$
Door	$y = 0.26x$

REFERENCES

- Abdollahi, A., Pradhan, B., and Alamri, A. M. (2022). An ensemble architecture of deep convolutional segnet and unet networks for building semantic segmentation from high-resolution aerial images. *Geocarto International*, 37(12):3355–3370.
- Alidoost, F. and Arefi, H. (2018). A cnn-based approach for automatic building detection and recognition of roof types using a single aerial image. *PFG–Journal of Photogrammetry, Remote Sensing and Geoinformation Science*, 86(5):235–248.
- Amini, M. O. and van de Lindt, J. W. (2014). Quantitative insight into rational tornado design wind speeds for residential wood-frame structures using fragility approach. *Journal of Structural Engineering*, 140(7):04014033.
- Apivatanagul, P., Davidson, R., Blanton, B., and Nozick, L. (2011). Long-term regional hurricane hazard analysis for wind and storm surge. *Coastal Engineering*, 58(6):499–509.
- ASCE (2010). *ASCE/SEI 7-10 Minimum design loads and associated criteria for buildings and other structures*. American Society of Civil Engineers, Reston, Virginia.
- ASCE (2016). *ASCE/SEI 7-16 Minimum design loads and associated criteria for buildings and other structures*. American Society of Civil Engineers, Reston, Virginia.
- Bengio, Y., Courville, A., and Vincent, P. (2013). Representation learning: A review and new perspectives. *IEEE transactions on pattern analysis and machine intelligence*, 35(8):1798–1828.
- Brown-Giammanco, T. M., Giammanco, I. M., and Pogorzelski, H. (2018). *Hurricane Harvey Wind Damage Investigation*. Insurance Institute for Business and Home Safety.
- Buyukdemircioglu, M., Can, R., and Kocaman, S. (2021). Deep learning based roof type classification using very high resolution aerial imagery. *The International Archives of Photogrammetry, Remote Sensing and Spatial Information Sciences*, 43:55–60.

- Castagno, J. and Atkins, E. (2018). Roof shape classification from lidar and satellite image data fusion using supervised learning. *Sensors*, 18(11):3960.
- Chung Yau, S., Lin, N., and Vanmarcke, E. (2011). Hurricane damage and loss estimation using an integrated vulnerability model. *Natural Hazards Review*, 12(4):184–189.
- Crandell, J. H., Nowak, M., Laatsch, E. M., van Overeem, A., Barbour, C., Dewey, R., Reigel, H., and Angleton, H. (1993). *Assessment of damage to single-family homes caused by Hurricanes Andrew and Iniki*. US Department of Housing and Urban Development’s Office of Policy Development and Research.
- Dai, M., Ward, W. O., Meyers, G., Tingley, D. D., and Mayfield, M. (2021). Residential building facade segmentation in the urban environment. *Building and Environment*, 199:107921.
- Datin, P. L., Prevatt, D. O., and Pang, W. (2011). Wind-uplift capacity of residential wood roof-sheathing panels retrofitted with insulating foam adhesive. *Journal of architectural engineering*, 17(4):144–154.
- De Barros Soares, D., Andrieux, F., Hell, B., Lenhardt, J., Badosa, J., Gavaille, S., Gaiïffas, S., and Bacry, E. (2021). Predicting the solar potential of rooftops using image segmentation and structured data. In *NIPS Proceedings*.
- El-Hariri, H., Mulpuri, K., Hodgson, A., and Garbi, R. (2019). Comparative evaluation of hand-engineered and deep-learned features for neonatal hip bone segmentation in ultrasound. In *Medical Image Computing and Computer Assisted Intervention–MICCAI 2019: 22nd International Conference, Shenzhen, China, October 13–17, 2019, Proceedings, Part II 22*, pages 12–20. Springer.
- Ellingwood, B. R., Rosowsky, D. V., Li, Y., and Kim, J. H. (2004). Fragility assessment of light-frame wood construction subjected to wind and earthquake hazards. *Journal of Structural Engineering*, 130(12):1921–1930.

- Ellingwood, B. R. and Tekie, P. B. (1999). Wind load statistics for probability-based structural design. *J. Struct. Eng.*, 125(4):453–463.
- English, E. C., Friedland, C. J., and Orooji, F. (2017). Combined flood and wind mitigation for hurricane damage prevention: Case for amphibious construction. *Journal of Structural Engineering*, 143(6):06017001.
- FEMA (1992). Building performance: Hurricane andrew in florida.
- Gavanski, E., Kordi, B., Kopp, G. A., and Vickery, P. J. (2013). Wind loads on roof sheathing of houses. *Journal of Wind Engineering and Industrial Aerodynamics*, 114:106–121.
- Gurley, K., Pinelli, J., Subramanian, C., Cope, A., Zhang, L., Murphree, J., Artiles, A., Misra, P., Culati, S., and Simiu, E. (2005). Florida public hurricane loss projection model engineering team final report. *International Hurricane Research Center, Florida Internat'l University*.
- Haklay, M. and Weber, P. (2008). Openstreetmap: User-generated street maps. *IEEE Pervasive computing*, 7(4):12–18.
- Hamid, S. S. (2021). *Florida Public Hurricane Loss Model, version 8.1*. ,submitted to the Florida Commission on Hurricane Loss Projection Methodology, May 24, 2021, https://fphlm.cs.fiu.edu/files/wind_certification/v8.0Submission/Submission_Document/20210609_FP_HLM_2019_FinalizedMar2021_Submission_Document_No_Track_Changes.pdf.
- Hamid, S. S., Pinelli, J.-P., Chen, S.-C., and Gurley, K. (2011). Catastrophe model-based assessment of hurricane risk and estimates of potential insured losses for the state of florida. *Natural Hazards Review*, 12(4):171–176.
- He, W. X. and Hong, H. P. (2012). Probabilistic characterization of roof panel uplift capacity under wind loading. *Canadian Journal of Civil Engineering*, 39(12):1285–1296.

- ICC (2018). *North Carolina State Building Code: Residential Code*. International Code Council, Brea, California.
- Jayaseeli, J. D. and Malathi, D. (2020). An efficient automated road region extraction from high resolution satellite images using improved cuckoo search with multi-level thresholding schema. *Procedia Computer Science*, 167:1161–1170.
- Ji, S., Wei, S., and Lu, M. (2019). A scale robust convolutional neural network for automatic building extraction from aerial and satellite imagery. *International journal of remote sensing*, 40(9):3308–3322.
- Ji, X., Huang, G., Wu, F., and Lu, Z.-H. (2020). Wind-induced hazard assessment for low-rise building envelope considering potential openings. *Journal of Structural Engineering*, 146(4):04020039.
- Kang, J., Körner, M., Wang, Y., Taubenböck, H., and Zhu, X. X. (2018). Building instance classification using street view images. *ISPRS journal of photogrammetry and remote sensing*, 145:44–59.
- Kashani, A. G., Graettinger, A. J., and Dao, T. (2016). Lidar-based methodology to evaluate fragility models for tornado-induced roof damage. *Natural Hazards Review*, 17(3):04016006.
- Kreibich, H., Thieken, A. H., Petrow, T., Müller, M., and Merz, B. (2005). Flood loss reduction of private households due to building precautionary measures—lessons learned from the elbe flood in august 2002. *Natural hazards and earth system sciences*, 5(1):117–126.
- Lee, K. H. and Rosowsky, D. V. (2005). Fragility assessment for roof sheathing failure in high wind regions. *Engineering structures*, 27(6):857–868.

- Li, Y. (2005). *Fragility methodology for performance-based engineering of wood-frame residential construction*. Georgia Institute of Technology.
- Lin, N. and Vanmarcke, E. (2010). Windborne debris risk analysis—part i. introduction and methodology. *Wind and Structures*, 13(2):191.
- Liu, H. and Saathoff, P. J. (1981). Building internal pressure: sudden change. *Journal of the engineering mechanics division*, 107:309–321.
- Marshall, R. D. (1975). A study of wind pressures on a single-family dwelling in model and full scale. *Journal of Wind Engineering and Industrial Aerodynamics*, 1:177–199.
- Masoomi, H., Ameri, M. R., and van de Lindt, J. W. (2018). Wind performance enhancement strategies for residential wood-frame buildings. *Journal of Performance of Constructed Facilities*, 32(3):04018024.
- Meecham, D., Surry, D., and Davenport, A. (1991). The magnitude and distribution of wind-induced pressures on hip and gable roofs. *Journal of Wind Engineering and Industrial Aerodynamics*, 38(2-3):257–272.
- Meloy, N., Sen, R., Pai, N., and Mullins, G. (2007). Roof damage in new homes caused by hurricane charley. *Journal of performance of constructed facilities*, 21(2):97–107.
- Merabet, Y. E., Meurie, C., Ruichek, Y., Sbihi, A., and Touahni, R. (2015). Building roof segmentation from aerial images using a line-and region-based watershed segmentation technique. *Sensors*, 15(2):3172–3203.
- Microsoft (2022). Bing maps tile system. <https://learn.microsoft.com/en-us/bingmaps/articles/bing-maps-tile-system?redirectedfrom=MSDN>. 2022-06-08.
- Minor, J. E. (2005). Lessons learned from failures of the building envelope in windstorms. *Journal of Architectural Engineering*, 11(1):10–13.

- Mohajeri, N., Assouline, D., Guiboud, B., Bill, A., Gudmundsson, A., and Scartezzini, J.-L. (2018). A city-scale roof shape classification using machine learning for solar energy applications. *Renewable Energy*, 121:81–93.
- Mostafa, K., Zisis, I., and Stathopoulos, T. (2022). Large-scale wind testing on roof overhangs for a low-rise building. *Journal of Structural Engineering*, 148(11):04022173.
- National Research Council (1991). *Hurricane Elena, Gulf Coast: August 29-September 2, 1985*. National Academies Press.
- Parackal, K., Humphreys, M., Ginger, J., and Henderson, D. (2016). Wind loads on contemporary australian housing. *Australian Journal of Structural Engineering*, 17(2):136–150.
- Peng, J. (2013). *Modeling natural disaster risk management: Integrating the roles of insurance and retrofit and multiple stakeholder perspectives*. University of Delaware.
- Peng, J., Shan, X. G., Gao, Y., Kesete, Y., Davidson, R. A., Nozick, L. K., and Kruse, J. (2014). Modeling the integrated roles of insurance and retrofit in managing natural disaster risk: A multi-stakeholder perspective. *Natural Hazards*, 74:1043–1068.
- Pinelli, J.-P., Pita, G., Gurley, K., Torkian, B., Hamid, S., and Subramanian, C. (2011). Damage characterization: Application to florida public hurricane loss model. *Natural Hazards Review*, 12(4):190–195.
- Pita, G., Francis, R., Liu, Z., Mitrani-Reiser, J., Guikema, S., and Pinelli, J.-P. (2011). Statistical tools for populating/predicting input data of risk analysis models. In *Vulnerability, Uncertainty, and Risk: Analysis, Modeling, and Management*, pages 468–476.
- Pita, G., Pinelli, J., Subramanian, C., Gurley, K., and Hamid, S. (2008). Hurricane vulnerability of multi-story residential buildings in florida. *Proceedings ESREL 2008*.
- Pita, G., Pinelli, J.-P., Cocke, S., Gurley, K., Mitrani-Reiser, J., Weekes, J., and Hamid, S. (2012). Assessment of hurricane-induced internal damage to low-rise buildings in the florida

- public hurricane loss model. *Journal of wind engineering and industrial aerodynamics*, 104:76–87.
- Qin, H. and Stewart, M. G. (2019). System fragility analysis of roof cladding and trusses for australian contemporary housing subjected to wind uplift. *Structural Safety*, 79:80–93.
- Ronneberger, O., Fischer, P., and Brox, T. (2015). U-net: Convolutional networks for biomedical image segmentation. In *International Conference on Medical image computing and computer-assisted intervention*, pages 234–241. Springer.
- Rosowsky, D. and Schiff, S. (1996). Probabilistic modeling of roof sheathing uplift capacity. In *Probabilistic Mechanics & Structural Reliability*, pages 334–337. ASCE.
- Russakovsky, O., Deng, J., Su, H., Krause, J., Satheesh, S., Ma, S., Huang, Z., Karpathy, A., Khosla, A., Bernstein, M., et al. (2015). Imagenet large scale visual recognition challenge. *International journal of computer vision*, 115:211–252.
- Sarma, H. D., Zisis, I., and Matus, M. (2023). Effect of roof shape on wind vulnerability of roof sheathing panels. *Structural Safety*, 100:102283.
- Schwendicke, F., Chaurasia, A., Arsiwala, L., Lee, J.-H., Elhennawy, K., Jost-Brinkmann, P.-G., Demarco, F., and Krois, J. (2021). Deep learning for cephalometric landmark detection: systematic review and meta-analysis. *Clinical oral investigations*, 25(7):4299–4309.
- Shao, S., Stathopoulos, T., Yang, Q., and Tian, Y. (2018). Wind pressures on 4: 12-sloped hip roofs of l-and t-shaped low-rise buildings. *Journal of Structural Engineering*, 144(7).
- Simonyan, K. and Zisserman, A. (2014). Very deep convolutional networks for large-scale image recognition. *arXiv preprint arXiv:1409.1556*.

- Soares, D. d. B., Andrieux, F., Hell, B., Lenhardt, J., Badosa, J., Gavaille, S., Gaiffas, S., and Bacry, E. (2021). Predicting the solar potential of rooftops using image segmentation and structured data. *arXiv preprint arXiv:2106.15268*.
- Sparks, P. R., Schiff, S., and Reinhold, T. (1994). Wind damage to envelopes of houses and consequent insurance losses. *Journal of wind engineering and industrial aerodynamics*, 53(1-2):145–155.
- Stewart, M. G., Ginger, J. D., Henderson, D. J., and Ryan, P. C. (2018). Fragility and climate impact assessment of contemporary housing roof sheeting failure due to extreme wind. *Engineering Structures*, 171:464–475.
- Taghinezhad, A., Friedland, C. J., Rohli, R. V., and Marx, B. D. (2020). An imputation of first-floor elevation data for the avoided loss analysis of flood-mitigated single-family homes in louisiana, united states. *Frontiers in Built Environment*, 6:138.
- Taylor, H. T., Ward, B., Willis, M., and Zaleski, W. (2010). The saffir-simpson hurricane wind scale. *Atmospheric Administration: Washington, DC, USA*.
- Twisdale, L., Vickery, P., and Steckley, A. (1996). Analysis of hurricane windborne debris risk for residential structures. *Raleigh (NC): Applied Research Associates Inc.*
- Uematsu, Y., Yambe, T., and Yamamoto, A. (2022). Wind loading of photovoltaic panels installed on hip roofs of rectangular and l-shaped low-rise buildings. *Wind*, 2(2):288–304.
- Unnikrishnan, V. U. and Barbato, M. (2016). Performance-based comparison of different storm mitigation techniques for residential buildings. *Journal of Structural Engineering*, 142(6):04016011.
- van de Lindt, J. W. and Dao, T. N. (2009). Performance-based wind engineering for wood-frame buildings. *Journal of Structural Engineering*, 135(2):169–177.

- Vickery, Peter J., e. a. (2006). HAZUS-MH hurricane model methodology . II : damage and loss estimation. *Nat. Hazards Rev.*, 7(2):94–103.
- Vickery, P., Skerlj, P., and Twisdale, L. (2000). Simulation of hurricane risk in the us using empirical track model. *Journal of structural engineering*, 126(10):1222–1237.
- Wang, C., Yu, Q., Law, K. H., McKenna, F., Stella, X. Y., Taciroglu, E., Zsarnóczy, A., Elhaddad, W., and Cetiner, B. (2021). Machine learning-based regional scale intelligent modeling of building information for natural hazard risk management. *Automation in Construction*, 122:103474.
- Wang, D., Davidson, R. A., Nozick, L. K., Trainor, J. E., and Kruse, J. L. (2020). Computational framework to support government policy-making for hurricane risk management. *Natural hazards review*, 21(1):04019012.
- Wiik, T. and Hansen, E. W. (1997). The assessment of wind loads on roof overhang of low-rise buildings. *Journal of wind engineering and industrial aerodynamics*, 67:687–696.
- Wu, G., Guo, Z., Shi, X., Chen, Q., Xu, Y., Shibasaki, R., and Shao, X. (2018). A boundary regulated network for accurate roof segmentation and outline extraction. *Remote Sensing*, 10(8):1195.
- Xing, F., Mohotti, D., and Chauhan, K. (2018). Study on localised wind pressure development in gable roof buildings having different roof pitches with experiments, rans and les simulation models. *Building and Environment*, 143:240–257.
- Xu, Y. L. and Reardon, G. (1998). Variations of wind pressure on hip roofs with roof pitch. *Journal of Wind Engineering and Industrial Aerodynamics*, 73(3):267–284.
- Zambanini, S., Loghin, A.-M., Pfeifer, N., Soley, E. M., and Sablatnig, R. (2020). Detection of parking cars in stereo satellite images. *Remote Sensing*, 12(13):2170.

- Zhang, J., Yin, Z., Chen, P., and Nichele, S. (2020). Emotion recognition using multi-modal data and machine learning techniques: A tutorial and review. *Information Fusion*, 59:103–126.
- Zhou, B., Lapedriza, A., Khosla, A., Oliva, A., and Torralba, A. (2017). Places: A 10 million image database for scene recognition. *IEEE Transactions on Pattern Analysis and Machine Intelligence*.
- Zhou, Z. and Gong, J. (2018). Automated analysis of mobile lidar data for component-level damage assessment of building structures during large coastal storm events. *Computer-Aided Civil and Infrastructure Engineering*, 33(5):373–392.
- Zillow (2018). ZTRAX: Zillow Transaction and Assessor Dataset, 2018-Q2.